ATLAS NOTE

ATL-LARG-PUB-2009-001

January 7, 2009

The Simulation of the ATLAS Liquid Argon Calorimetry

John Paul Archambault[8], Joseph Boudreau[1], Tancredi Carli[5], Davide Costanzo[15], Andrea Dell'Acqua[5], Andrea Di Simone[5], Fares Djama[6], Manuel Gallas[5], Margret Fincke-Keeler[4], Mohsen Khakzad[8], Andrei Kiryunin[3], Peter Krieger[9], Mikhail Leltchouk[2], Peter Loch[6], Hong Ma[10], Sven Menke[3], Emmanuel Monnier[6], Armin Nairz[5], Valentin Niess[6], Gerald Oakham[8], Chris Oram[4], Guennadi Pospelov[3], Srinivasen Rajagopalan[10], Adele Rimoldi[14], David Rousseau[11], John Rutherfoord, William Seligman[2], Andrei Soukharev[12], Pavol Strizenec[3], Moustapha Thioye[17], Jozsef Toth[7], Ilya Tsukerman[13], Vakhtang Tsulaia[1], Guillaume Unal[5], Karl-Johan Grahn[16]

[1] *University of Pittsburgh, Department of Physics and Astronomy, Pittsburgh, PA USA*

[2] *Nevis Laboratory, Columbia University, Irvington, New York USA*

[3] *Max-Planck-Institut fuer Physik, Muenchen Germany*

[4] *University of Victoria, Victoria Ca*

[5] *CERN, Geneva, Switzerland*

[6] *Centre de Physique des Particules de Marseille, IN2P3-CNRS, Marseille France*

[7] *Hungarian Academy of Sciences, Budapest Hungary*

[8] *University of Carleton, Carleton Ca*

[9] *University of Toronto, Toronto Ca*

[10] *Brookhaven National Laboratory,*

Upton NY USA

[11] *Laboratoire de l'Accelerateur Lineaire,*

IN2P3-CNRS, Orsay

[12] *Budker Institute of Nuclear Physics,*

Novosibirsk Russia

[13] *Institute for Theoretical and Experimental Physics,*

Moscow, Russia

[14] *Universit degli Studi di Pavia and INFN, Pavia, Italy*

[15] *University of Sheffield, Sheffield, UK*

[16] *AlbaNova Universitetscentrum, Stockholm,*

Sweden [17] *Stony Brook University*

In ATLAS, all of the electromagnetic calorimetry and part of the hadronic calorimetry is performed by a calorimeter system using liquid argon as the active material, together with various types of absorbers. The liquid argon calorimeter consists of four subsystems: the electromagnetic barrel and endcap accordion calorimeters; the hadronic endcap calorimeters, and the forward calorimeters. A very accurate geometrical description of these calorimeters is used as input to the Geant 4-based ATLAS simulation, and a careful modelling of the signal development is applied in the generation of hits. Certain types of Monte Carlo truth information ("Calibration Hits") may, additionally, be recorded for calorimeter cells as well as for dead material. This note is a comprehensive reference describing the simulation of the four liquid argon calorimeteter components.

Contents

I. INTRODUCTION AND OVERVIEW

In ATLAS hadronic and electromagnetic calorimetry is performed in two subsystems, the Liquid Argon (LAr) Calorimeter and the Tile Calorimeter. In the barrel region, the LAr provides electromagnetic calorimetry, while in the endcap, LAr-based components provide both electromagnetic and hadronic calorimetry. The LAr calorimeter itself consists of four subsystems: the electromagnetic barrel (EMB) at $|\eta| < 1.475$, the electromagnetic endcap (EMEC) $1.375 < |\eta| < 3.2$, the hadronic endcap (HEC) at $1.55 < |\eta| < 3.2$ and the forward calorimeter (FCAL), a totally non-projective detector nominally covering the region of about $3.1 < |\eta| < 4.9$. The Tile calorimeter provides hadronic calorimetry at at $|\eta| < 1.7$. This note describes the simulation of all the LAr systems, i.e. all of the calorimetry except the Tiles.

The simulation of the Liquid Argon Calorimetry has a very long history, during which its functionality has continually improved and its infrastructure has continuously been revised. The focus of this note is the LAr Simulation in its "final" form; which is to say, the simulation in the year 2008. While further development of the simulation is anticipated past this date, the infrastructure has become mostly stable.

The LAr simulation runs within the ATLAS offline framework, Athena[1]. Athena provides the mechanisms for scheduling, running, and steering algorithms and services, and for accessing geometrical data, conditions data, and event data. Within the framework, several services and algorithms run, with relevance to the simulation of ATLAS and of LAr.

The service `GeoModelSvc`[3] builds the geometry of all ATLAS detectors, including the LAr detectors. Both the raw geometry, and the readout geometry[2] are created at this time. Both are highly optimized, tightly coupled, and available to reconstruction algorithms as well as to the simulation. Besides the simulation of full ATLAS, commissioning setups, combined beam test setups, and LAr-only beam test setups can be simulated.

The service `Geo2G4Svc` translates the detector geometry into GEANT4 (G4) Geometry. G4[4] is ATLAS's simulation engine. It simulates the propagation of particles through the detector, and their interaction with the detector. To optimize the speed of the G4 tracking code, G4 geometries contain large amounts of cached information (voxels) which are not present in the GeoModel description. The geometrical alignment of detectors may in general change over a run; however, during simulation (unlike in reconstruction) one set

of alignment conditions is used per job. Therefore the G4 geometry is never stale.

Sensitive detectors are dedicated classes that produce hits during the phase of G4 in which particles are stepped through sensitive volumes of the detector. Many sensitive detectors are used during the LAr simulation, one (or more) sensitive detector for each sensitive volume. In the LAr simulation, the sensitive detectors live in the package `LArG4SD`; they handle the common overhead of hit management but delegate to a `Calculator` the task of performing LAr-subsystem specific computations to determine the time and energy deposit, within a single G4 step. The calculators are classes that live in packages named `LArG4Barrel`, `LArG4EC`, `LArG4HEC`, and `LArG4FCAL`.

`G4AtlasApps` and especially its top algorithm, `PyG4AtlasAlg`, is a framework (for simulation) within-a-framework (Athena). The top algorithm initializes the G4 system and invokes the `Geo2G4Svc`, attaching sensitive detectors to active volumes. Much of the relevant code for this assignment can be found in `G4AtlasApps/python/atlas_calo.py`. In user code, the simulation should be steered through a python control structure named `SimFlags`, which controls many simulation options. Documentation on running simulation may be found in reference [5].

A further level of control is provided by additional run control structures defined in the package `LArG4RunControl`. Normally users do not configure these directly but rather indirectly, via `SimFlags`. The structures are created in python and stored in StoreGate. Later, the structures can be accessed by sensitive detectors. The structures can be saved on the output file where they serve as a record of non-geometrical run options effective during the simulation step. Geometrical run options are stored, by contrast, in the geometry database as part of the geometry "tag;" i.e. the collection of data structures used as input to GeoModel.

G4 treats the generation of a response to energy loss as a two-step process: in the first step the ionization is collected into a "hit" and in the second step, the digitization step, a transducer signal, e.g. an ADC output, is simulated from the hit energy. In ATLAS this typically occurs in two processing steps (i.e. separate executables) so that additional minimum bias events or "pileup" can be added to the physics event. The minimum bias events are taken from a library and hits are merged, followed by digitization.

The large number of hits generated in the LAr needs to be substantially reduced by

merging into readout cells in the simulation step. During the reduction, the x, y, and z position of the individual hits are lost–only the readout cells of the merged hits are retained. As we will describe in a later section, the calorimeter response, including the electronic response, varies greatly as a function of position within the readout cell. These are referred to as "charge collection" effects. For performance reasons, many elements of the electronics response, while conceptually part of digitization, are carried out in the simulation.

The simulation produces two kinds of event (hit) output:

- `LArHit` (energy, time, identifier)
- `CaloCalibrationHit` (energy[4], identifier)

The calibration hits are part of a general accounting scheme for energy flow in the detector. Four types of energies are accounted for: electromagnetic, nonelectromagnetic, invisible and escaped. Electromagnetic energy is energy deposited by electrons and positrons. Nonelectromagnetic energy is energy deposited by charged pions, protons, kaons, hyperons and other hadrons. Invisible energy is energy that is gained or lost by breaking up nuclei. Escaped energy is energy carried out of the cell by particles, which escape the World volume, for example, by neutrinos. The production of calibration hits is enabled via a switch in the `SimFlags.CalibrationRun` property. The possible values of this property are 'LAr', 'Tile', 'LAr+Tile', 'DeadLAr', enabling the calibration hits to be collected in all or part of the detector. By default the value is 'DeadLAr', which causes calibration hits to be collected only in the LAr cryostat. Note, the identification scheme for calibration hits extends that for normal hits by allowing hits to be recorded in voxelized regions *not* in the calorimeter sensitive volume (and even outside of the calorimeter itself).

In the following sections we describe in more detail the simulation of the LAr calorimeter with a mind to providing a good reference on the subject to ATLAS collaborators.

Version	G4 Version	Physics List QGSP_BERT
14.5.0	geant4.9.1.patch03.atlas01	QGSP_BERT
14.4.0	geant4.9.1.patch03.atlas01	QGSP_BERT
14.3.0	geant4.8.3.patch02.atlas03	QGSP_BERT
14.2.0	geant4.8.3.patch02.atlas02	QGSP_BERT
14.1.0	geant4.8.3.patch02.atlas02	QGSP_BERT
14.0.0	geant4.8.3.patch01.atlas00	QGSP_BERT
13.0.10	geant4.8.2.patch01.atlas01	QGSP_EMV
12.5.0	geant4.8.2.patch00.atlas01	QGSP_EMV
12.2.0	geant4.7.1.patch01.atlas03	QGSP_GN
12.0.95	geant4.8.2.patch01.atlas01	QGSP_EMV
12.0.7	geant4.7.1.patch01.atlas03	QGSP_GN
12.0.6	geant4.7.1.patch01.atlas03	QGSP_GN
12.0.5	geant4.7.1.patch01.atlas03	QGSP_GN
12.0.4	geant4.7.1.patch01.atlas03	QGSP_GN
12.0.31	geant4.7.1.patch01.atlas03	QGSP_GN
12.0.3	geant4.7.1.patch01.atlas03	QGSP_GN

TABLE I: Table of GEANT4 versions and physics tables used in recent releases of the simulation. The physics table is a set of configuration parameters used by GEANT4 to steer physics processes under its control.

II. G4 VERSIONS AND PHYSICS TABLES

The GEANT4 version, and the physics table (or description of physics processes, cross sections, etc.) has a strong effect upon the properties of both electromagnetic and hadronic showers, including shower shapes and sampling fractions. Proper calibration of the calorimeter requires the input of information derived from Monte Carlo simulation; these calibration constants are therefore sensitive to both the G4 version and the physics tables. For reference we collect here a list of all GEANT Versions and Physics Lists.

Another important quantity influencing shower properties is the so-called range cut. In the simulation of low-energy delta rays, a parameter controls the energy cut-off to which

delta-rays are tracked in simulation; below that energy, the energy of the delta ray is simply deposited in a single point. The cut-off energy is not expressed in MeV/c^2, but rather in terms of the expected particle range. The range cuts are currently set to 30 microns.

The biggest change that has occurred in recent times is the transition from GEANT v 4.7 to GEANT v 4.8. An improved treatment of multiple scattering was introduced. A positive effect of the fix was that sampling fractions in the calorimeter became much less dependent on the range cut. A negative effect is that the CPU time increased significantly. The special physics list QGSP_EMV partially deactivates the new treatment of multiple scattering, still considered too costly in CPU. The special physics list reduces the impact of the change to GEANT v 4.8. The physics list QGSP_BERT implements the Bertini cascade model for nucleon and pion induced reactions. More information can be found in reference [6], as well as in reference [7]

III. GEOMETRY, ALIGNMENT, AND CONDITIONS DATA

ATLAS where possible employs common software solutions across all of its offline tasks, most importantly, simulation, reconstruction, and data analysis. The technologies for storing and accessing geometry, alignment, and conditions data are therefore also used more widely in ATLAS. Since they are of major importance for the simulation of liquid argon calorimeters, we give a brief description here.

A. The Geometry Database

The basic data for the construction of the LAr geometry are stored in a database (as in all other ATLAS subsystems). The database is organized using relational database technology; its archival copy is stored in a CERN oracle server named `atlas_dd`. Tables within the database are defined, loaded, and collected into specific ATLAS versions, and then frozen, locked, and replicated as a single file to remote users. The system supports versioning and schema evolution. Designated database administrators can define the database's schema, but a wider group of people is allowed to update the database structures. More information on the relational database can be found in Ref[11]; The database may be browsed at:

`http://atlas.web.cern.ch/Atlas/GROUPS/OPERATIONS/dataBases/DDDB/`

Tag name	Purpose
ATLAS-CSC-02-02-00	Adds material distortion to ATLAS-CSC-02-01-00
ATLAS-CSC-02-01-00	Adds misalignments to ATLAS-CSC-02-00-00
ATLAS-CSC-02-00-00	Used in release 13.0.X and 14.0.X series.
ATLAS-CSC-02-01-00	Misaligned Muons. (Now LAr gets misalignment from COOL)
ATLAS-CSC-02-02-00	Material distortions for the LAr and ID (Muons misaligned)
ATLAS-CSC-01-00-00	For 12.0.X releases. This is an ideal geometry tag.
ATLAS-CSC-01-00-01	For (12-13).0.X. ATLAS-CSC-01-00-00; fixes envelope clashes.
ATLAS-CSC-01-01-00	For 12.0.X releases. Adds misalignments to ATLAS-CSC-01-00-00
ATLAS-CSC-01-02-00	For 12.0.X releases. Adds material distortions to ATLAS-CSC-01-02-00
ATLAS-TBEC-01	For the 2002 TB, including only the EMEC.
ATLAS-H6-2002-00	For the 2002 TB, including EMEC and HEC
ATLAS-H6-2003-02	For the 2003 H6 TB, including the FCAL
ATLAS-H6-2004-00	For the 2004 H6 TB with HEC, EMEC, and FCAL
ATLAS-CTB-01	For the H8 Combined Test Beam
ATLAS-Comm-02-00-00	The commissioning setup
ATLAS-CommNF-02-00-00	The commissioning setup with no field

TABLE II: Table of important geometry tags for ATLAS simulations. The special setups for beam test geometries are mostly beyond the scope of this document.

Within the relational database, the data is organized in a hierarchical structure that resembles a directory, using symbolic names called "tags" which are then collected into the hierarchical structure. The database browser allows users to navigate the hierarchy and examine the data contained there. The database contains, in addition to tagged data for full-ATLAS, special sets of tagged data for beam test setups and for commissioning of ATLAS. The full-ATLAS tags start with names like ATLAS-CSC-* ("computing system commissioning"). Table II shows the important geometry tags in use since summer 2006.

B. The Conditions Database

The ATLAS Conditions database provides a storage for non-event data, such as calibration, alignment or Detector Control System[8] (DCS) data. The Conditions database is accessed by the COOL API(Conditions Objects for LCG, where LCG is the LHC Computing Grid, and LHC is the Large Hadron Collider) developed within the LCG Applications Area project. Access to COOL from Athena is done via the Athena IOVDbSvc[9], which provides an interface between conditions data objects in the Athena transient detector store (TDS) and the conditions database itself. The IOVDbSvc takes care of the low-level interactions with COOL, ensuring that the correct conditions data objects are always loaded into the Athena Transient Detector Store (TDS).

The COOL Conditions Database consists of two main components:

- `COOL Folders` are the containers of condition data, which form a hierarchical logical structure of the conditions database. Folders contain the 'indexing' information - interval of validity, tags, and may also contain the conditions data (payload) itself
- `The payload data` is represented by persistent C++ objects which are usually contained within POOL ROOT files. The references to the payload data objects are stored within COOL folders.

LAr Simulation applications access the Conditions Database for retrieval of alignment constants and high voltage imperfection values. The Conditions Database, currently seems to lack a widely available browser, which is a significant drawback. A tool to print database tables from the command line called `AtlCoolConsole.py` is in use and partially fills this void.

1. Alignment

The LAr geometry description contains a set of volumes, whose default positions in space can be corrected by applying delta transformations to generic transformations called AlignableTransforms. These alignable transforms are created at the time the LAr geometry is built and they are stored in StoreGate, in order that they may be retrieved at a later time and adjusted. A list of the important alignable transforms is shown in Table III.

Name	Description
LARCRYO_B	Barrel Cryostat
LARCRYO_EC_POS	Positive Endcap Cryostat
LARCRYO_EC_NEG	Negative Endcap Cryostat
EMB_POS	Positive EM Barrel
EMB_NEG	Negative EM Barrel
EMEC_POS	Positive EM Endcap
EMEC_NEG	Negative EM Endcap
HEC_POS	Positive HEC
HEC_NEG	Negative HEC
HEC1_POS	HEC 1 Module
HEC1_NEG	HEC 1 Module
HEC2_POS	HEC 2 Module
HEC2_NEG	HEC 2 Module
FCAL1_POS	Positive FCAL1 Module
FCAL1_NEG	Negative FCAL1 Module
FCAL2_POS	Positive FCAL2 Module
FCAL2_NEG	Negative FCAL2 Module
FCAL3_POS	Positive FCAL3 Module
FCAL3_NEG	Negative FCAL3 Module
SOLENOID	Solenoid

TABLE III: Named alignable transforms in the ATLAS system, shown in this table together with the main volumes that they are designed to affect. The HEC contains two sets of transforms, the first is in use in cases where the HEC is modeled as a single volume and the second in case the HEC is split into two volumes.

The LAr alignment information is stored in the COOL folder '/LAR/Align'. Currently there are two sets of alignment constants identified by two COOL tags:

- `LARAlign_CSC_00` no alignments, for 'ideal' geometry;
- `LARAlign_CSC_01` initial set of alignments imported to COOL from the Geometry

database.

2. High Voltage Imperfections

High voltage information is read from the real detector using the `DCS` system and into an Oracle database; it can then be accessed through `COOL`. However, we have provided a common layer of software to access the high voltage status. This layer provides a uniform interface across all subsystems and may be accessed in either simulation or reconstruction. It resides in a package called `LArHV`, which contains high-voltage managers for EMB, EMEC, HEC, and FCAL. In addition, where appropriate, the readout geometry layer (in the package `LArReadoutGeometry`) can be accessed for the high voltage information for electrodes (EMB/EMEC), sub-gaps (HEC), or tubes (FCAL) connected to each readout element. The access to high voltage information through the readout geometry layer goes through the high voltage layer, and merely provides another access mechanism to the same data, for convenience. While the simulation is equipped to simulate high voltage imperfections it does not yet apply them. The readout electronics on the detector itself can correct (at least partially) for these imperfections. The question of where to apply high voltage imperfections in simulation is coupled to decisions on how the detector itself will be operated. A second issue is how to take appropriate snapshots of the frequently changing HV information, for replication to remote sites where the simulation is run. For the moment the capability to simulation HV imperfections is held in reserve. Fig. 1 shows a view of the electromagnetic compartments highlighting the state of their high voltages.

C. Field Maps, and Other Inputs

Some inputs to the simulation are stored neither in the conditions database nor the geometry database. These are principally the current maps (described in section VIII 7). They are distributed as files in the area `atlas/offline/data/lar`. It is possible that these data migrate to either the conditions database or the geometry database, but the impact of such a future migration is minimal.

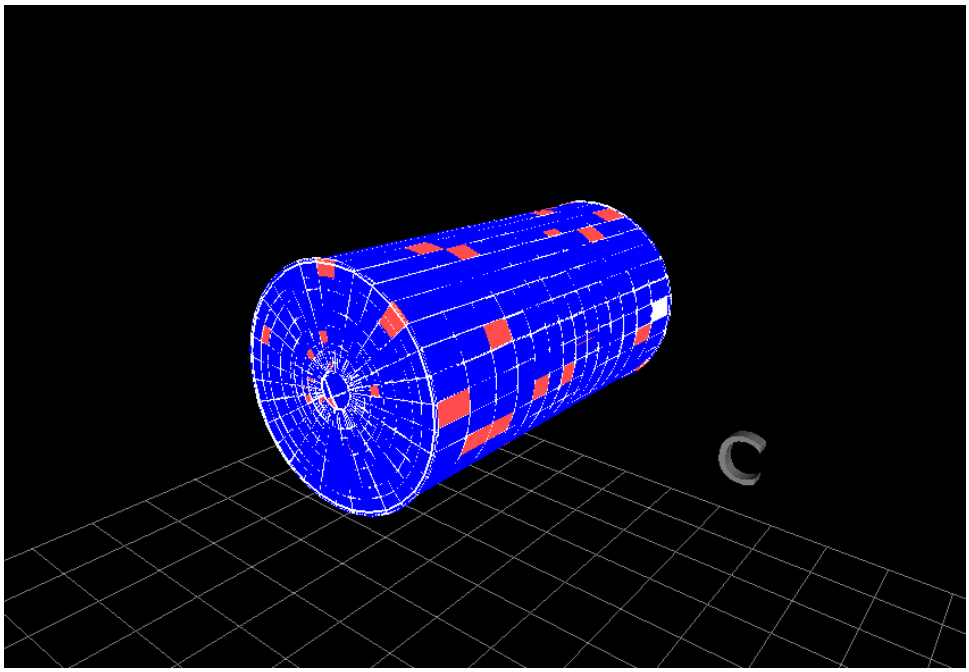

FIG. 1: *A display of the electromagnetic compartments of the calorimeter, in which normal high voltages are shown in blue; out-of-range high voltages are shown in red, and missing high voltages are shown in white.*

IV. HIT PRODUCTION

The output of detector response simulation usually consists of collections of hits which imitate collections of real hits. In the ATLAS calorimeter simulation procedure these hits are called standard hits.

Monte Carlo simulated data contain more information about a particular event or interaction then presented in standard hits, because the underlying generating processes are explicitly known. The corresponding additional information is often referred to as Monte Carlo (MC) Truth information. MC Truth information has been shown to be useful in the understanding of the detector response for guidance in detector design, calibration and general signal corrections, and acceptance estimates in physics studies [10].

A second kind of "hit" is recorded by the LAr simulation, called a calibration hit, which records certain kinds of Monte Carlo truth information. This choice of name reflects one of

the most anticipated use cases for this information. In fact a more general name - *MC truth energy deposit hits* - may be more appropriate. In this document, however, we adhere to the term "calibration hits". The following two sections describe the production of standard hits and calibration hits.

A. Standard LAr Hits

The active region in the calorimeter is the volume which is instrumented for readout in the experiment. It is subdivided into calorimeter cells, each of which corresponds to at least one calorimeter readout channel. Each cell in the calorimeters is uniquely named by a set of indices (which we will call an identifier) encoding not only a unique index but also all information needed to look-up or return the cell location, the names of the calorimeter module and layer it is in, and other useful geometry information. A set of classes pack and unpack the indices into an identifier. These classes are called Id Helpers and the specific classes are:

- LArEM_ID
- LArHEC_ID
- LArFCAL_ID

Details of hit production in various subsystems are described in later sections of this note. The granularity of the readout geometry varies over the calorimeter. Energy deposits are recorded within each cell. The energy corresponds to the true energy loss of all particles crossing the cell's active layer (liquid argon gap) in a given event, which is the source of the signals (real hits) detected in the experiment.

The energy in each cell is accumulated from G4 hits, so, with the caveat that the binning varies over the calorimeter, the hit production mechanisms are conceptually similar to a scatterplot. A further detail is that a *time* is generated for each hit. The time t is like a third axis on the $\eta - \phi$ scatterplot. The calorimeter is binned not only by the readout granularity but also into time slices with a time width of 2.5 ns. The data structures used to implement this is a set of hits for each time bin, and a map from time bin index to hit set.

The mechanism for hit production is the following. A sensitive detector processes a single G4 step. The time, energy, and position are computed. The time is used to identify the time bin and the position is used to identify the readout cell. Within each cell an energy and energy-weighted average time is computed. The result is recorded as a `LArHit` and written out by the simulation. This involves a partial loss of time information.

In most cases a single sensitive detector is assigned to an active volume. In several cases however multiple SD's are active, and, they will generate on the output multiple hits for the same readout cell. One example is the EMEC, where one sensitive detector handles the so-called barrette region (described below) while another sensitive detector handles the rest of the EMEC. Parameterization (outside the scope of this document) also produces hits which are unmerged with hits from full simulation. There appears to be no drawback to this, so we retain it, at least for now.

B. Calibration Hits

Monte Carlo truth information is classified by energy type and by cell location. The "cells" include, actually, not only the standard calorimeter cells with standard granularity but also a voxelization of the entire ATLAS detector, even the parts (e.g. the inner detector) not strictly corresponding to the LAr or its services. In the following sections we describe the classification of energy, and also the division of ATLAS into regions.

The *detectable energy* E_{detect}, i.e. the energy deposited in the active medium of the calorimeter, is accumulated for each calorimeter cell during an event simulation and used for signal calculation to form the previously discussed *standard* calorimetric hit for this cell.

The total *deposited energy* E_{dep}in a given calorimeter cell volume, including active medium and absorber, is not accessible in the the real detector response but it is accessible in the Monte Carlo simulation. In the ATLAS GEANT4-based simulation it is accumulated in a calibration hit, which more generally represents all energy deposits in space, even outside of the global calorimeter volume itself.

As with a standard hit, a calibration hit is formed by sum of all energy deposits in a cell during the simulation of one event. The cell can either correspond to a calorimeter cell generating a detectable signal, or to a dead material "cell", which is created by subdividing

the inactive material outside of the sensitive calorimeter cell volumes.

Three categories of calibration hits: *active*, *inactive*, and *dead* are defined, based on two categories of regions: the active and the dead regions.

The three calibration hit collections are stored separately in `CaloCalibHitCollections` named

- `LArCalibrationHitActive`
- `LArCalibrationHitInactive`
- `LArCalibrationHitDeadMaterial`

In contrast to standard hits, calibration hits record the energy deposits only, and not the time. In addition, the detectable energy does not include any charge collection corrections and so, in general, will not agree with the energies recorded in the standard hits.

For each event the sum of all calibration hit energies collected in the entire simulation world, together with the energy leaving the simulated world setup, is equal to the total energy carried by the generated primary particle(s).

1. Active calorimeter regions

Within the active region of the calorimeter, a cell has both *active* and *inactive* materials. The active material is the sensitive medium like liquid argon (or, for tile, scintillator). The sum of the energies deposited at GEANT4 steps in this material of a given cell for a given event is the basis of the signal and, at accumulated the hit level, stored as E_{detect}in a standard hit with unique cell identifier.

The inactive material in a cell is largely provided by the absorber (lead, copper, or tungsten in LAr, and iron in Tile) which is a necessary part of any sampling calorimeter. The absorber is a dense medium needed for electromagnetic and hadronic showers development and determines the number of secondary particles in a shower and the shower size. There may be additional inactive materials within the cell volume - for the LAr they are electrode boards, glues, and parts of the liquid argon volume from which signal can't be collected. In the ATLAS nomenclature and in this note all these particular inactive materials are *not*

considered dead. The name "dead" is reserved for materials outside of the active calorimeter region.

To properly collect calibration hits it is necessary to describe the exact cell structure made of active and inactive material in order to sum energy deposits which contribute to the signal as active calibration hits, and deposits which do not contribute to the signal as inactive calibration hits.

Note that the positions of the boundaries between cells inside absorbers and other inactive materials are not important for a standard hit and for active calibration hit definitions but they should be exactly defined for inactive calibration hit definition. The cell boundaries need to be defined in detail also in cases with a "gap" of dead material between cells (see below).

The standard cell identifier used in the standard signal hits is also used in the active and inactive calibration hits as a key for the energy collection. This means that these three types of hits are stored in exactly the same granularity.

2. Dead Regions

From the calorimetry point of view, dead regions contain all materials outside active zones of the LAr and Tile. These include cryostat walls, the magnet coil, mechanical support structures inside and outside of the cryostats, non-instrumented liquid argon, electronic crates; all materials of the ATLAS Inner Detector, including the silicon and pixel detectors which reconstruct charged tracks in front of the calorimeters; and all materials of Muon System, typically behind the calorimeters. Note that the Inner Detector in front of the ATLAS calorimeters is also considered to be a dead region, as all energies lost in the corresponding material are not available for calorimetric detection.

The dead region classification has been introduced because the energy losses in the corresponding materials have no direct contribution to the calorimeter cell signals. They are typically not used in a first order calibration, which is a first attempt to reconstruct the total energy deposited within an active region. The energy losses in dead materials are important for the determination of additional signal corrections.

Naturally, there are no signal hits in dead material, at least not from the point of view

of the calorimeters. The calibration hits, though, can be produced in this material as well. Unlike the active region of the calorimeter, there is no hardware-implied cell structure. Thus, a virtual division of these materials into dead material cells has been introduced with a granularity of $\Delta\eta \times \Delta\varphi = 0.1 \times 0.1$ and several layers of depth segmentation, indicating with the necessary detail if the hit has been collected in front, within[23], or behind the calorimeters (leakage detection). This particular virtual division of the ATLAS detector defines the structure of the dead calibration hit collection. Such a virtual division is widely used in calibration hit applications but evidently it is not the only possible virtual division.

It is important to note that, in general, the virtual division of a whole ATLAS detector (or of some part of it) can be optimized for special studies. For example, a special dead material subdivision was implemented for testbeam studies where only a limited set of the ATLAS subdetectors were employed.

Note the difference between the dead calibration hit identifiers, which correspond to virtual cells of the dead material regions, and inactive calibration hit identifiers which correspond to cells of active calorimeter regions. While different versions of the former can be chosen (optimized for different applications), the latter should correspond to read-out channels of real calorimeters.

3. Energy Flow and Classification for Calibration Hits

In the GEANT4 detector description all active calorimeters and all dead materials are placed in the World volume. During event simulation, the energy of primary particle(s) will be carried by (distributed between) secondary particles and finally deposited somewhere inside the World volume or will escape as energy of particles leaving the World volume. The previous two sections have described the manner in which the energies recorded in calibration hits are subdivided into geometrical cells. The energies are further classified according to the physics processes that deposit them. There are two main classifications, visible energy and invisible energy. Visible energy is further subdivided into electromagnetic, and non-electromagnetic energy. Invisible energy is further subdivided into invisible energy losses and escaped energy. Practically all energy of an electromagnetic shower is visible EM energy; the other categories apply chiefly to processes within hadronic showers.

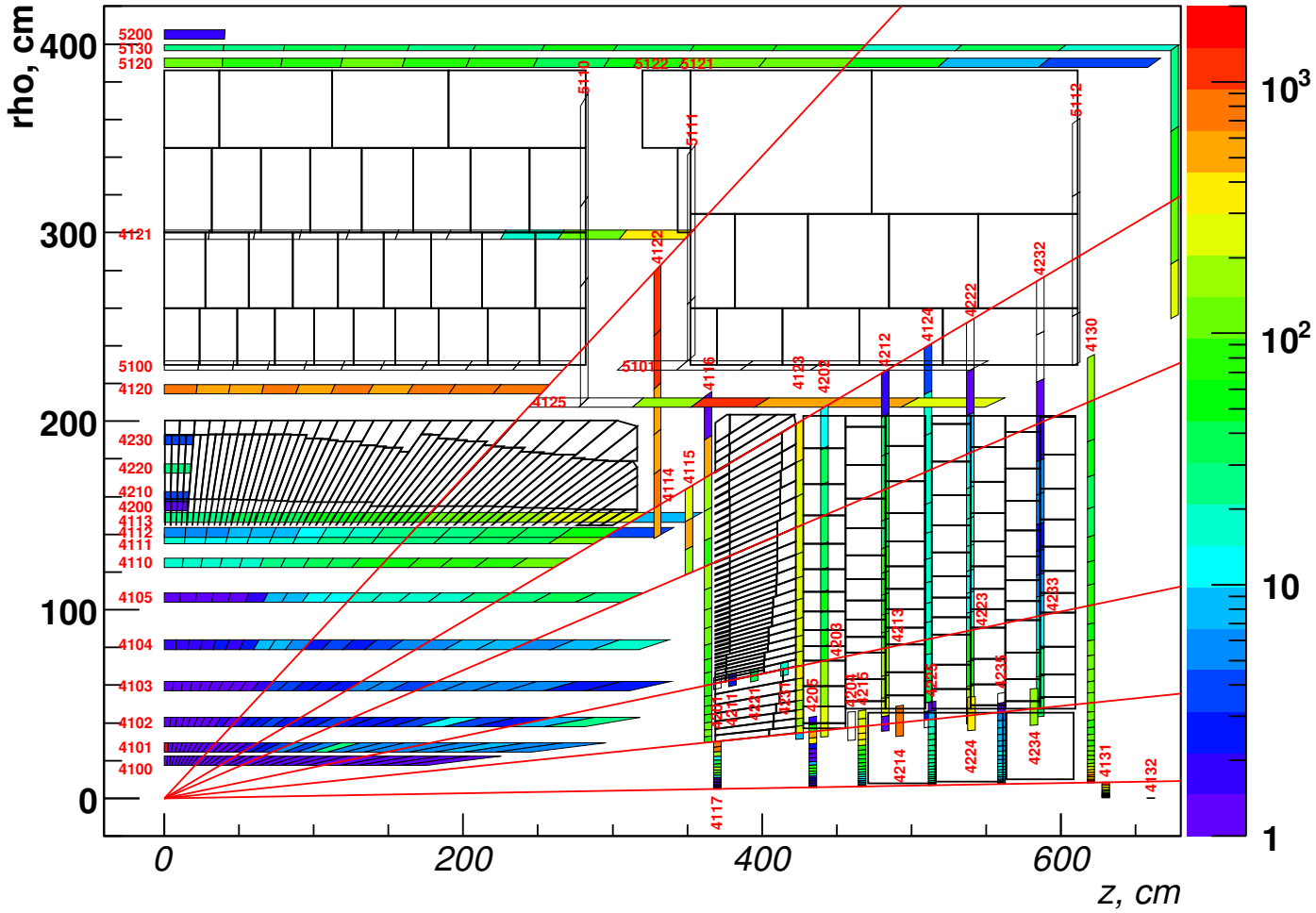

FIG. 2: This figure shows the division of the ATLAS detector into cells. In the active regions of the LAr and Tile calorimeters these cells correspond to readout cells; in the inactive materials throughout the detector they correspond to an extension of the notion of a "cell"; in particular a cell in the dead material is simply a voxelized region of space, imposed upon either a particular volume like a cryostat, or else upon a region of ATLAS as a whole. Each dead material (DM) calibration hit is presented as coloured box on rz plane (the more energy, the redder the colour). The colours of this figure show average energies deposited in DM calibration hits for 500 GeV negative pions (10000 single pion events total), with a flat distribution in η and ϕ coordinates over the full detector. Here, energy from hits with the same η and radius but different ϕ coordinate are gathered into one box. Red numbers represent the dead material region number.

Each hit in the calibration hit collection records the four types of energies. In the following

two subsections we describe the classification of energies in more detail.

4. Visible Energy

Visible energy deposits are those that arise from processes which would be detectable in active materials. These are divided into electromagnetic (EM) and nonelectromagnetic (NonEM) visible energy. These categories of energy classification have been chosen for better understanding of calorimeter response with the main goal to improve the calorimeter calibration for a best possible measurement of hadronic shower energy.

A hadronic shower is a product of a high energy hadron or jet interaction with calorimeter materials. The energy deposit in a hadronic shower consists of an electromagnetic (EM) component from π^0's, and a non-electromagnetic (NonEM) component mainly from ionization energy deposited by secondary low-energy hadrons. In a reald detector the EM and NonEM energy depositions are converted to calorimeter read-out signals with different conversion efficiencies. Thus, it is useful to subdivide the visible energy into these two categories based on information about the physics processes simulated by GEANT4. The classification applies, however, even when the energy is deposited in inactive or dead materials.

The calorimeter is said to be noncompensating if the ratio of the EM and hadronic conversion efficiencies (called the intrinsic e/h ratio) is not equal to 1. ATLAS calorimeters are noncompensating.

5. Invisible energies

Invisible energy deposits arise from processes that normally are not detectable, even if they were to occur in active materials. There are two categories: invisible energy loss, and escaped energy.

Invisible energy loss is typical of G4 steps which end with a hadronic interaction. Some energy losses generated in hadronic inelastic interactions do not contribute to the signal at all. Typical examples are binding energy losses in post-collision nuclear break-up.

Escaped energy is energy which is carried out by a particle escaping from the world volume and applied to the cell where this particle was created. A typical case is a neutrino from the weak decay of a π^+.

6. *Implemented classification of energy deposits*

The implementation of the energy classification scheme resides in the package `Calorimeter/CaloG4Sim`, which is used not only within the LAr simulation but also within the Tile simulation. Classes in that package use the following set of criteria to classify energies:

electromagnetic energy deposits E_{dep}^{em} are energy deposits generated by passage of electrons or positrons through matter, or by the atomic photoelectric effect - one specific process only many possible photon interactions in matter. This is because in the GEANT4 implementation, the kinetic energy of a very soft photoelectron is deposited at its point of production without being tracked further.

These energy deposits are the only ones occurring within the development of an EM shower, with the exception of a very small and often negligible hadronic component from photo-nuclear reactions. Note that in purely electromagnetic showers these deposits are the fractional energy loss dE/dx, integrated along all electron and positron tracks.

nonelectromagnetic energy deposits E_{dep}^{NonEM} (sometimes called ionization energy deposit E_{dep}^{ion}) are generated by any particle (or nuclear fragment) except electrons and positrons and except the energy deposits from atomic photoelectric effect.

Note that, although NonEM energy deposits arise mainly from ionization energy lost by secondary low-energy charged hadrons and by muons, any energy deposits other than E_{dep}^{em} (including deposits generated by any rare or exotic process) are included in E_{dep}^{NonEM} by definition.

invisible energy losses E_{inv} are mostly generated in hadronic inelastic interactions, like hadron-nucleon collisions in the development of a hadronic shower. By definition, they do not contribute to the signal. Typical examples are binding energy losses in post-collision nuclear break-up.

E_{inv} is calculated at the end of each GEANT4 step as imbalance of incoming and outcoming energies from which the escaped energy is subtracted (see [10] for more details).

escaped energies E_{esc} form a special class contributing to the inbalance between incoming and outcoming energy and consist of the energies of neutrinos or other particles (photon, neutron, muon, ...) that escapes from the World volume.

Any of the four types of energy losses described above can occur in any type of material: in active, inactive, or dead materials.

C. Sensitive Detectors and Hit Management

The main package containing sensitive detector code is `LArG4SD`. That package contains one class, also called `LArG4SD`, which uses calculators (subclasses of `LArVCalculator`) to do the detailed work of applying charge collection effects if applicable, and computing the cell identifier for storage in `LArG4Hits`

Another class, `LArG4CalibSD`, performs the same task for calibration hits, using calibration calculators (class `VCalibrationCalculator`) for the detailed work.

In general, for a run with calibration hits, one needs to apply:

- Calibration sensitive detectors to specific materials (e.g. the cryostat) within dead regions.
- Both standard sensitive detectors, and calibration sensitive detectors, to active volumes.
- A default sensitive detector to everything else.

The notion of the "default sensitive detector" comes from GEANT4, which allows one to attach by default some sensitive detector to all volumes to which one has not already attached any other sensitive detector. In ATLAS, the `LArG4CalibSD` creates a default sensitive detector, with a default calibration calculator, and declares it to G4's sensitive detector at an early processing stage.

When more than one sensitive detector is required for a single volume, the class `LArG4MultSD` can be used to chain two of them together. This is how a normal sensitive detector and a calibration sensitive detector are chained together.

The process by which hits are collected in independent time bins and finally merged at the end of the event simulation is controlled by a so-called HitMerger class. The hit merger

class is given the energies, time, and identifiers at each G4Step. It collects that input, keeps it separated by time bin until the end of the event, and finally computes the total energy and energy-weighted time at the end of the event, when it is called back by the sensitive detector. The HitMerger maintains one `LArHitCollection` for each subsystem, EMB, EMEC, HEC, and FCAL.

The HitMerger itself is extensible. Other hit mergers can be created and registered with the system. The main purpose is to allow the creation of other kinds of hits besides the standard `LArHits`–without interfering with the production of standard hits. An example of a use-case are the user-defined extensions of Monte Carlo truth information. In order to extend the present system with new types of hits, one needs to take the following actions:

- Create a new hit class in `LArSimEvent`
- Create a new hit merger class, in a new package, and a new hit merger factor to instantiate it following the pattern of the standard hit merger classes, `LArHitMerger` and `LArHitMergerFactory`
- Create a new Application Action which adds the hit merger factor to StoreGate, following the example in `LArG4HitManagement/LArHitsEventAction`
- Load the new action in python script.

A similar mechanism will soon be available for calibration hits.

V. THE TOP OF THE GEOMETRY HIERARCHY ("TREE TOPS")

The geometry is implemented as a tree of volumes. For the LAr, this tree is rooted in three tree-tops, one for the barrel and one for each endcap. This is shown in Fig. 3. The barrel mother volume is modeled as a simple centered polycone.

The endcap is constructed as a polycone whose $z = 0$ plane is at the outermost boundary. The $z = 0$ boundary of the mother volume coincides with the back of the cryostat, and that choice is driven by the fact that this plane is marked with precision alignment markers. The front face of the polycone is at -3245 mm. This is large enough to accommodate an extra pocket for the Minimum Bias Scintillators which protrude inwards by 71 mm from

the endcap. Within the endcap cryostat, all positions are then specified with respect to the $z = 0$ surface. The barrel mother volume has been artificially extended (the series of steps one sees, in Fig 3, at the end of the barrel mother) to accommodate cables and cooling from the inner detector through the crack region.

The 39 mm gap between the volumes containing the barrel and endcaps allows for large misalignments of either barrel or endcap without generating geometry clashes. All three of the tree tops are alignable. In the relational database scheme the alignments correspond to the names LARCRYO_B, LARCRYO_EC_POS, and LARCRYO_EC_NEG, in Table III.

These volumes are constructed via `GeoModelTool`s and `GeoModelFactory`s, which live in the package `LArCalorimeter/LArGeoModel/LArGeoAlgsNV`. At the time the top level volumes are created they are also filled with their substructure by dedicated Construction classes living in packages such as `LArGeoBarrel`, `LArGeoEndcap`, etc. The factories create trees of volumes and put them in the detector store. Many tricks are available to compress the geometry at the GeoModel level. The size of the LAr Geometry prior to conversion can be monitored by checking the file GeoModelStatistics, which appears in the working directory when simulation is run. At present a nonsagging geometry requires 19M of memory (in GeoModel).

VI. THE ELECTROMAGNETIC BARREL GEOMETRY

This section describes the G4 simulation of the Electromagnetic calorimeter, as of 12.0.3[24] using the geometry described with GeoModel. The main parameters are listed as well as some known approximations. All the dimensions quoted are meant to be dimensions at cold. Only the barrel cryostat and its contents are discussed in detail here.

This description is organized as follows:

- Overview of the main envelopes and their alignment
- Description of the barrel cryostat
- Description of the presampler geometry
- Description of the calorimeter geometry
- Radiation length plots for the nominal geometry

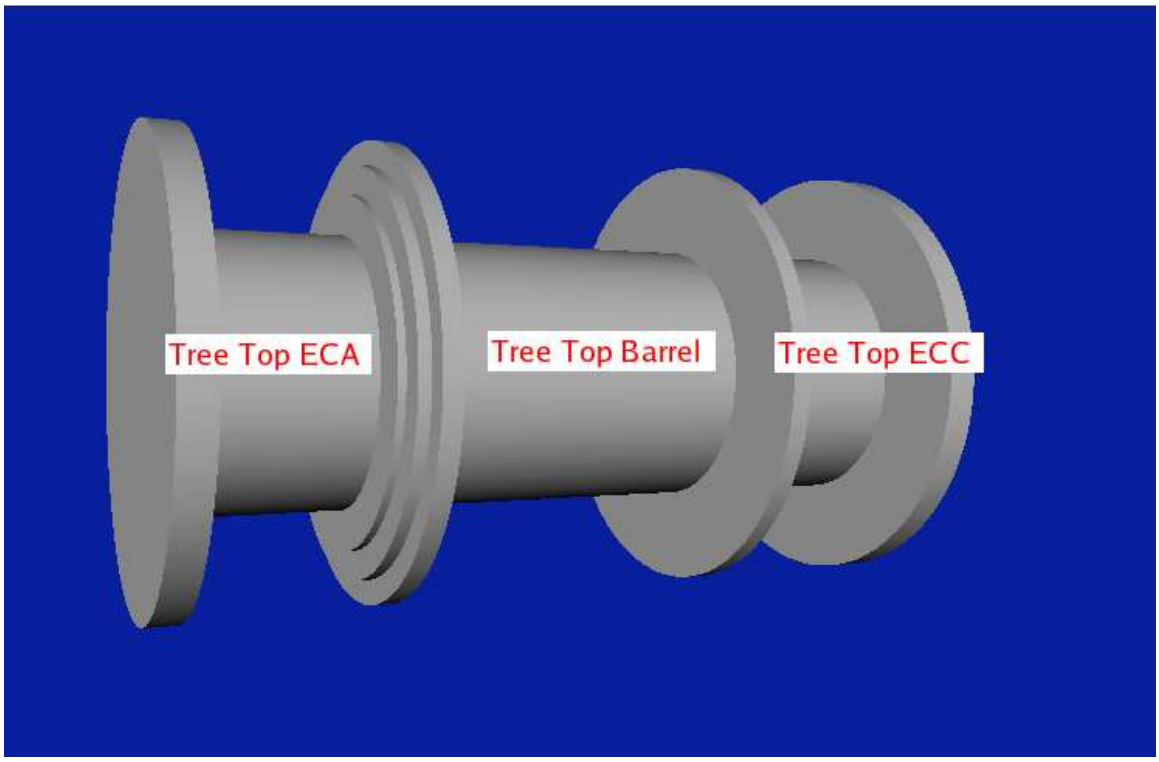

FIG. 3: *Top level volumes in the simulation of the LAr subcomponents. The center volume is the barrel which contains the EMB, and the outer volumes are endcaps containing the EMEC, HEC, and FCAL.*

- Overview of the matter-distorted geometry

A. Overview

The electromagnetic calorimeter and its cryostat are described by a set of volumes. Fig. 4 shows a view of the contents of the main envelope. In grey are the cables; services from the tracker as well as the front end electronics crate of the barrel calorimeter[12]. In red is the warm wall of the barrel cryostat. The structure of the envelopes is shown in Fig. 5.

The main envelope is made of Air. It covers a z range from -3521 to +3521 mm. For $|z| <$ 2849, the radius range is 1150 mm to 2250 mm. For the outer z parts, the maximal radius varies between 2930 mm and 3820 mm. The reason for the shape at large z and large radius is to contain the Front-End electronics crate within this main envelope, without conflict with

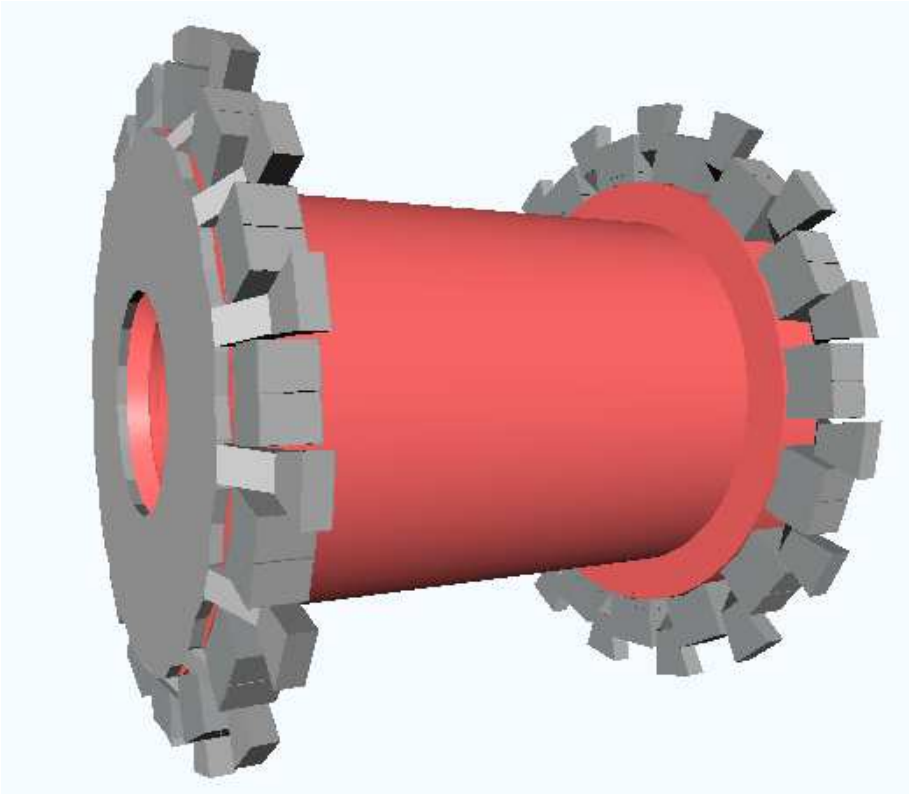

FIG. 4: *Overall view of the content of the main envelope*

the Tile Barrel and Extended Barrel envelopes. The high-z part of this envelope, which is outside the cryostat, also contains the description of the services and cables of the inner detector that run between the barrel and the end-cap cryostats.

This main envelope houses the cryostat elements (see section VI B, the Front-End electronics crate, the services/cables from the tracker and a LAr bath (shown in red). The total z range of the LAr bath is $\pm$3267 mm. The inner radius of the LAr bath is 1385 mm for $\pm$3101 mm in z, and 1565.5 mm at the extreme z values . The outer radius is 2140 mm.

The main LAr volume is divided into two parts for each half calorimeter. The sizes of these half LAr baths is smaller than the overall bath to allow to misalign each half LAr bath within the overall bath without conflict. The minimal z of the half LAr are $\pm$ 3 mm, maximum z is 3170 mm. The minimal radius is 1410 mm, the maximal radius is 2103.2 mm, except for $|z| < 90$ where it is 2003.5 mm (to allow space for an aluminum flange near z=0).

Each half LAr part houses an envelope for the presampler (LAr bath in which the presampler elements are placed) shown in magenta in Fig. 5 and an envelope for the accordion

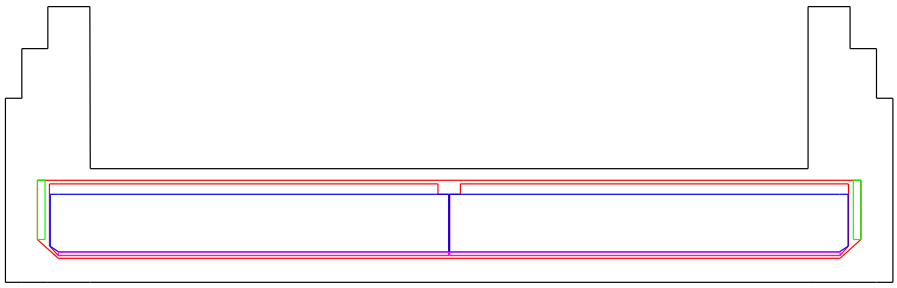

FIG. 5: *Overall envelopes used in the GEANT Monte-Carlo (see text)*

calorimeter (again LAr bath in which the various elements are placed), shown in blue on the figure.

The parameters used for the LAr material are a density of 1.396 g/cm^3 and atomic number A=39.948, giving a radiation length of 140.0 mm.

The outer steel support rings are located in the LAr half-barrel volumes, after the accordion envelope (see Fig. 6). In the same radial range, any motherboards and cables are located that were neglected in the description so far.

The main LAr bath also houses a tube at each end (from radius =1565.5 to 2140 mm and from z=3205 to 3267 mm) for the cables from the calorimeter, shown in green in Fig. 5. The material used for these cables is a mixture of C,H and LAr, with density 1.28 g/cm^3 (the realism of this description may need to be revisited).

1. Alignment

The following volumes can be misaligned (translation+rotation):

- The overall envelope in the Atlas global frame (LARCRYO_B in Table III)
- Each half-barrel LAr bath within the overall envelope (EMB_POS and EMB_NEG in Table III; each of these volume houses the presampler and the calorimeter which are moving together)
- The cylinders describing the solenoid (SOLENOID in Table III; see section VI B) in the overall envelope

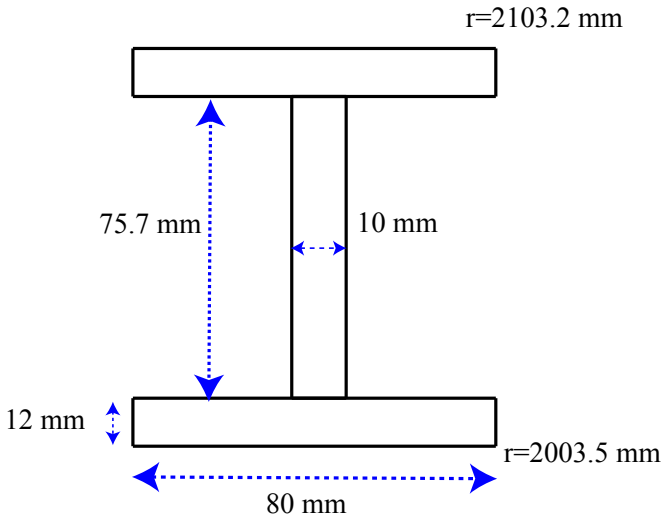

FIG. 6: *Steel outer ring, an I-beam strongback, in the z-r plane. 6 such rings are located at z=397, 809, 1255, 1750, 2316 and 2868 mm. The ring close to z=0 has a slightly different shape. The Al flange at z=0 for the cold vessel is also included in the simulation (*Δ *r=8.4 mm,Rmin=205.6 mm,* Δ *z=*$\pm$*7.2 mm*

The table below summarizes the values that have been chosen for the "misaligned" geometry for the CSC simulation (ATLAS-CSC-01-01-00 and ATLAS-CSC-01-02-00) (the rotation is specified by the θ and ϕ angles, in spherical coordinates, of the rotation axis, and the value of the rotation angle around this axis).

Element	Mother volume	Translation (mm)			Rotation (rad)		
		x	y	z	θ	ϕ	Angle
Cryostat	Atlas GLOB	0	2	4	0	0	0
Solenoid	Cryostat	0	-2	0	0	0	0
Half-Barrel z>0	Cryostat	2	-5	0	1.57075	0.46365	.00022
Half-Barrel z<0	Cryostat	-2	-3	0	0	0	0

B. Barrel cryostat

The cryostat description in GEANT was done by M.Leltchouk and W.Seligman, it was then adapted to GeoModel and improved by J.Boudreau and V.Tsulaia.

The GEANT description of the barrel cryostat is summarized in Fig. 7 and Fig. 8

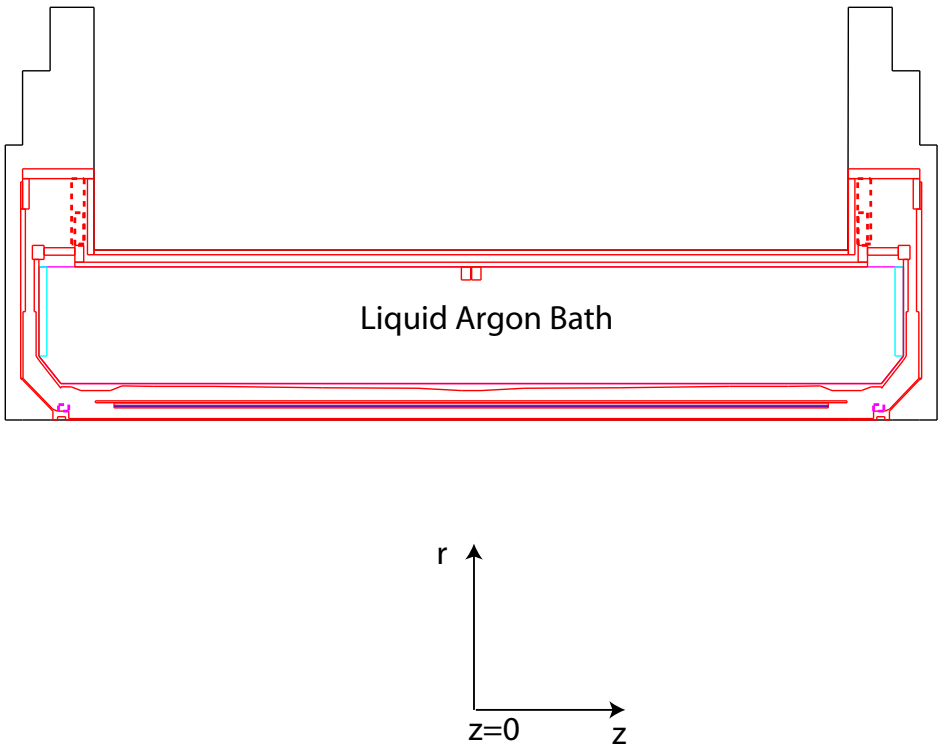

FIG. 7: *Description of the cryostat in the r-z plane (invariant under ϕ rotation). The red lines limit volumes in Al, the blue in Cu, the green in G10. Dashed lines show structures which cover only part in ϕ (see the following figure). The Al flange near z=0 and the volume for the LAr cable (in cyan) at high z are located within the main LAr bath volume.*

In the central z part, the Al inner warm vessel of the cryostat starts at r=1150 mm and has a thickness of 10 mm . The coil starts at 1229 mm and ends at 1275.535 mm. It is composed of layers of Al (12.8, 13.8 and 12 mm thick), Cu (3.05 mm) and G10 (4.7 mm). The Al inner cold vessel ends at r=1385 mm with a thickness varying with η (14 to 44 mm, see the figure). The outer Al cold vessel covers r=2140 to 2170 mm and the warm vessel 2220 to 2250 mm.

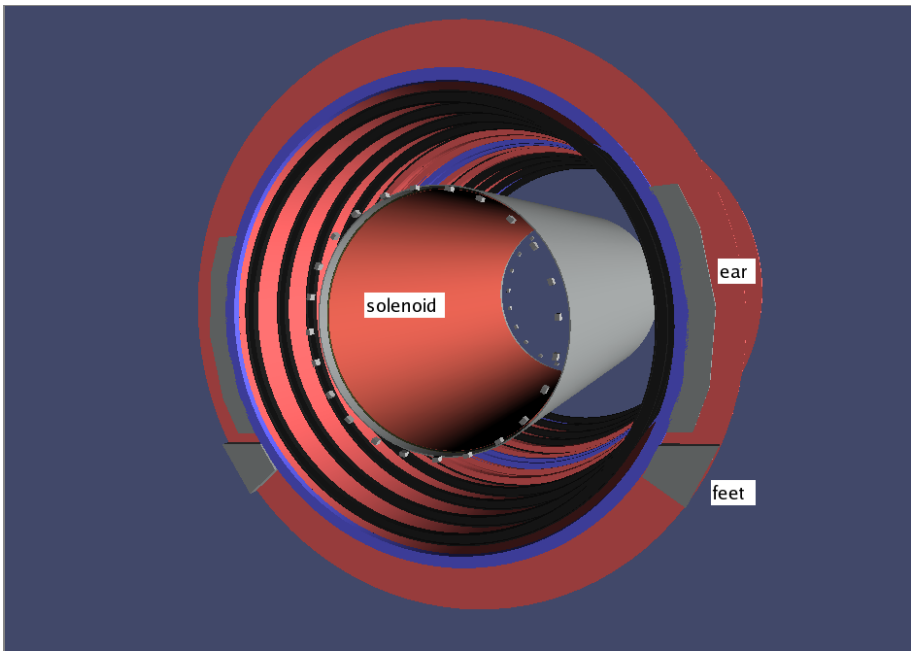

FIG. 8: *A view of the cryostat in which several support structures are visible. Aluminum "feet" welded to the warm vessel support the cold vessel via aluminum "ears". The gap is filled, in reality, with G10. Small titanium blocks, mounted to a beveled surface (not shown) on the warm vessel, support the solenoid which lies in the vacuum between the warm and cold vessels via (unmodified) G10 triangular straps.*

The ear and leg support at large z and large radius between the warm and cold vessels are shown in Fig. 8. They are made of Aluminum. The z thickness is 70 mm for the ear and 96 mm for the leg. The radial range is 2280-2490 mm for the ear and 2290-2710 mm for the leg. The upper and lower part of the ear are at $y = \pm 1004$ mm. The bottom of the leg is at ϕ=-37 deg. Support of the coil is provided by a series of titanium blocks welded onto the warm vessel, also visible in Fig. 8. Triangular supports made of G10 used to connect the coil to these blocks is presently not modeled in the simulation. A number of additional items are also not modeled, including:

- Additional Al plates (16 at each end, 25 mm thick) at high z and high radius between the cold and the warm vessels
- Feedthroughs/cables between the warm and cold vessel

- Some LAr bath at the high radius, high z part of the cryostat, near the feedthroughs

More details on dead materials within the LAr system itself can be found in Section XI A. Cables running from the inner detector to the electronics crates have a complicated composition. Both the electronics crates and the cables from the inner detector are visible in Fig. 4. The description of these cables has required a intense effort, and is documented separately in reference [12].

C. Presampler geometry

The barrel presampler description in GEANT comes from D.Benchekroun, it was adapted to GeoModel by V.Tsulaia.

The LAr envelope in which the presampler is located starts at r=1410 mm and stops at r=1447 mm (the beginning of the LAr envelope of the accordion calorimeter). Each half-barrel presampler has 32 sectors in ϕ. Each sector is a LAr volume of thickness 29.98 mm in which the various presampler elements are located. The centers of the sectors are located on a circle of radius 1426 mm (see Fig. 9).

The transverse view of a sector is shown in Fig. 10. The width is 276.91 mm at the inner edge and 282.42 mm at the outer edge. The protection shell (thickness 0.4 mm), protection plate (thickness 0.5 mm) and the rails (thickness 8.58 mm, width 23.92 mm) are made of FR4 (mixture of hydrogen, carbon and oxygen, density 1.9 g/cm^3, radiation length 211.08 mm). The motherboard (thickness 2.19 mm) is made of a mixture of FR4 and Copper (density 2.24 g/cm^3, radiation length 127.19 mm). The cable thickness varies linearly with z from 1.5 mm to 5 mm with a width varying from 2.8 mm to 168.56 mm. The cables are made of a mixture of copper, kapton, and liquid argon (density 3.98 g/cm^3, radiation length 45.43 mm). The supports between the sector and the calorimeter inner G10 rings are ignored. Eight modules of different z sizes are located in each PS sector (see Fig. 11).

Each module is a LAr volume in which the cathodes and anodes are located, as well as two prepreg plates (thickness 1 mm and 4.49 mm) made of FR4. The anode thickness is 0.329 mm and the cathode one is 0.2692 mm. They are made of a mixture of copper and FR4 (density 3.73 g/cm^3, radiation length 46.3 mm for the cathode, density 3.06 g/cm^3

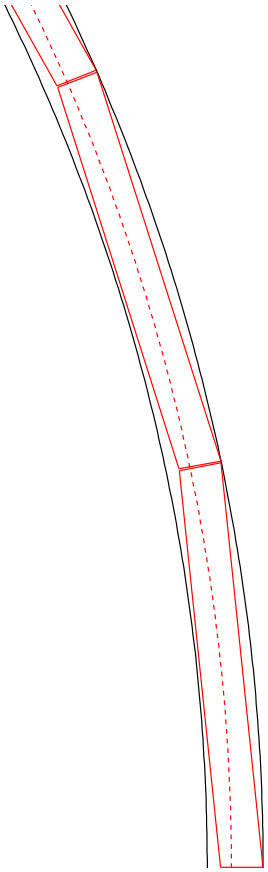

FIG. 9: *Position of the PS sectors inside the LAr envelope*

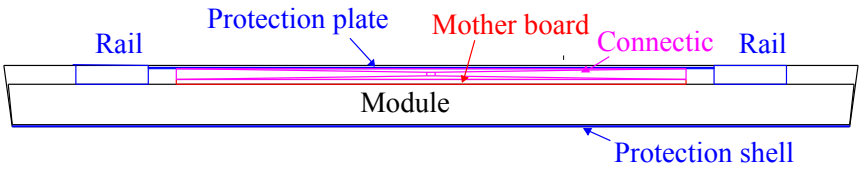

FIG. 10: *Transverse view of one PS sector*

radiation length 64.92 mm for the anode). The "active" LAr thickness in a module is 13 mm (see section VIII for a more detailed discussion).

Table IV shows the z length of each module, the number of cathodes, the z separation between the cathodes (there is an anode in between two consecutive anodes), the angle of the electrodes, the number of readout cells (regrouping several gaps) and the z of the beginning of the first cell of the module. Fig. 12 and 13 show the third module in z as an

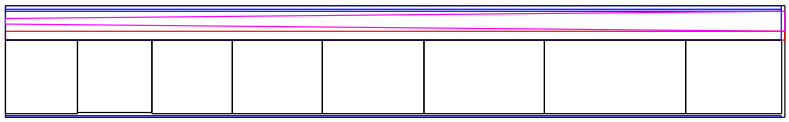

FIG. 11: *Longitudinal view of one PS sector (note that the vertical sale is 18 times bigger than the horizontal one)*

example. The beginning of the first module is at z=3 mm and the end of the last one at z=3082.13 mm.

TABLE IV: Parameters for the presampler modules

Module	length (mm)	N(catho.)	Δ(z) catho. (mm)	Angle (deg)	N(cell)	z first cell (mm)
1	285.67	56	4.974	25	8	3
2	294.99	64	4.609	12	8	288.67
3	320.28	72	4.448	0	8	583.65
4	355.89	80	4.448	0	8	903.93
5	403.76	88	4.588	0	8	1259.82
6	477.17	104	4.588	0	8	1663.58
7	561.75	128	4.387	0	8	2140.75
8	379.62	87	4.387	0	5	2702.5

D. Accordion calorimeter geometry

The calorimeter GEANT simulation was originally developed by G.Parrour and K.Kordas. The latest evolutions have been implemented by G.Unal

FIG. 12: *Transverse view of one PS module (the third in z)*

FIG. 13: *Longitudinal view of one PS module (the third in z)*

The mother envelope of a half-barrel is shown in Fig. 14. It is filled with LAr. It goes from r=1447 mm (after the presampler) to r=2003.5 mm (end of the G10 outer bar). The inner z value of 3 mm is the beginning of the absorbers and electrodes. There is thus a gap of $\pm$ 3mm at z=0 between the absorbers of the two half-barrels. The non-projectivity of the end of the barrel near η 1.475 is taken into account in the simulation, see Fig. 15 for a view of the structure of the barrel near η 1.475.

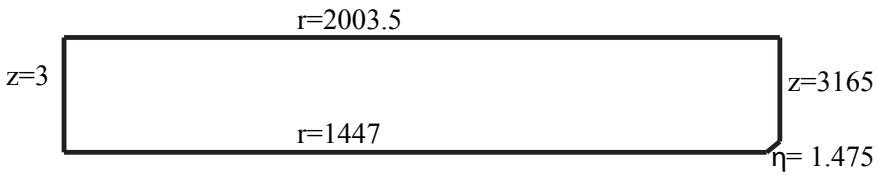

FIG. 14: *Overall parameters of the calorimeter envelope*

This mother volume is divided radially to create envelopes for the cables and motherboards, the front G10 bar, the accordion structure and the back G10 bar. This division is shown in Fig. 16. The small straight sections at the beginning and the end of the absorbers/electrodes are described in separate volumes as shown in the figure.

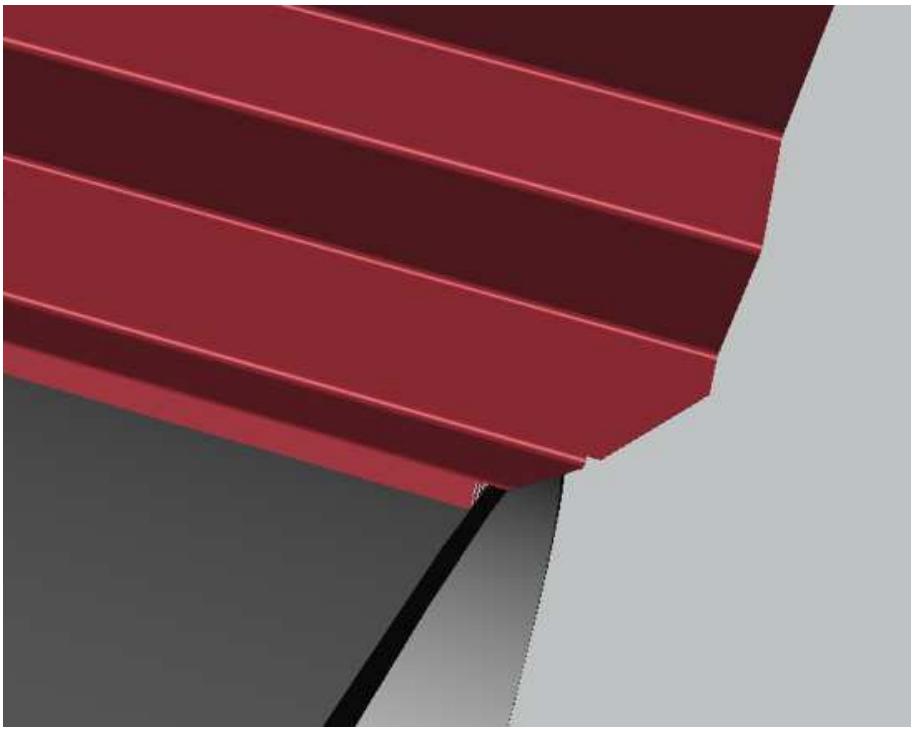

FIG. 15: *View of the high-η part of the calorimeter*

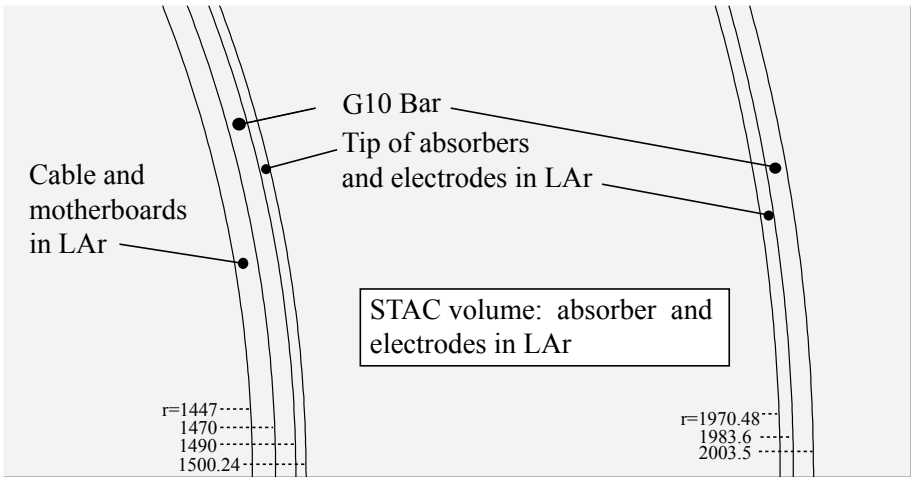

FIG. 16: *Radial subdivision of the volumes in the calorimeter envelope*

The description of the cables and motherboard follows the description written in[13]. An effective mixture for the summing board effect has been included. A zoom of the structure of this area for one module can be found in Fig. 17.

The thickness of the motherboard is 4.3 mm. It is described by a mixture of Cu and

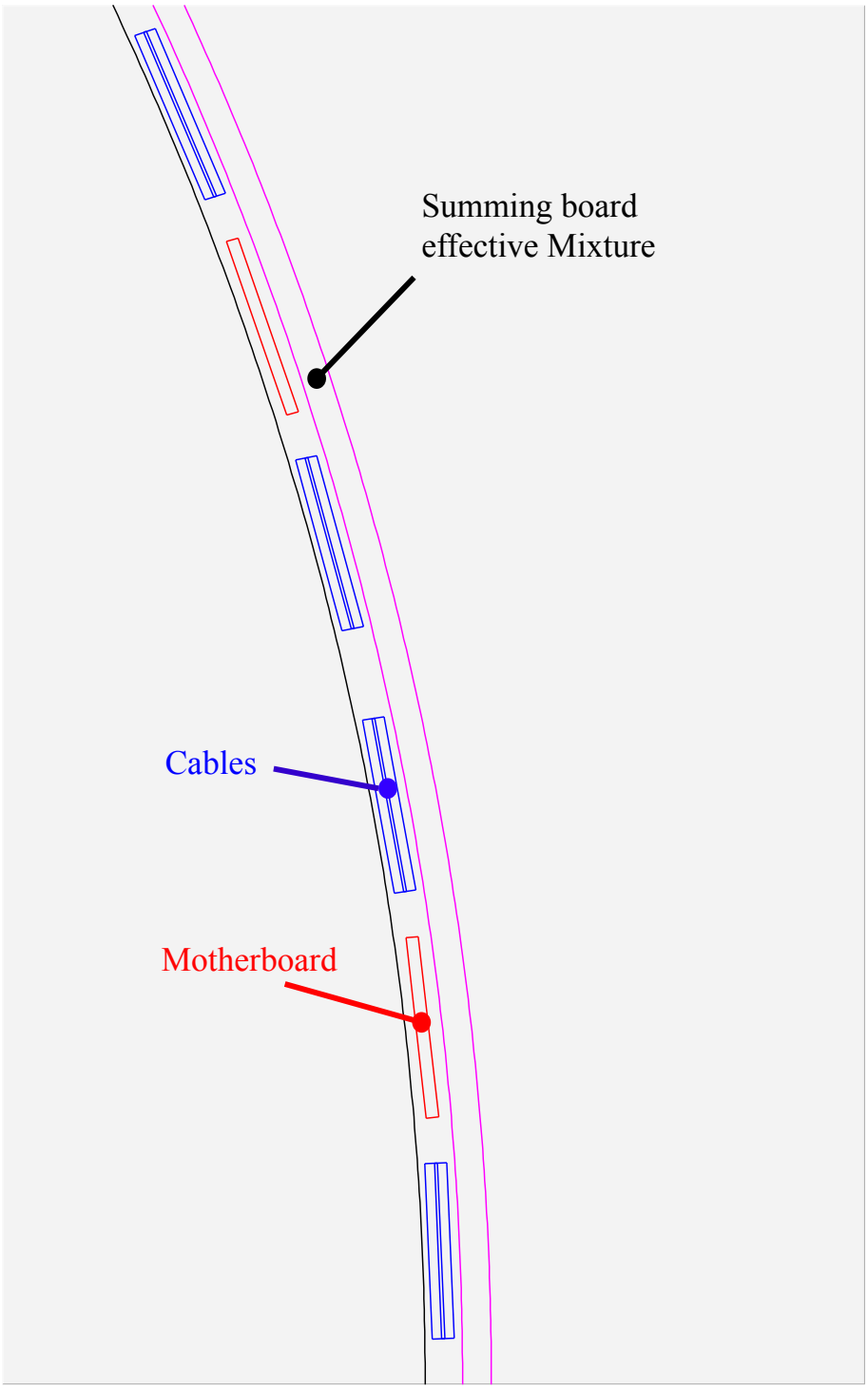

FIG. 17: *Cable and motherboard structure for one module in ϕ*

G10 given a density of 2.849 g/cm^3 and a radiation length of 71.32 mm. The thickness of the cable varies linearly with z from 1 to 7.2 mm. The cables are described by a mixture

of Cu and Kapton given a density of 3.04 g/cm^3 and a radiation length of 57.30 mm. The summing board+LAr is described by an effective mixture (thickness 10 mm) of Cu and Ar given density of 1.608 g/cm^3 and a radiation length of 112.51 mm.

The G10 for the inner and outer bars has a density of 1.72 g/cm^3 and a radiation length of 179.5 mm. The thickness is 20 mm.

The accordion structure extends from r=1500.24 mm to r=1970.48 mm (starting at the first fold and ending at the last fold). It is a LAr bath in which the individual elements for the electrodes and the absorber are positioned. The electrodes and absorbers follow the same accordion shape (see Fig. 18), with different thicknesses (2.21 mm for the absorber and 0.275 mm for the electrodes). The absorber thickness corresponds to the average value given in the Barrel construction NIM paper[14]. The electrode is made of a mixture of Cu and Kapton, giving a density of 4.3236 g/cm^3 and a radiation length of 34.744 mm. The absorbers are made of a mixture of lead, iron and glue[25]. For η less than 0.8, the mass fractions are 0.8254, 0.1517, and 0.0229, respectively, giving a density of 9.4749 g/cm^3 and a radiation length of 7.4735 mm. For η above 0.8, the mass fractions are 0.7466, 0.1859, and 0.0675 giving a density of 7.7326 g/cm^3 and a radiation length of 9.7506 mm. In this case, the values for the thickness and the density are the values at warm. A contraction factor of 0.997 is used to obtain the cold characteristics (the thickness is reduced by this factor and the density is increased by the cube of this factor). Note that in the absorber structure a mixture is used and that the actual structures (lead and glue sandwiched between the steel skins) are not described in full detail. Even if the overall radiation length is the same, this could have a small effect on the signal visible in LAr (as the interaction of low energy electrons and photons depends on Z of the material). From a full simulation of a simple parallel-plate geometry, this seems to be a small effect. The free space between absorbers and electrodes is filled only with the LAr bath, and the effect of the honeycomb is neglected. This will change by few % (volume effect) the signal in LAr, but should have a negligible effect on shower development and shower shape.

The absorber or electrode geometry is described in its internal frame, in which the x axis points along the axis of the absorber/electrode, oriented along the vector connecting the two endpoints of the accordion but originating near the origin of ATLAS coordinates. In this frame, positions of the center of the circle corresponding to the folds are specified.

The radius of the fold (radius of the circle at the mid-line of the material) is 2.78 mm (see Fig. 19). The values (ρ,ϕ) in cylindrical coordinates of the center of the fold are summarized in table V.

TABLE V: Parameters for the accordion geometry. The ϕ values are computed in the internal frame, as defined in the text. The table applies to both electrodes and absorbers.

fold number	ρ (mm)	ϕ (deg)
0	1500.02	0.10619
1	1521.00	0.569751
2	1559.66	-0.573092
3	1597.20	0.576518
4	1634.57	-0.579943
5	1671.02	0.582296
6	1707.43	-0.585638
7	1743.07	0.588207
8	1778.67	-0.590596
9	1813.75	0.59285
10	1848.87	-0.595587
11	1883.36	0.59744
12	1918.02	-0.599714
13	1952.10	0.601911
14	1970.48	0.0811661

The 1024 absorbers and electrodes are positioned in the LAr by applying rotations in ϕ.

The small straight sections at the beginning (Δr=10 mm) and at the end (Δr=13 mm) of the accordion are described by placing small representative boxes in the LAr volume. For the front part, the Lead of the absorber is replaced by G10 for most of the radial space. In this case, the detailed structure with the steel plate is described (as shown in Fig. 20), since the steel plate changes the average radiation length before the active volume by 2% X_0 (45% X_0 for 4.3% of the solid angle). Since this part of the structure is projective and the

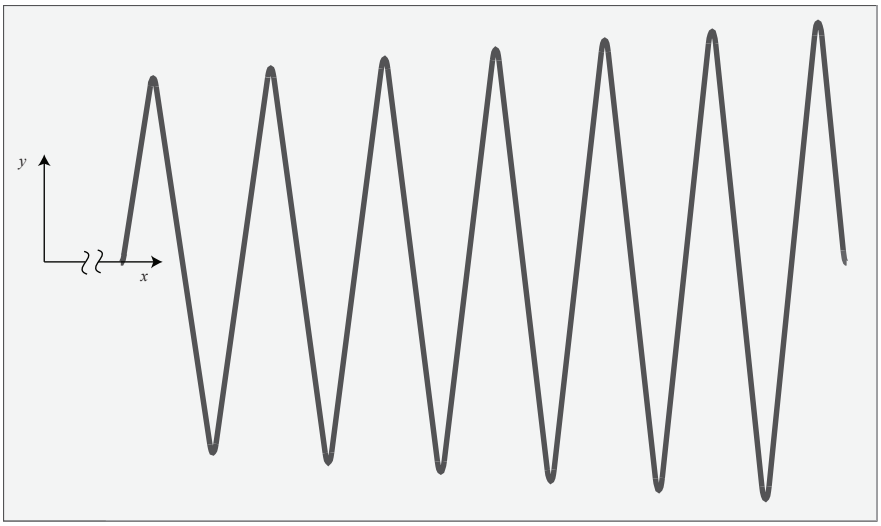

FIG. 18: *Overview of non-sagging accordion structure. Note that the y scale is 10 times expanded compared to the x scale.*

showers are very narrow at their beginning, this detailed description has been found to have a slight impact on the ϕ modulation of the energy response.

The transition at η=0.8 in the lead plates forms a straight projective line on the plate before folding. After folding, the transition on no longer at fixed η but varies with radius as shown in Fig. 21. This is accurately described in the geometry description.

In the simulation, the ϕ=0 axis of the nominal geometry is an electrode axis. The electrodes and absorbers run along the positive ϕ direction in the positive z barrel and, because of a relative rotation between the two barrels, in the negative ϕ direction in the negative-z barrel. The first absorber of the first cell is located before the first electrode, so its ϕ-position is at -$2\pi/2048$ for the positive-z barrel and $+2\pi/2048$ for the negative z barrel.

1. Sagging deformation

Sagging of the absorbers under the action of gravity is implemented in the accordion geometry (this is an option which is not active by default and is not turned on in the CSC production geometries). The mechanical sagging of absorber planes was computed recently at Orsay by A.Gallas with a finite element method. In this computation it is assumed

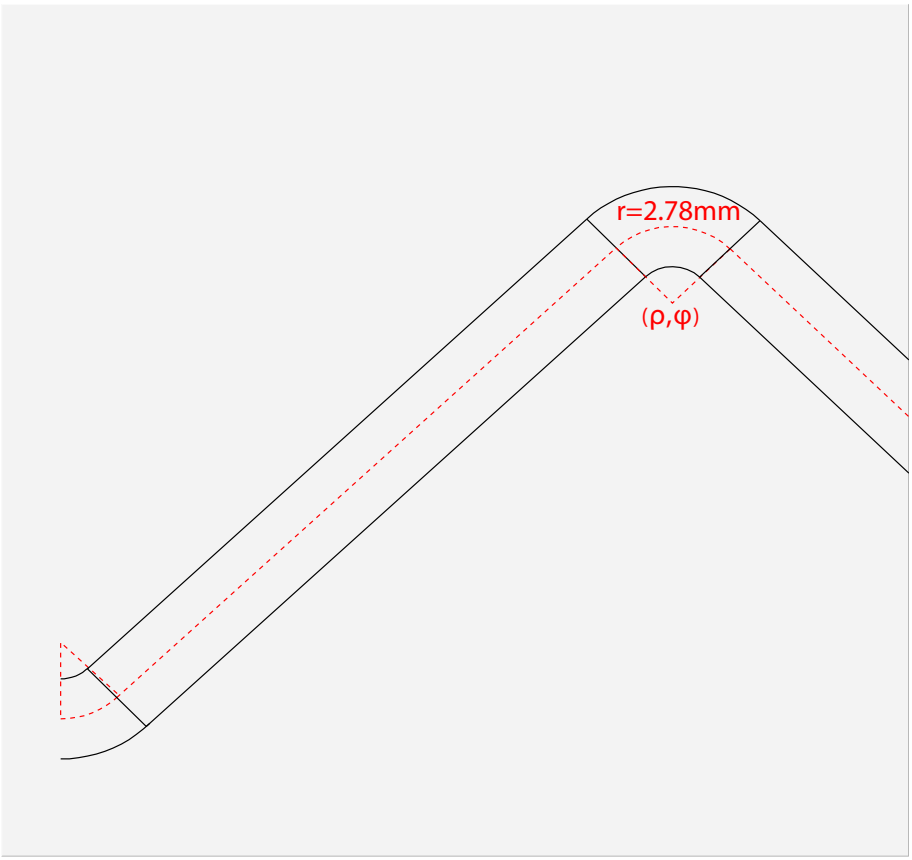

FIG. 19: *Detail of the accordion structure of one absorber. The electrode shape is the same with a different thickness.*

that the inner radial and outer radial part of the absorbers remain in place and that the G10 rings stay perfectly circular. The sagging is described by a move in x-y local frame of each of the fold of the absorber (in the local frame, the x-axis is the absorber axis). This computation was repeated for different orientations of the absorber. The maximal amplitude was normalized to the 1.2 mm displacement measured on a real absorber (the maximum sagging amplitude in the computation is 0.75 mm). The values of δx and δz for the folds of the absorber at ϕ=0 are given in the following table

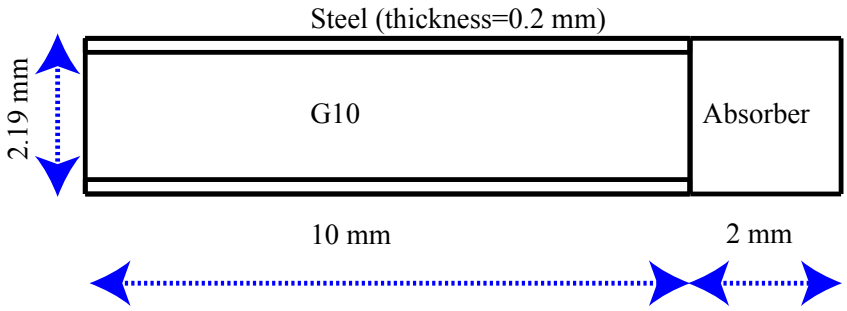

FIG. 20: *Detail of the description of the front tip of the absorber, between the inner G10 cylinder and the first accordion fold*

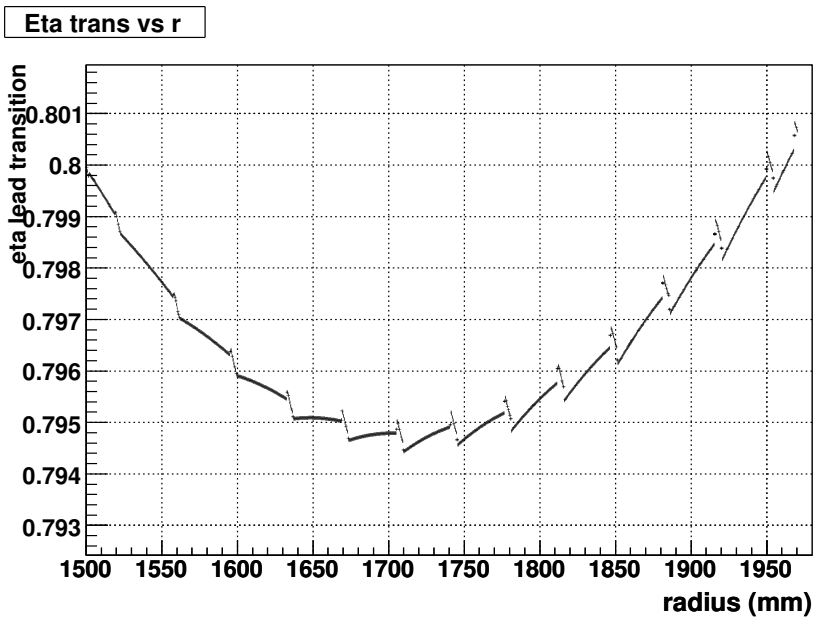

FIG. 21: *Transition between lead thicknesses in η (Atlas) as a function of radius, after folding of the absorber plate.*

Fold	δy (mm)	δx (mm)
0	0	0
1	-0.064	0.032
2	-0.256	-0.128
3	-0.528	0.128
4	-0.8	-0.144
5	-1.008	0.144
6	-1.168	-0.064
7	-1.20	0
8	-1.152	0.064
9	-1.008	-0.112
10	-0.768	0.16
11	-0.512	-0.16
12	-0.256	0.176
13	-0.064	-0.064
14	-0	0

For an absorber axis at ϕ=0, the δy values are obviously all negative and the maximal amplitude is at the middle of the absorber. The δx values arise because the total length of the absorber straight sections remains constant. For an arbitrary ϕ axis, the x and y amplitudes in the absorber frame scale with $\cos\phi$

From the displacements above, the geometry of all the elements of the accordion structure can be easily recomputed (assuming that the fold radius is constant, the fold positions and the fold radius are enough to completely constrain the accordion geometry).

Fig. 22 shows an example of the geometry after sagging, with the sagging amplitude magnified by a factor 10 for visibility.

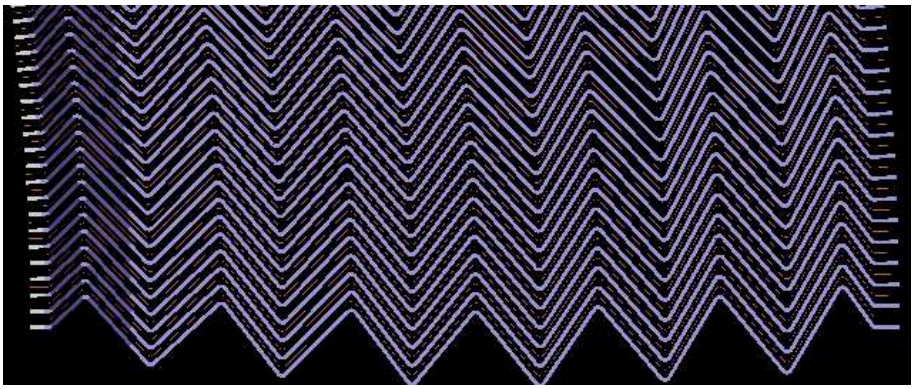

FIG. 22: *view of the accordion structure with sagging (amplified by a factor 10)*

E. Number of radiation lengths

The number of radiation lengths for various parts of the setup described above is estimated from geantino scans in GEANT4.

Fig. 23 shows the distribution of radiation lengths as a function of radius at η=0.1. The structures of the cryostat are clearly visible.

Fig. 24 shows the integrated radiation length distribution as a function of radius for tracks coming from the primary vertex for different η positions (only the contribution from the LAr calorimeter and the cryostat is included).

Fig. 25 shows the amount of radiation length before the beginning of the active presampler layer, as a function of ϕ (over one calorimeter module) for various η. The structure at the

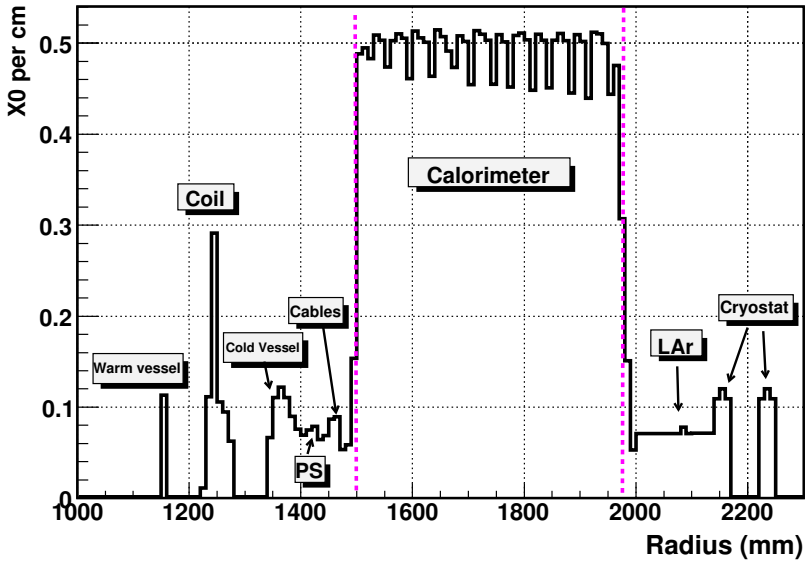

FIG. 23: *X_0 as a function of radius at η=0.1*

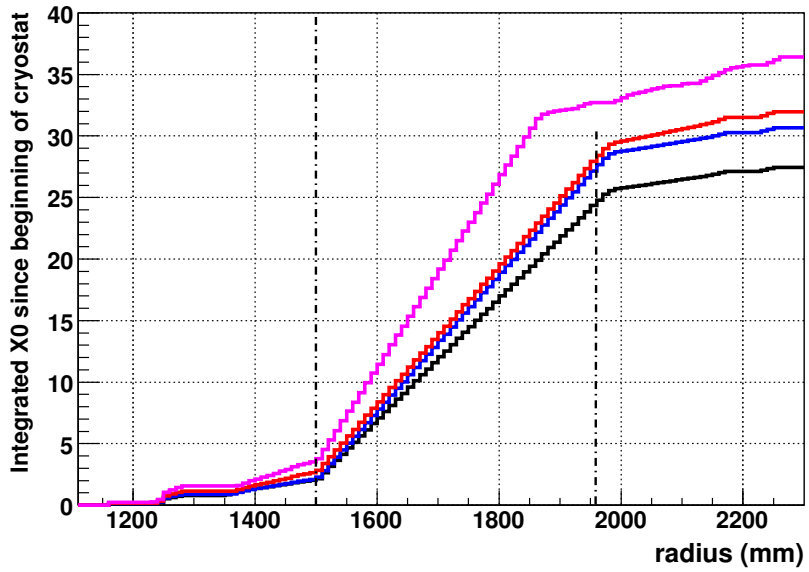

FIG. 24: *Integrated X_0 as a function of radius at η=0.1 (black), 0.5 (blue), 0.9 (red) and 1.3 (magenta)*

middle of the module is because there is a small crack in the presampler between two presampler modules and at this particular ϕ the beginning of the active PS layer is not

well defined. Fig. 26 shows the amount of radiation length between the PS active layer (included) and the beginning of the sensitive area of the calorimeter. The structure in ϕ from the cables and motherboards is clearly visible, as well as the effect of the tips of the absorbers. The details of the region with the cables and motherboard can be seen in Fig. 27.

Fig. 28 shows the detail of the amount of radiation length in the inactive part between the end of the G10 inner bar (r=1490 mm) and the beginning of the LAr sensitive region (r=1500.24 mm) as well as the number of radiation lengths in the LAr sensitive area (at η=0.05) as a function of ϕ, over one readout cell. Fig. 29 shows the amount of radiation lengths in the radial range corresponding to the sensitive area (1500.24 to 1960 mm) for the Liquid Argon and the inactive material (absorbers+electrodes). The small remnant effect from the accordion structure is clearly visible.

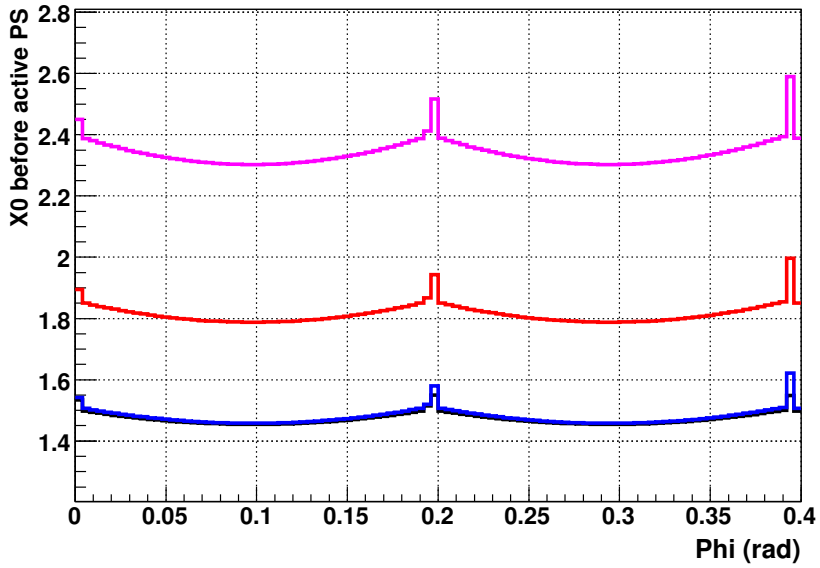

FIG. 25: *X_0 before active PS layer at η=0.1 (black), 0.5 (blue), 0.9 (red) and 1.3 (magenta)*

Fig. 30 shows the amount of radiation length as a function of z for a track at η=1.4 . Fig. 31 shows the total integrated matter from the description in the barrel overall envelope as a function of η.

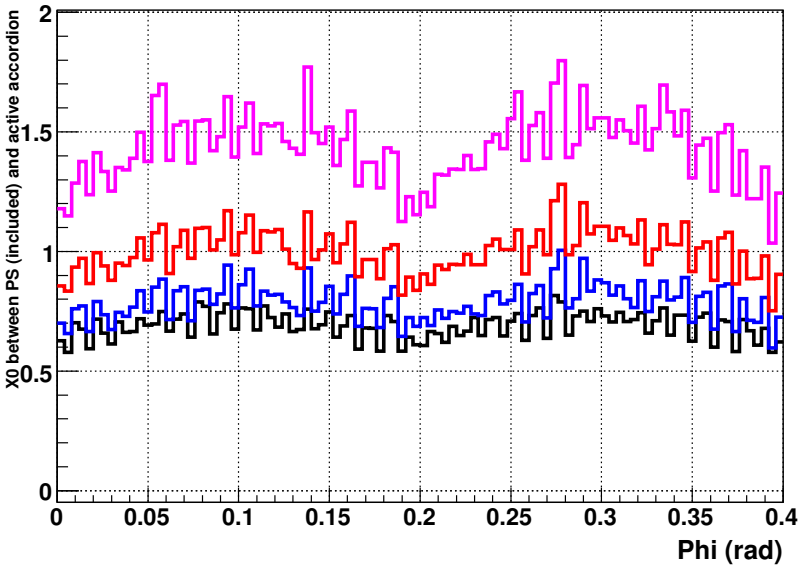

FIG. 26: X_0 *between active PS layer (included) and sensitive region of the accordion calorimeter at* η*=0.1 (black), 0.5 (blue), 0.9 (red) and 1.3 (magenta)*

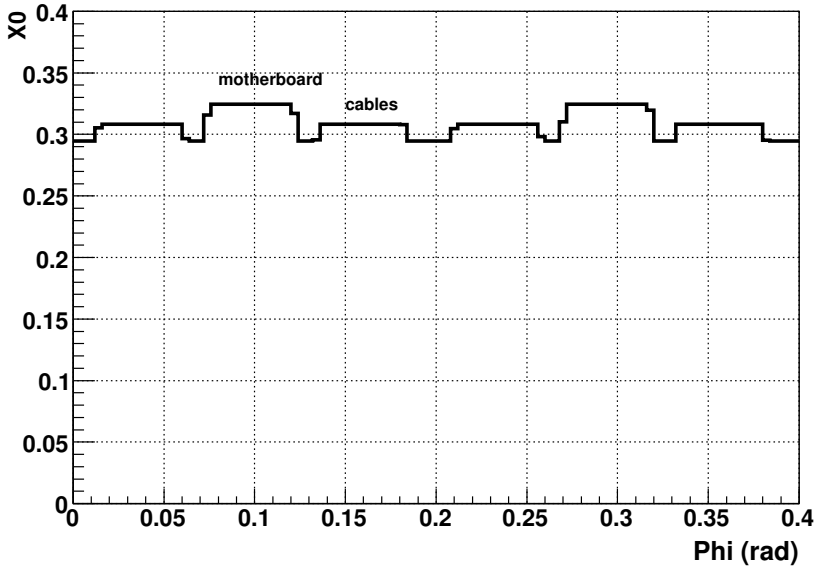

FIG. 27: X_0 *in the region of the cables/motherboard (1470*$<$ *r* $<$*1490 mm) before the sensitive region of the accordion calorimeter as a function of* ϕ *for* η*=0.1*

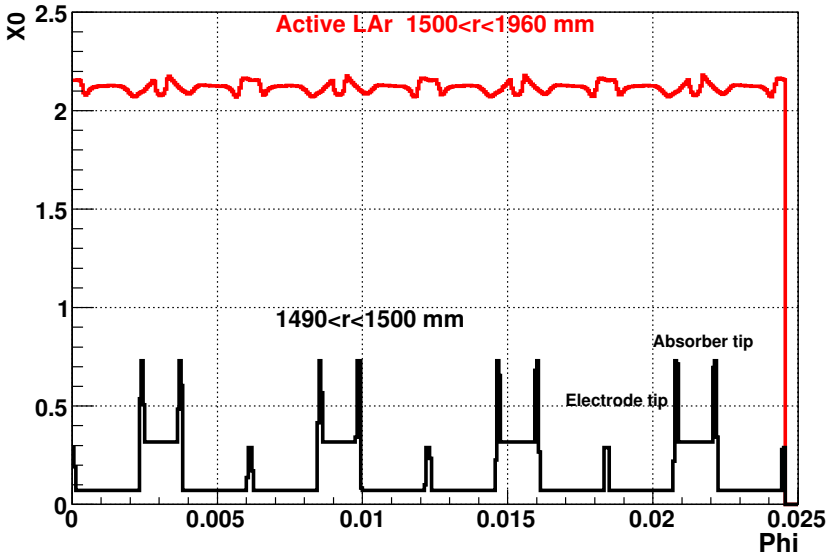

FIG. 28: *X_0 in the region of the tip of the absorber/electrodes (after the G10 inner bar) and total X_0 in sensitive Liquid Argon, as a function of ϕ for η=0.10*

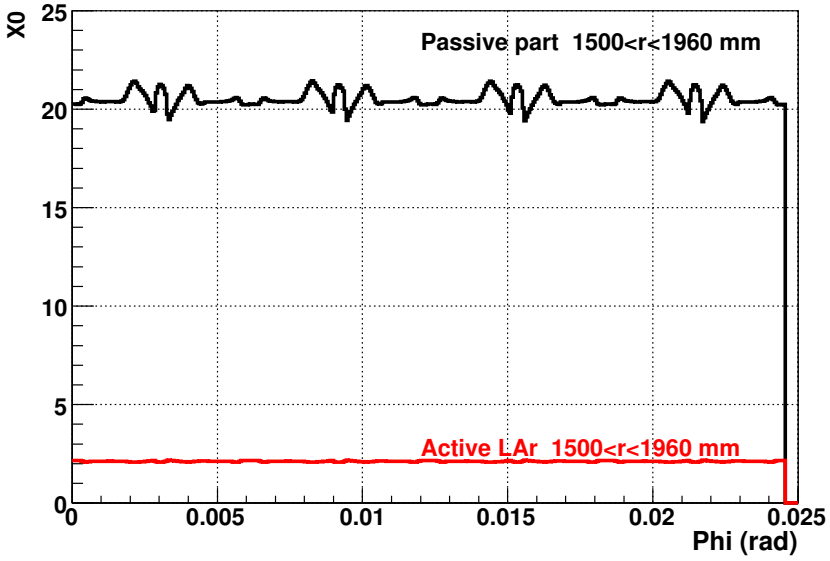

FIG. 29: *X_0 in sensitive LAr and in passive material in the accordion region (1500.24<r<1960 mm) for η=0.1*

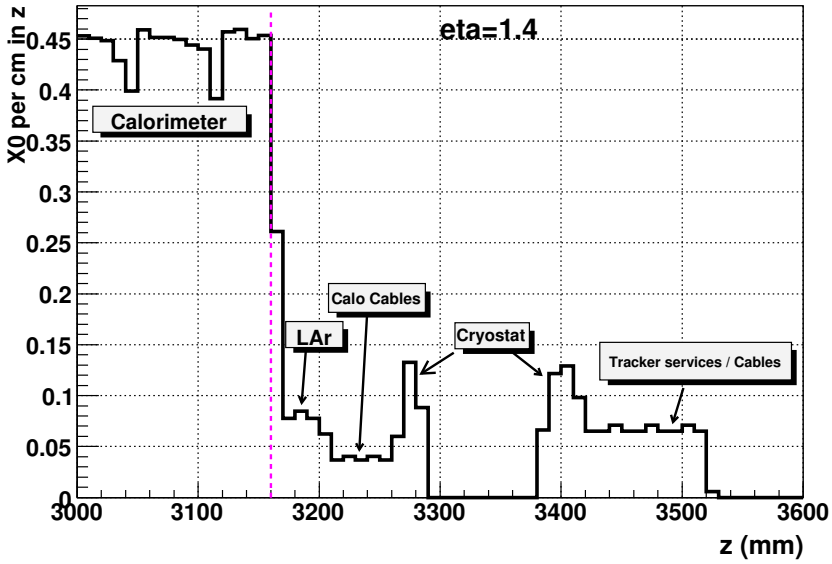

FIG. 30: *Radiation length as a function of z, seen by a track coming from the vertex at η=1.4.*

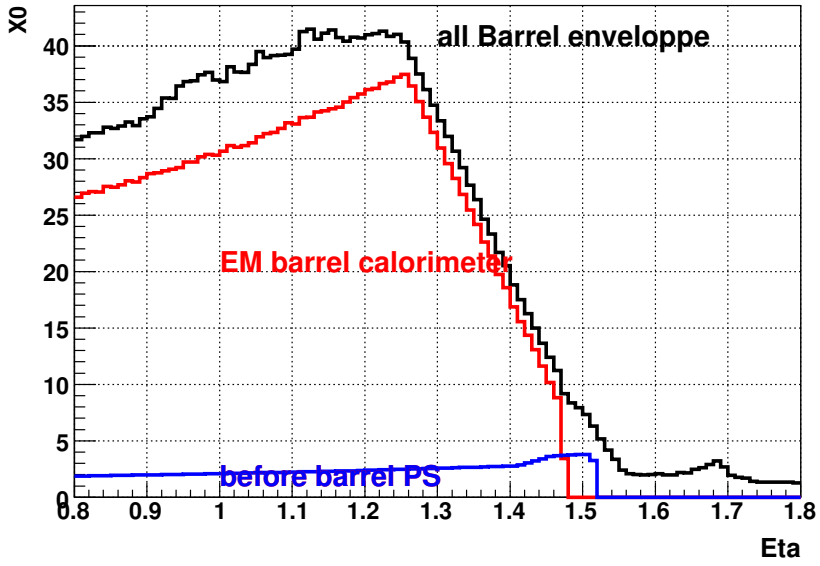

FIG. 31: *Total number of radiation lengths seen by a track coming from the primary vertex as a function of η, for the overall matter in the barrel em envelope (black), the matter up to the end of the active part of the calorimeter (red), and the matter up to the barrel presampler (blue).*

F. Overview of matter-distorted geometry

In the geometry ATLAS-CSC-01-02-00, additional material has been added compared to the one described above to investigate systematic effects. For the EM calorimeter, the additional material is the following:

- Additional material in the barrel cryostat upstream of the presampler. For $\eta > 0$ and all ϕ, one additional layer giving 8-11% X_0 radial (linear variation between eta=0 and eta=1.4).
- Additional material between the presampler and the accordion. At $\eta > 0$ for ϕ between $\pi/2$ and $3\pi/2$, and at $\eta < 0$ for ϕ between $3\pi/2$ and $\pi/2$, 5% X_0 radial added in one thin layer of lead.
- Additional material inside the cryostat downstream from the calorimeter. For $\eta > 0$, 7-11% X_0 radial is added (this should be more than what is missing from not describing the motherboards and cables at the downstream end of the calorimeter).
- Density of the material in the gap barrel-endcap cryostats increased by a factor 1.7, from nominal values described in reference[12], which should be an "extreme" change.

G. List of geometry parameters taken from the database

name	value for Atlas	TB value
(absorber)		
LArEMBThinAbsGlue	0.0679 cm	same
LArEMBThinAbsIron	0.04 cm	same
LArEMBThinAbsLead	0.1131 cm	same
LArEMBThickAbsGlue	0.0278 cm	same
LArEMBThickAbsIron	0.04 cm	same
LArEMBThickAbsLead	0.1532 cm	same
ABSORBERCONTRACTION	0.997	same

```
(electrodes)
LArEMBThickElecCopper   0.0105 cm        same
LArEMBThickElecKapton   0.0170 cm        same

(matter PS to strips)
LArEMBEpoxyVolumicMass   1.8 g/cm3       same
LArEMBmasspercentCu      62%             same
LArEMBmasspercentKap     38%             same
LArEMBCuThickness        0.063 cm        same
LArEMBG10Thickness       0.367 cm        same
LArEMBInnerElectronics   2.3   cm        same
LArEMBG10SupportBarsIn   2.0   cm        same
LArEMBMoBoTchickness     0.43  cm        same
LArEMBMoBoHeight         7.23  cm        same
LArEMBCablethickat0      0.1   cm        same
LArEMBthickincrfac       0.517 cm        same
LArEMBCableEtaheight     7     cm        same
LArEMBnoOFmothboard     32                   2
LArEMBMoBoclearfrPS      0.6   cm        same
LArEMBnoOFcableBundle   64                   4
LArEMBCablclearfrPS      0.6   cm        same
LArEMBLeadTipThickFront  0.2   cm        same
LArEMBG10TipThickFront   0.8   cm        same

(matter after accordion)
LArEMBLeadTipThickEnd    1.3   cm        same
LArEMBG10TipThickEnd     0.0   cm        same
LArEMBLArGapTail         1.3   cm        same
LArEMBG10SupportBarsOut  2.0   cm        same
```

```
(overall geometry)
LArEMBAbsPhiFirst     -2pi/2048            0
LArEMBMotherZmin          0.3  cm         same
LArEMBMotherZmax        316.5  cm         same
LArEMBMotherRmin        144.7  cm         same
LArEMBMotherRmax        200.35 cm         same
LArEMBphiMaxBarrel      360    deg        22.5
LArEMBnoOFAccZigs        14               same
LArEMBMaxEtaAcceptance   \EMBMaxEta           same
LArEMBThickEtaAcceptance 0.8              same
LArEMBnoOFPhysPhiCell   1024                64
LArEMBPhiGapAperture   0.3515625 deg      same


(active electrode region)
LArEMBfiducialMothZmax      316.4 cm      same
LArEMBfiducialMothZmin        0.4 cm      same
LArEMBRadiusInnerAccordion  150.0024 cm   same
LArEMBFiducialRmax          196.0 cm      same

(accordion   shape)
LArEMBNeutFiberRadius        0.278 cm     same
LArEMBRadiusAtCurvature[0]   150.002 cm   same
LArEMBRadiusAtCurvature[1]   152.1        same
LArEMBRadiusAtCurvature[2]   155.966      same
LArEMBRadiusAtCurvature[3]   159.720      same
LArEMBRadiusAtCurvature[4]   163.457      same
LArEMBRadiusAtCurvature[5]   167.102      same
LArEMBRadiusAtCurvature[6]   170.734      same
LArEMBRadiusAtCurvature[7]   174.307      same
LArEMBRadiusAtCurvature[8]   177.876      same
```

```
LArEMBRadiusAtCurvature[9]    181.375       same
LArEMBRadiusAtCurvature[10]   184.887       same
LArEMBRadiusAtCurvature[11]   188.336       same
LArEMBRadiusAtCurvature[12]   191.802       same
LArEMBRadiusAtCurvature[13]   195.210       same
LArEMBRadiusAtCurvature[14]   197.048       same
LArEMBPhiAtCurvature[0]      0.106187 deg   same
LArEMBPhiAtCurvature[1]      0.569751       same
LArEMBPhiAtCurvature[2]     -0.573092       same
LArEMBPhiAtCurvature[3]      0.576518       same
LArEMBPhiAtCurvature[4]     -0.579943       same
LArEMBPhiAtCurvature[5]      0.582296       same
LArEMBPhiAtCurvature[6]     -0.585638       same
LArEMBPhiAtCurvature[7]      0.588207       same
LArEMBPhiAtCurvature[8]     -0.590596       same
LArEMBPhiAtCurvature[9]      0.59285        same
LArEMBPhiAtCurvature[10]    -0.595587       same
LArEMBPhiAtCurvature[12]     0.59744        same
LArEMBPhiAtCurvature[12]    -0.599714       same
LArEMBPhiAtCurvature[13]     0.601911       same
LArEMBPhiAtCurvature[14]     0.0811661      same
LArEMBDeltaZigAngle[0]      46.2025 deg     same
LArEMBDeltaZigAngle[1]      45.0574         same
LArEMBDeltaZigAngle[3]      43.3446         same
LArEMBDeltaZigAngle[3]      42.4478         same
LArEMBDeltaZigAngle[4]      40.9436         same
LArEMBDeltaZigAngle[5]      40.2251         same
LArEMBDeltaZigAngle[6]      38.8752         same
LArEMBDeltaZigAngle[8]      37.0608         same
LArEMBDeltaZigAngle[9]      36.5831         same
LArEMBDeltaZigAngle[10]     35.4475         same
```

LArEMBDeltaZigAngle[11]	35.0556	same
LArEMBDeltaZigAngle[12]	33.9977	same
LArEMBDeltaZigAngle[13]	33.6767	same

VII. THE ELECTROMAGNETIC ENDCAP GEOMETRY

A. Geometry Overview

The electromagnetic endcap (EMEC) calorimeter is at the front of the liquid argon bath inside the endcap cryostat. It is built as two concentric plug-shaped wheels, called the inner wheel and the outer wheel. Within each wheel folded absorbers alternate with folded electrodes whose traces, after folding, follow straight lines at particular angles (i.e. η) with respect to the axis of the calorimeter. The electrodes and absorbers are organized in an axial arrangement as shown in Fig. 32 and the signals from several neighboring electrodes are ganged together, forming a projective cell which is a ϕ slice of a radial slice of the wheel. The ϕ boundaries are not sharp, but follow the wavy shape of the folded electrode.

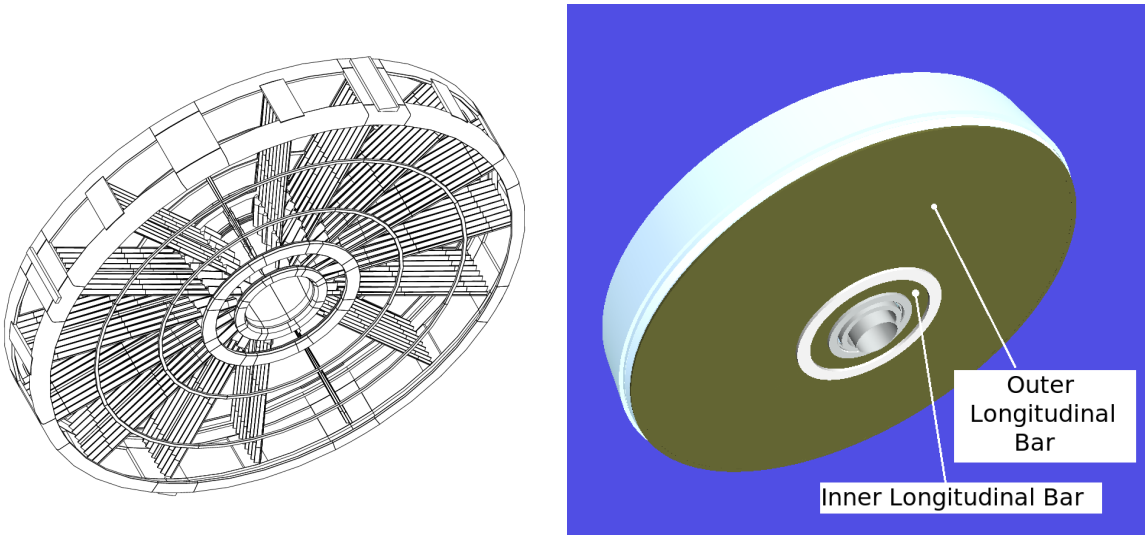

FIG. 32: *The EMEC volume, shown in two views. Some the folded fan absorbers are shown on the left. These are anchored, at the front and back, to so-called "longitudinal bars" made from G10, shown on the right. The back surface of the front longitudinal bar is an important positional reference for the EMEC.*

Before giving dimensions we describe precisely important positional references within the EMEC. The most precise reference point in the EMEC is a ring-shaped assembly at the front of the EMEC known as the front longitudinal bars which are constructed from G10

and which support the absorbers and connect the electrodes. The back surface of each front longitudinal bar is the main mechanical reference point for the EMEC.

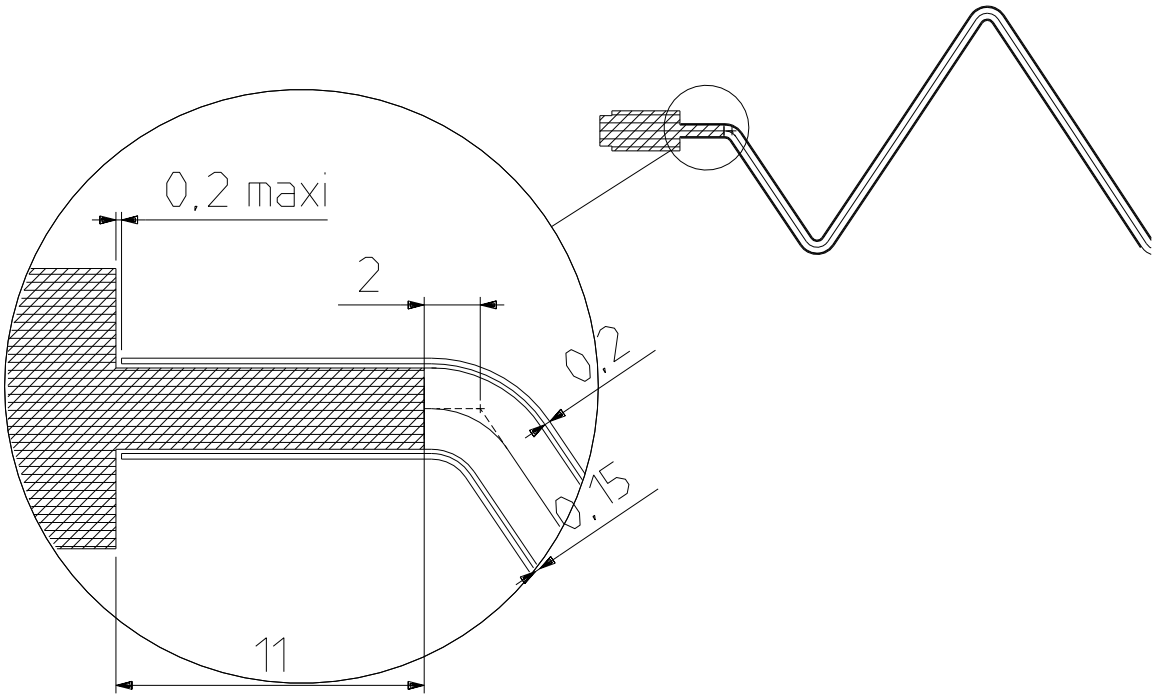

FIG. 33: *Detail of the first fold of the EMEC Electrode. The "barrette" attaches the electrode and creates a dead region over an 11 mm length.*

The location of the first fold in the EMEC, shown in Fig. 33, is also the start of its active region, where sensitive copper traces are applied to the surface of the kapton electrode. A similar structure at the other end of the electrode, near the back of the EMEC, determines the end of the active region.

The EMEC was designed to have projective cells. As ATLAS was under construction, it became clear that a larger crack between barrel and endcap calorimeter was needed for the placement of cables, so the entire endcap cryostat was shifted outward from its design

position by z=40 mm. Because of this shift and, to a lesser extent, because of additional misalignments, the cells do not project to the interaction point. Therefore the description of the EMEC is formulated in terms of a "focal point" which does not coincide with the interaction point.

Let θ be the angle between the axis of the calorimeter and the cell boundaries and let $\eta = \ln \tan \theta/2$. Because of the nonprojectivity described above, η is only approximately equal to the pseudorapidity of particles from the interaction point; the true significance of the cell η boundary values is that they are engineering numbers for the EMEC. The lines meet at a point in space that depends upon the temperature of the electrode. The place where the lines of a cold EMEC cross is called the electrical focal point. From the location of that point and the η values of the cell boundaries one can work out the radial coordinate of a point at which the boundaries intercept any plane in z (such as the start of the active region).

The separation between the inner wheel and outer wheel occurs at $\eta = \eta_{mid}$. The inner edge of the outer wheel, and the outer edge of the inner wheel are defined by conical surfaces parallel to this separation but displaced radially by 1.5 mm (out, or in) from it, forming a gap. The inner wheel has a conical inner boundary at $\eta = \eta_{min}$, and the outer wheel has a radial outer boundary at $r = r_{max}$, plus a bevel at the front at $\eta = \eta_{max}$. The boundaries are determined by the edges of the kapton electrode sheets and/or the lead absorbers.

The electrodes are subdivided along the z-axis into two compartments (inner wheel) and three compartments (outer wheel). The z locations of the divisions depend on the particular cell, and are referred to as the sampling separations.

Milled into the front wall of the cryostat is an annular depression to hold the presampler. The radial limits of this volume are called the presampler minimum and maximum radii. A conductive high voltage plane lies on top of the cavity, a short distance behind the cryostat inner wall, and a segmented readout plane is attached to the hollowed-out part of the cryostat wall.

For the simulation, two other, non-physical, reference points are important. These are the locations of fiducial planes defining the front and back boundary surfaces of a mother volume within the liquid argon, containing the electrodes plus certain cables on the front of the EMEC and at the back, between the EMEC and the HEC.

Feature	From
Front longitudinal bars back surface	Mechanics
Active volume start	printed feature on electrode
Active volume end	printed feature on electrode
Electrical focal point	printed feature on electrode
Separation point between S1, S2	printed feature on electrode
Separation point between S2, S3	printed feature on electrode
Outer wheel outer radial surface	kapton/absorber mechanics
Outer wheel outer η surface	kapton/absorber mechanics
Outer wheel inner η surface	kapton/absorber mechanics
Inner wheel outer η surface	kapton/absorber mechanics
Inner wheel inner η surface	kapton/absorber mechanics
Front cryostat wall z surface	cryostat mechanics
Presampler groove z surface	cryostat mechanics
Presampler HV z surface	presampler
Front Mother volume z surface	fiducial plane
Back Mother volume z surface	fiducial plane

TABLE VI: Reference surface definition.

In Table VI we summarize the reference points, lines, and surfaces within the EMEC.

B. Internal construction

A stable reference plane is required to define the relative position of the constituents of the EMEC. We take that plane to be the back surface of the longitudinal bars. Table VII includes the best current knowledge of the coordinate of each reference surface. Radial coordinates are measured from the axis of the calorimeter while z-coordinates are measured from the reference plane. The inner surface of the outer wheel and outer surface of the inner wheel are special because they require both an angle (the cone angle between center line and axis) and a distance (the gap distance between these two parallel surfaces).

Feature	Coordinate type	value
Front longitudinal bars back surface	z	0.0
Active volume start	z	11 mm
Active volume end	z	525(=11+514) mm
Electrical focal point	z	-3689 mm
Separation point between S1, S2	z	(Array)
Separation point between S2, S3	z	(Array)
Outer wheel outer radial surface	r	2034 mm
Outer wheel outer η surface	angle (η)	28.379^o=1.375
Outer wheel inner η surface	angle (η) + gap	9.385^o=2.5+ 1.5 mm
Inner wheel outer η surface	angle (η) + gap	9.385^o=2.5- 1.5 mm
Inner wheel inner η surface	angle (η)	4.668^o=3.2
Front cryostat wall z surface	z	
Presampler groove z surface	z	
Presampler HV z surface	z	
Front Mother volume z surface	z	-50 mm
Back Mother volume z surface	z	+580 mm

TABLE VII: Reference surface distances. These numbers are cold dimensions.

C. Geometry Description in GEANT

The endcap mother volume is a containment envelope made of air that fits closely inside the tile calorimeter extended barrel. Fig. 34 shows the mother volume, together with the tile, from several viewpoints. Inside the mother volume lie various daughter volumes, including the cylinders and cones that make up the cryostat. A complete list of objects within the mother is:

- An air volume containing minimum bias scintillators and polystyrene moderator
- A series of cylinders of aluminum and some G10 representing the cryostat walls (both inner, cold wall and outer, warm wall, and some G10 spacing between the two.

- Behind the cryostats, iron shielding, 20 cm thick between radii 47 mm and 790 mm, and 30 cm thick between an inner radius of 790 mm and an outer radius of 2520 mm
- A large LAr bath
- A second aluminum cryostat system for the FCAL
- A smaller LAr Bath within the second cryostat containing the FCAL
- A large copper plug, just behind the FCAL

A Tomographic view of the endcap can be seen in Fig. 35, and in particular the two LAr baths are clearly visible. The large LAr bath contains the EMEC and the HEC. Embedded in this bath are two smaller subsections (Fig. 36); the forward section is a bath that contains the EMEC. The HEC is discussed further in Section IX. Here, we shall further discuss the EMEC geometry and its implementation in ATLAS.

Note that the presampler does not live within the LAr bath; instead, it occupies a special place within an aluminum cryostat layer. The inner cold wall at the front face extends between radii of 221 mm and 2165 mm, and has a full thickness in z of 65 mm. Within the inner cold wall is a liquid argon volume with a thickness of 8 mm, an inner radius of 1231.74 mm and an outer radius of 171.98 mm (from $1.52 < \eta < 1.82$). The presampler is shown in Fig. 37.

In Fig. 38 we display the piece of the LAr bath containing the EMEC. This is almost a cylinder, except for the inner radius slopes as shown in Fig. 38. Within this volume is a topologically complicated set of interlocking LAr volumes, which are exploded in the view of Fig. 39.

The front support mother volume contains only inactive materials, including the LAr bath, motherboards, cables, G10, and aluminum. A view of the front and back of that volume is shown in Fig. 40.

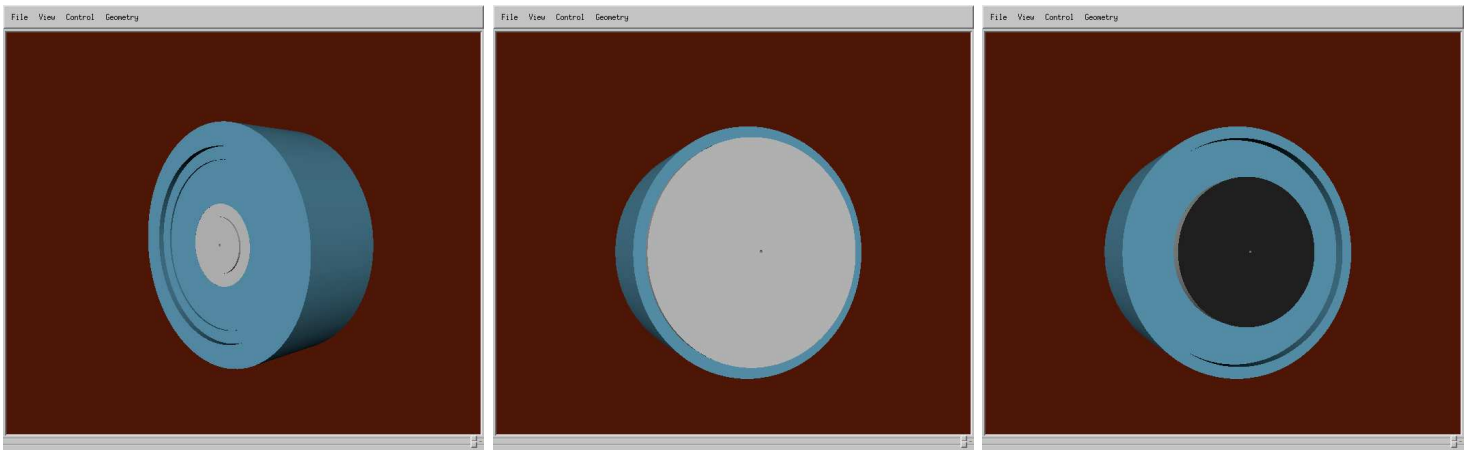

FIG. 34: *The endcap mother volume (air) fits tightly with the Tile Calorimeter extended barrel in the endcap region. Left: the front face. Middle: the back face. Right: the back face cryostats, immediately within the mother volume.*

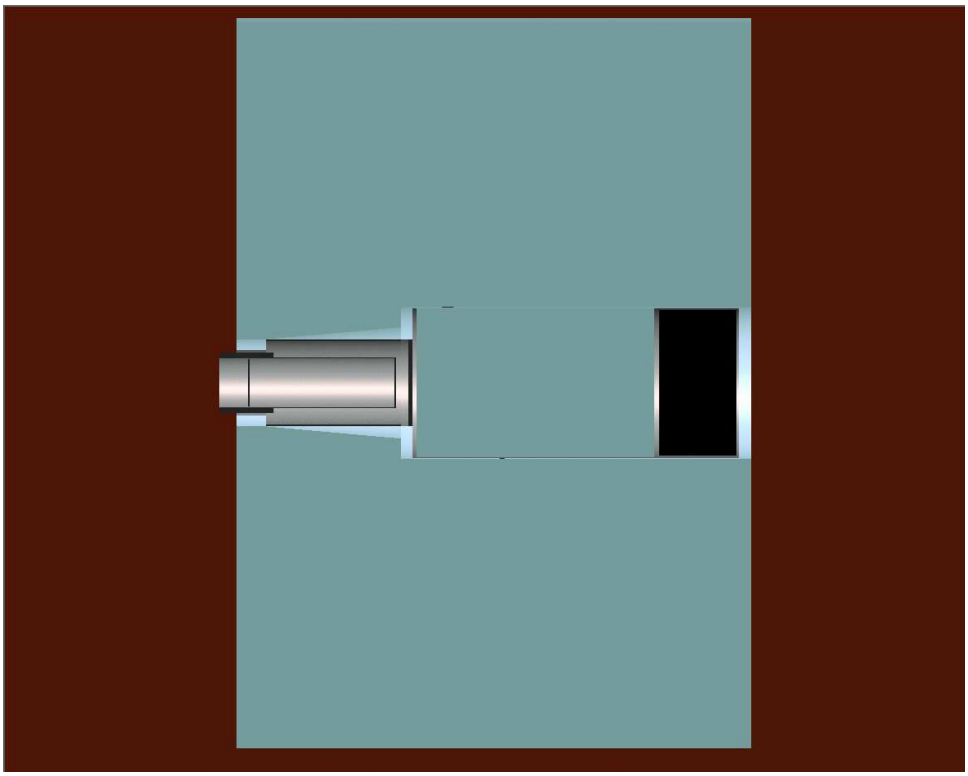

FIG. 35: *Tomographic view of the LAr Endcap Liquid Argon bath. The inner LAr bath (FCAL) is enclosed by an aluminum cylinder.*

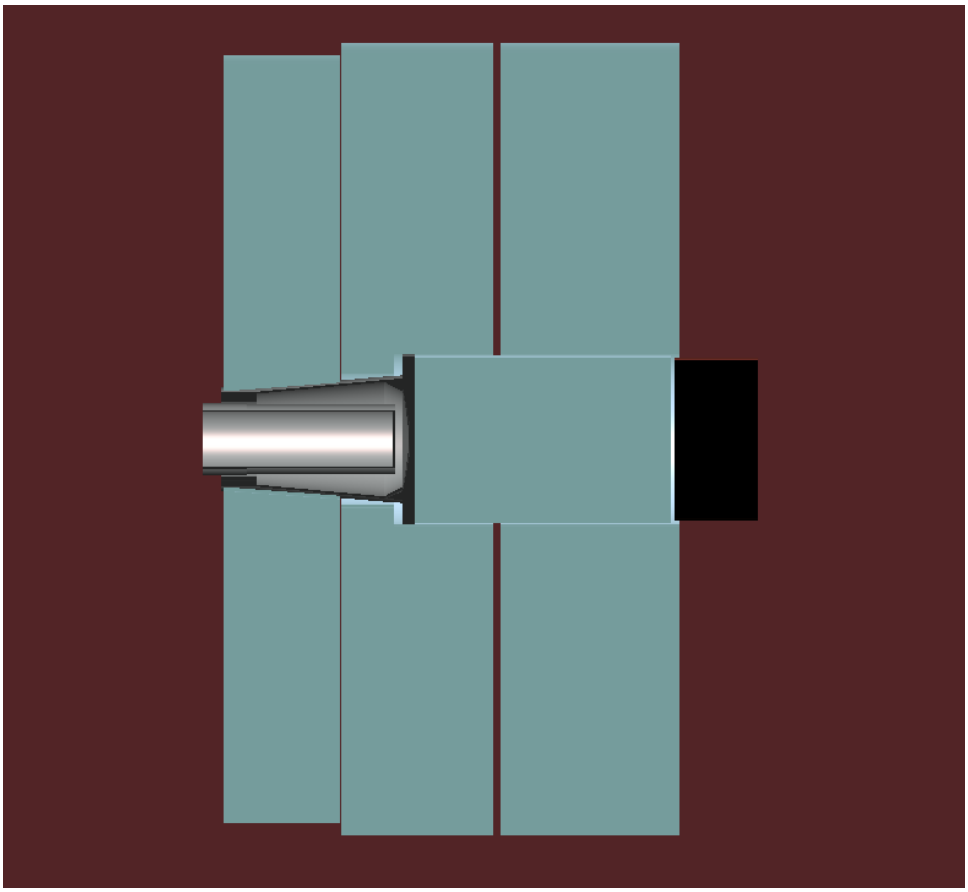

FIG. 36: *Tomographic view of the LAr Endcap Liquid Argon bath. Similar to the previous figure, but in this figure the big LAr bath has been exploded to show its contents, one bath for the EMEC and two for the HEC*

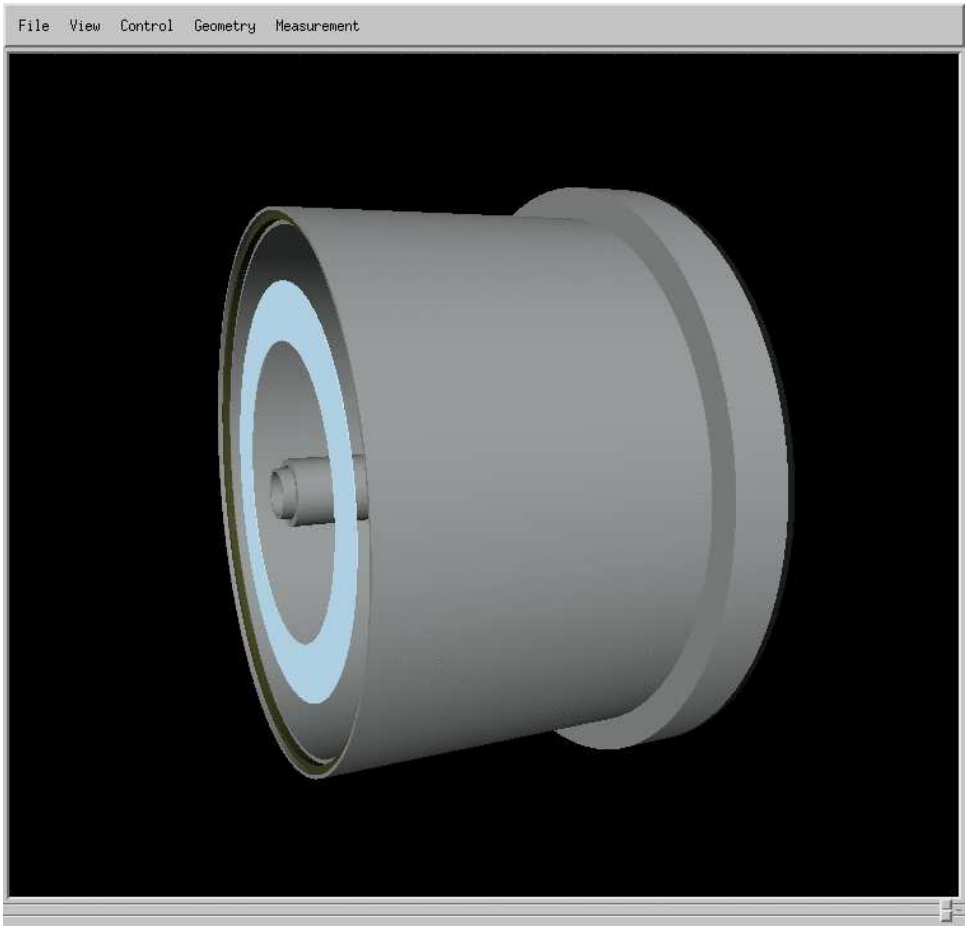

FIG. 37: *The endcap presampler LAr volume lives in within the inner cryostat aluminum front face wall.*

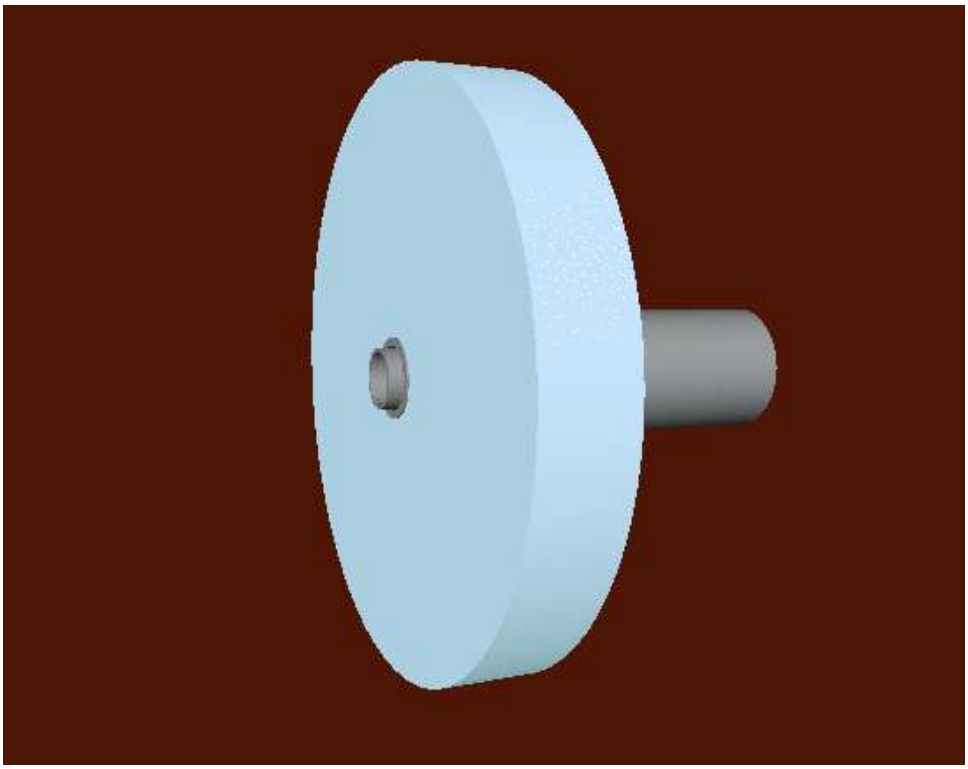

FIG. 38: *Picture of the LAr volume containing the EMEC. This volume has an outer radius of 2070 mm and an inner radius that slopes from 279 mm at z = 3639+40 mm to 324 mm at z=4269+40 mm*

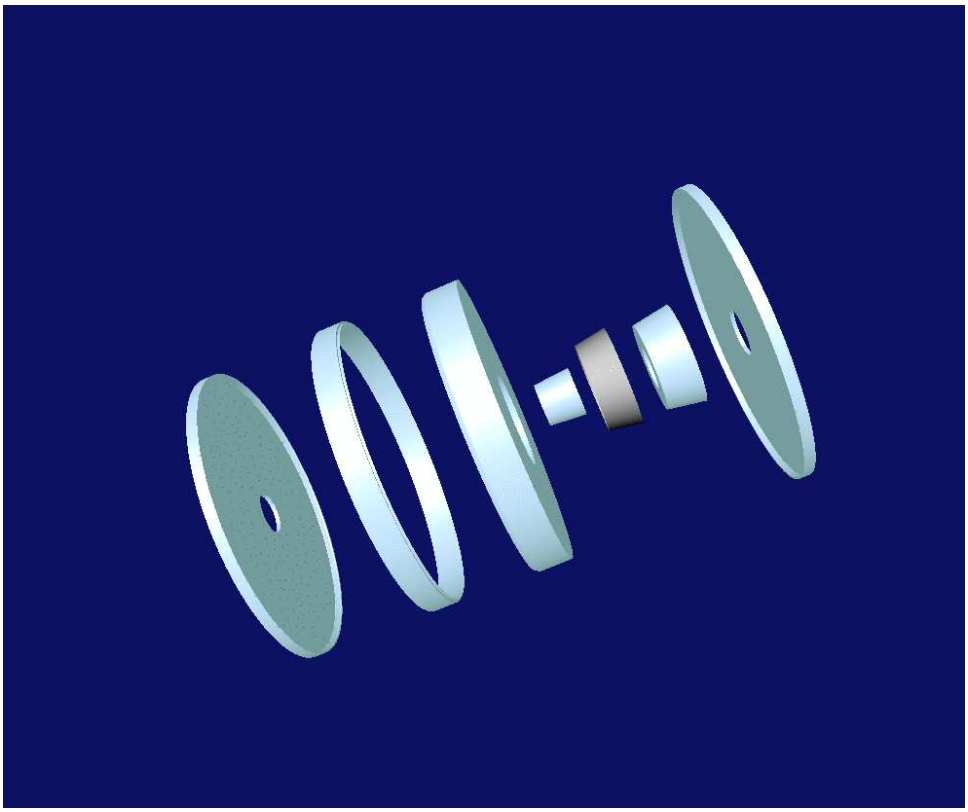

FIG. 39: *Exploded view of the EMEC LAr volume. From left to right: The front support mother, the outer support mother, the outer wheel, the inner aluminum cone (which is wrapped in a thin layer of LAr), the inner traversal bars, the inner wheel, and the back support mother.*

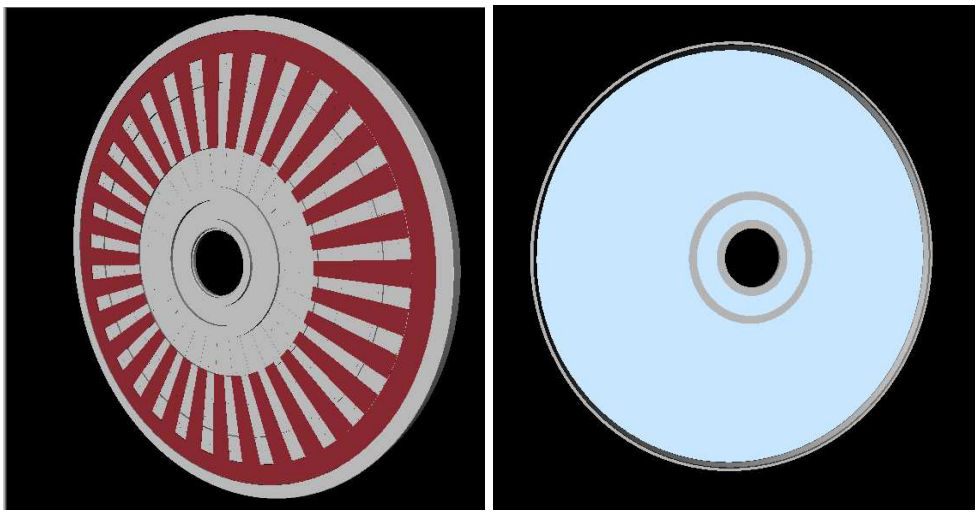

FIG. 40: *Front and back views of the dead material in the Front Support Mother volume, shown in Fig. 40*

		Dimension (mm)
Cavity	depth	5
	min radius	1210
	max radius	1725
Module	depth	9.5
	min radius	1216
	max radius	1718
Active Pads	min radius	1230
	max radius	1698

TABLE VIII: Dimensions of the endcap presampler cavity (from G. Pospelov, 15 May 2005)

D. Technical inputs to the readout geometry: Presampler

The dimensions of the endcap presampler are described in Table VIII. The external radius of the active part of the presampler is 1702 mm, the internal radius is 1232 mm and the longitudinal distance from the interaction point is 3624 mm. The presampler is placed in a special cavity on the back side of the cryostat cold wall. It's granularity is $\triangle\eta \times \triangle\varphi = 0.025 \times 2\pi/64$, i.e. the same as for the calorimeter towers in the η directions and 4 times larger in φ. This corresponds to $12 \times 64 = 768$ electronic channels for each End-Cap. The dimensions of the cells for different η are given in table IX.

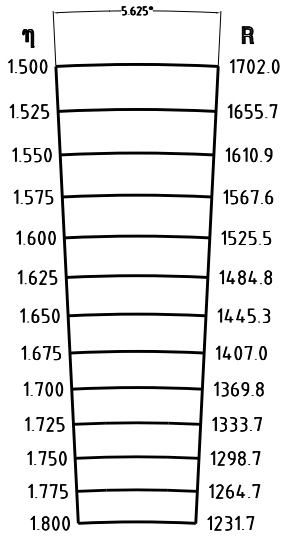

TABLE IX: Cells geometry.

η	$2\pi R/64, mm$	$\triangle R, mm$	P, cm	S, cm^2
1.500-1.525	167.1-162.6	46.3	42.2	76.2
1.525-1.550	162.6-158.2	44.8	41.0	71.8
1.550-1.575	158.2-153.9	43.4	39.9	67.7
1.575-1.600	153.9-149.8	42.0	38.8	63.8
1.600-1.625	149.8-145.8	40.7	37.7	60.2
1.625-1.650	145.8-141.9	39.5	36.7	56.8
1.650-1.675	141.9-138.1	38.3	35.7	53.6
1.675-1.700	138.1-134.5	37.2	34.7	50.7
1.700-1.725	134.5-130.9	36.1	33.8	47.9
1.725-1.750	130.9-127.5	35.0	32.9	45.2
1.750-1.775	127.5-124.2	34.0	32.0	42.8
1.775-1.800	124.2-120.9	33.0	31.1	40.4

E. Technical inputs to the readout geometry: The EMEC.

The η and ϕ boundaries of the EMEC Wheels are engineering numbers: a focal distance (also an engineering number) together with the η and cell boundary values specify the exact location of cell boundaries in the actual physical EMEC module. In a perfectly aligned EMEC the focal point would lie at the interaction point and the ϕ and η boundaries would correspond to the azimuth and pseudorapidity of particles striking the EMEC, but here we draw a clear distinction between the focal point and the interaction point in order to make a precise definition of the EMEC construction that does not depend upon a particular placement of the EMEC.

The focal distance is the distance from the reference plane to the electronic focal point. That distance is 3689.5 mm. The radial position of a point along the cell boundary (measured from the EMEC axis) can be worked out from the η value of the cell boundary, the

focal distance, z position, from the simple formula:

$$r = (f + z)/\cot\Theta = z/\sinh\eta. \quad (1)$$

In this formula, f is the focal distance and z is a z position, measured from the reference plane. For example the z position of the front of a cell can be used to determine the radial limits at the front cell boundary.

Other important numbers for the EMEC are:

- The distance between the reference plane and the start of the active region: 11 mm.
- The overall active depth: 514 mm.

These numbers are in the `EMECMagicNumbers` table of the DD Database.

The sensitive volumes in the endcap are called LAr::EMEC::OuterWheel and LAr::EMEC::InnerWheel. A recent addition to the simulation is the simulation of some reduced sensitivity in the barrette region, shown in Fig. 33, between the reference plane and the active region, formerly considered to be a completely inactive part of the detector.

Access to the readout geometry is provided through the `EMECDetectorManager` and related classes. In particular the position of the focal points, their distance to the reference plane, and the other numbers discussed above can be retrieved from the `EMECDetectorManager`. The absolute transform of the `EMECDetectorRegions`, (polycones with local z=0 at the front surface) can be obtained as well as the characteristics of any cell. An image of the EMEC with readout geometry overlaid is shown in Fig. 41.

F. Technical inputs to the readout geometry: The EMEC inner wheel

The inner wheel of the EMEC covers the pseudorapidity interval $2.5 < \eta < 3.2$. It is divided into only two longitudinal samplings. By convention these are called sampling layers 1 and 2 (there is no presampler coverage in this region and no coverage from sampling layer 3). A separation occurs between the two sampling layer at a particular depth in the inner wheel that varies with η index. (Presently these are available in the database table EmecSamplingSep, columns ZIw[0-6]).

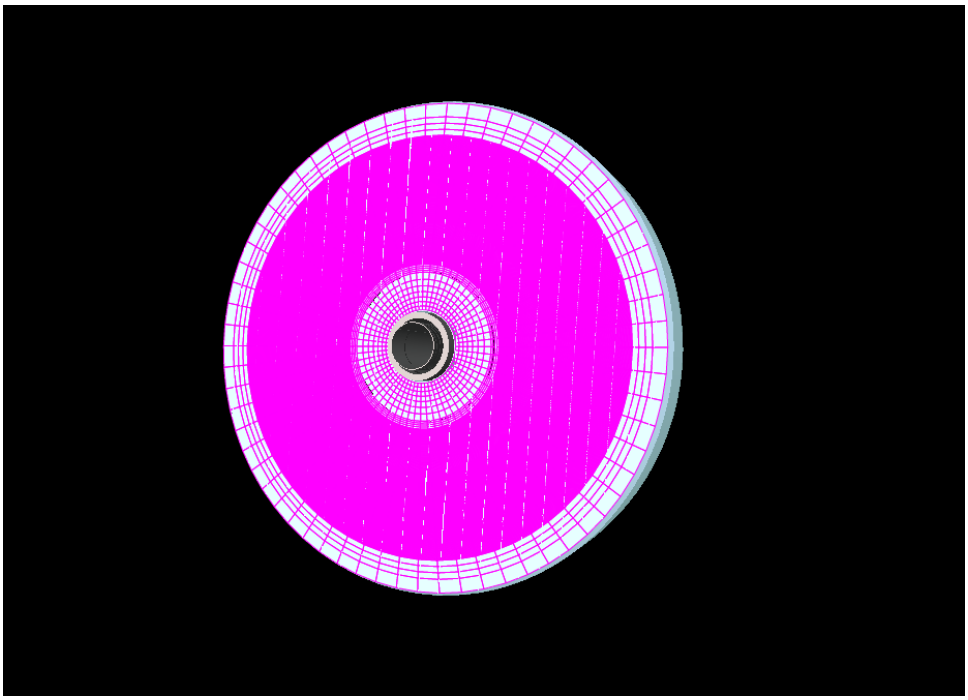

FIG. 41: *A view of the EMEC with the readout cells (sampling layer 1) superimposed. For the first layer the strips, which have a very fine granularity in η, are too small to be resolved in this view.*

G. Technical inputs to the materials

In the Tables X and XI we give a summary of the characteristics of the different materials used in the description of the EMEC. The most sensitive part for the response of the calorimeter is what deals with the absorbers characteristics. However, most complexity is found in the description of the front and back support structures. Although there might be significant improvements in the description of the materials composing these support structures this only plays in at next to leading order. These materials come from the detector description database are introduced to the simulation through the `StoredMaterialManager`; in addition, some materials (such as absorber) are pre-blended in the `LArMaterialManager`. The material used to describe "G10" in many support structures is actually a mixture of G10 with glass fibers, so a "custom" G10 (called G10Bar) is actually used where appropriate.

Material mixtures, like absorbers for example, are defined at cold by applying a cold contraction factor of 3×10^{-3}. A corresponding change is also applied to the widths of the

Material	$X_0(mm)$	Density (g/cm^3)	Location
Liquid Argon	142.24	1.40	EMEC mother Cryostat
Aluminum	89.87	2.70	Support
Iron	17.97	7.87	Absorbers
Copper	14.69	8.96	Support Electrodes
Lead	5.56	11.3	Absorbers
Air (20 C, 1 atm)	$304 \cdot 10^{-3}$	$1.214 \cdot 10^{-3}$	Experimental hall
Glue ($C_5H_8O_4Si = C_5H_8O_2 + SiO_2$)	203.77	1.69	Absorbers Barrettes
G10	224.41	1.80	Support

TABLE X: Description of the materials in use in the EMEC simulation (Dec. 2008)

absorbers. The contraction significantly changes the total number of radiation lengths seen from the absorbers, by about 0.1 X_0.

We note the following simplification in the material description: the absorbers and barrettes are in fact held by sheets of stainless steel instead of the raw iron that is currently used in the description. This stainless steel is composed of 71.75 % of iron, 19 % of Chromium and 9.25 % of Nickel. The density is of 7.84 g/cm^3 and the radiation length is of 18.14 mm. Nevertheless, the resulting effect on the total radiation length of the absorbers can be neglected.

H. Modeling the accordion folds in the endcap: the custom solid

1. Prehistory

Since EMEC absorbers and electrodes have a complicated fan-like shape it is necessary to use a special approach to describe their geometry. This appears to be the only case in all of ATLAS simulation where a shape is defined using the GEANT4's flexibility in defining

Material	$X_0(mm)$	Density (g/cm^3)	Location
Inner wheel barrette Glue (0.30 mm) + Iron (0.40 mm) + G10 (1.70 mm)	86.86	2.64	Support
Outer wheel barrette Glue (0.30 mm) + Iron (0.40 mm) + G10 (2.20 mm)	77.02	2.82	Support
Thin absorber Glue (0.30 mm) + Iron (0.40 mm) + Lead (1.70 mm)	7.29	9.58	Outer wheel
Thick absorber Glue (0.30 mm) + Iron (0.40 mm) + Lead (2.20 mm)	6.92	9.88	Inner wheel
Kapton	279.89	1.46	Electrodes Support
Electrodes 62% Kapton + 38% Copper (in mass)	35.45	4.32	Electrodes “Barrette” connectors
G10Bar=G10 + Glass Fiber G10 (38%) + SiO_2 (62%)	181.04	1.72	Support
Cables Copper (62%) Kapton (38%)	58.4	3.04	Cables

TABLE XI: Description of the materials in use in the EMEC simulation (Dec. 2008)

"custom" solids. Before GEANT4 was used in ATLAS, a GEANT3 version of simulation existed in which each absorber and electrode was described as a set of mini-pieces of standard shapes. In 2001, it was decided rely upon a custom shape for the GEANT4 version of the simulation. The main reasons for this decision were:

1. absence of "twisted trapezoid" shape in GEANT4 (at that time),

2. non-ideal stacking of "elementary pieces" in GEANT3.

The custom shape represents a whole wheel (inner or outer) of absorbers or electrodes.

2. Geometry of absorbers and electrodes

The geometry of endcap absorbers and electrodes differ only in their thickness, so a common term **"fan"** is used for both "absorber" and "electrode".

All geometrical calculations in custom solid are based on the computation of the distance to a so-called **neutral fiber**. The neutral fiber is a wave-like surface in the middle of the fan's thickness. Its properties are described below.

The amplitude of a fan's waves increases with distance from the wheel axis. Therefore, the wave slant angle α has a complex dependency on the radius.

Fig. 42 represents the cross-section of the neutral fiber in the plane parallel to the plane OZX and displaced from the calorimeter axis at a distance y. 1/4 of a neutral fiber's wave is shown. It consists of a straight region, where $x = z \tan \alpha(y)$, and a fold region. The fold radius ρ is constant for a given fan type.

The geometry of first and last quarter-waves of a fan is a little different (Fig. 43). It has an additional fold region of the same radius ρ. The flat part of the quarter-wave is directed to a point s which is a constant distance from the edge, so the straight region (of length $s - l$) at the beginning of the wave varies with y. The value of l is given by $\rho \tan \beta$, where $\beta = \alpha/2$.

A practical realization of a model of the geometry is based on the tables from [15], which contains tables of the neutral fiber dimensions. Using these tables, the dependence of the slant angle α on the distance to the calorimeter axis is parameterized with a 4th-degree polynomial.

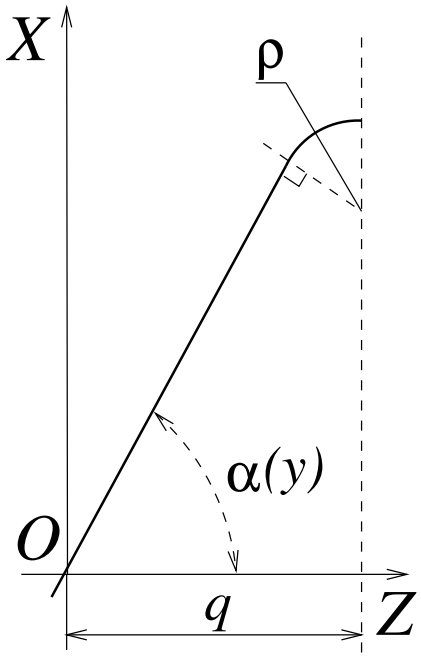

FIG. 42: 1/4 of wave of the fan's neutral fiber. O – local origin of coordinates, q – length of 1/4 of the fan's wave.

Real absorbers and electrodes have a structure of several layers, with each layer made of different material. In the custom solid approach the multilayer structure is replaced with a single-layer one using a "mean" material, similar to the approach used for the EMB.

3. Details of the implementation

Geometry engine is divided into three main parts. Corresponding classes are:

1. `LArWheelCalculator` holds the geometry core — initialization of constants and calculations of various distances to the neutral fiber.

   Its main methods allow to get for each point given in local coordinate system (which has $z = 0$ at wheel's front face):

   (a) The LAr φ gap number in which the point is located and the closest side of the nearest fan,

   (b) shortest distance to the nearest fan's neutral fiber,

   (c) nearest point on the neutral fiber,

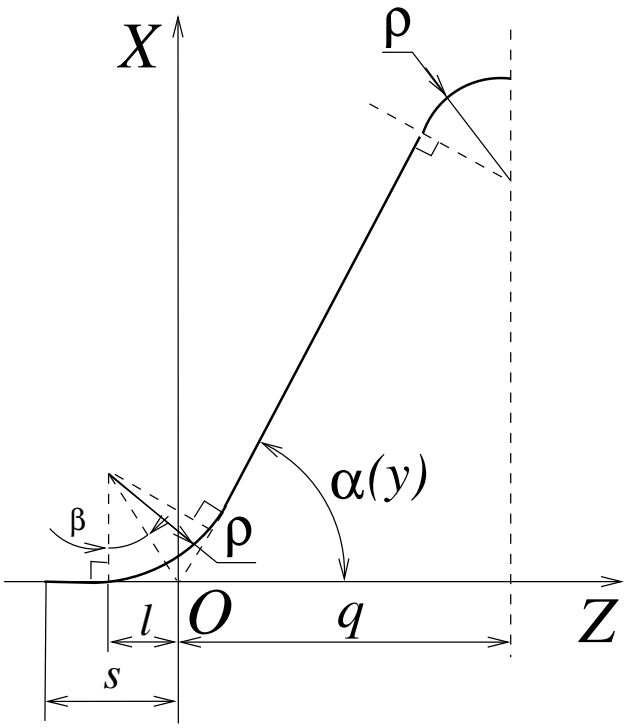

FIG. 43: 1/4 of the first wave of the fan's neutral fiber. O – local origin of coordinates, q – length of 1/4 of the fan's wave.

(d) amplitudes of the neutral fiber and both fan's surfaces as a function of the point's z coordinate.

There are also service methods to get various parameters of geometry (like fan thickness, limits on η etc).

For the calculations, all the input parameters are translated to the coordinate system where the fan is positioned along the OY axis (so-called **"vertical"** fan). If necessary, after the calculation the results are translated back into the initial coordinate system.

The current implementation assumes the absorber and electrode are used in conjunction. That means user can not set up geometry without, for instance, electrodes. Some algorithms require an electrode between each two absorbers and vice versa. This technique improves performance.

2. `LArWheelSolid` is GEANT4 custom solid. Thus it is inherited from the base class `G4VSolid` and a number of methods is implemented in it:

(a) `Inside(`$\vec{p}$`)` — determines if the point p is inside of solid, on its surface, or outside. The method gets the distance to the nearest-to-p fan and compares it with half of fan's thickness.

(b) `DistanceToIn(`$\vec{p}$`), DistanceToOut(`$\vec{p}$`)` — determines the shortest distance from the point p located outside or inside of the solid (respectively) to the solid's surface. The "distance to in" is the distance to the nearest-to-p fan's neutral fiber minus half of fan's thickness. Inverting this quantity gives the "distance to out".

(c) `SurfaceNormal(`$\vec{p}$`)` — determines a vector normal to the solid surface and going through the point p. It finds the nearest point on the closest fan's neutral fiber and returns the unit vector pointing to p from that point.

(d) `DistanceToIn`$(\vec{p},\vec{v})$, `DistanceToOut`$(\vec{p},\vec{v})$ — compute the distance from the point p located outside or inside of the solid (respectively) to the solid surface along the arbitrary vector $\vec{v}$.

(e) Several special functions for tracking and solid drawing.

A special feature of `LArWheelSolid` is its data member called `BoundingPolycone`. It is a polyconical shape that limits a wheel. It allows to reduce amount of calculations if the point is completely outside of a wheel.

An important feature of custom GEANT4 solids is the following: the information given by the functions mentioned above must be self-consistent. For example, if `DistanceToIn`$(\vec{p},\vec{v})$ returns value d then `Inside(`$\vec{p}+d|\vec{v}|$`)` must not return "outside".

3. `LArWheelEnergyCalculator` produces EMEC hits. It is a descendant of `LArWheelCalculator`. Apart from energy corrections, it features some geometrical methods to find hit positions which are not appropriate for the parent class.

For test-beam simulations it is necessary to be able to describe geometry of a single EMEC module (i. e. 1/8 of the whole wheel). This option is implemented.

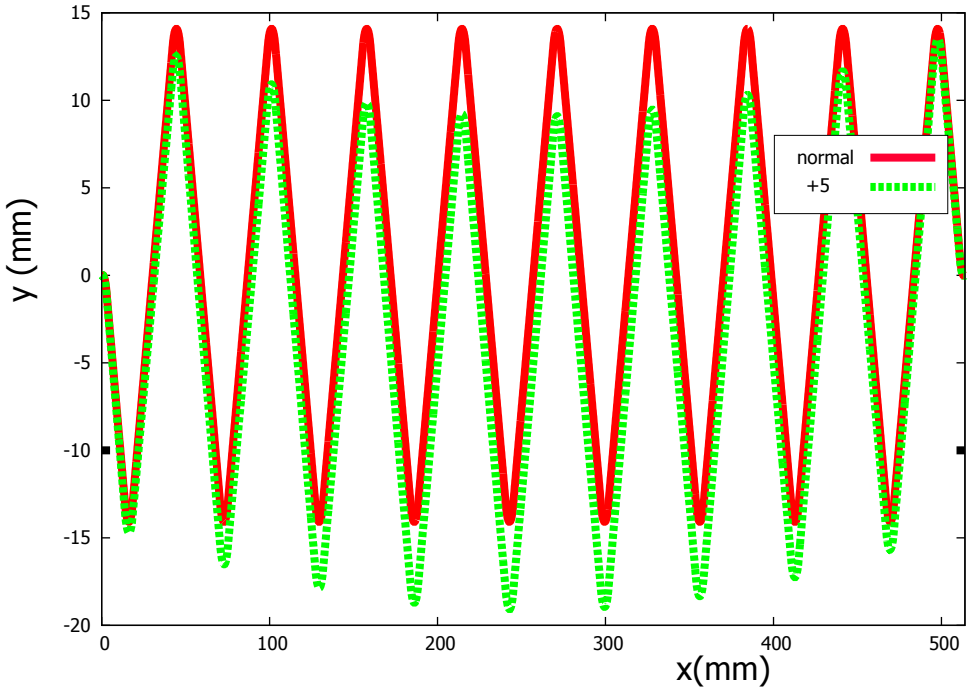

FIG. 44: Cross section of neutral fiber at $R = 1200$ mm. Normal fan and sagged fan with maximal sagging of 5 mm (measured values have amplitudes less than about 1.5 mm

4. Sagging deformation

Sagging of the absorbers under the action of gravity is implemented. It uses the following model.

In the coordinate system of the vertical fan each point is displaced on x coordinate according to the formula

$$\Delta x = A(y, n_f) \times \left(1 - \left(\frac{2z}{w}\right)^2\right),$$

where $A(y, n_f)$ — sagging amplitude as a function of y and fan number n_f, w — wheel thickness in z direction. So it is parabolic vs z, which is close to cosine if A is not too big.

VIII. RESPONSE AND CHARGE COLLECTION EFFECTS IN THE ELECTROMAGNETIC BARREL

5. Generalities

For each GEANT4 step, the appropriate signal derived from the ionization energy loss should be computed and recorded in the appropriate readout cell. This involves two kinds of computations: a) the identification of the readout cell and b) the simulation of the energy to current conversion. Part a) relies on the geometry of the detector. All the relevant computations are done in the internal frame where the calorimeter (or the presampler) is projective, so none of the computations have to be changed in case of misalignment. Part b) aims at computing the measured current after the front-end electronics for a given true deposited energy, taking into account electric field variations and the finite integration time of the readout electronics.

6. Cell identifier computation for the calorimeter

The sensitive LAr volume is defined as the LAr inside the STAC volume (cf. Figure16) in which the electrodes and absorber accordions are located. In addition, the radius of the hit should be smaller than 1960 mm to account for the fact that the end of the electrode in this area is not sensitive. The local z position in the half-barrel frame should also be greater than 4 mm (beginning of the HV area on the electrodes).

For a GEANT step in this fiducial volume, the cell number is computed as follows:

- The sampling number (strip, middle or back) is computed from the radius of the hit in the half-barrel frame (see Figure 45). A 1.1 mm thick transition region between the strips and the middle is considered as inactive. The small readout striplines of the middle section going across the back compartment to the signal connectors are taken into account (this is somewhat simplified because in this case the energy deposit is assigned to the readout stripline directly affected and not the back cell facing it). This line structure is quite complicated at the high η part of the barrel, and it is somewhat simplified in the simulation, see Figure 46.

- In ϕ, the cell number is computed from the accordion structure, and in case of non-ideal geometry, the actual positions of the absorbers and electrodes volumes in GEANT4 are used
- In η, the geometry is supposed to be perfectly projective

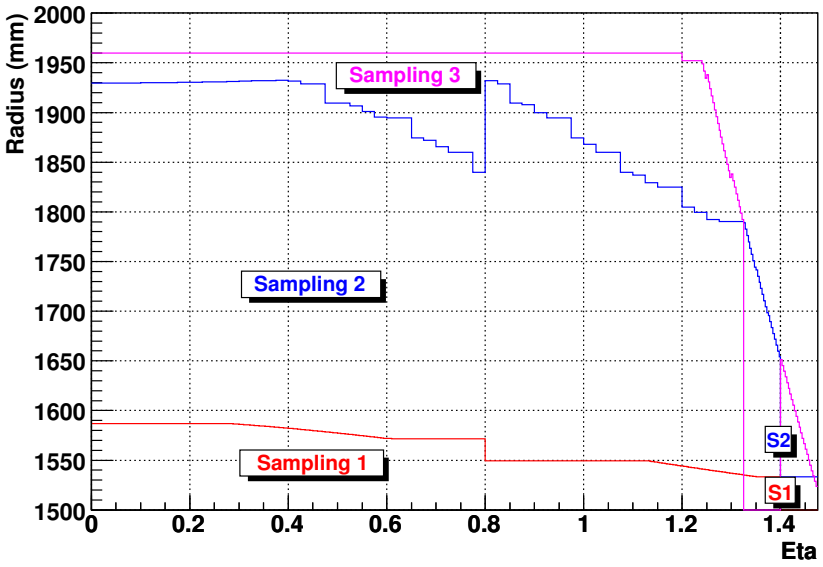

FIG. 45: *Transition between the samplings of the calorimeter. Sampling 1 has granularity 0.025/8 in η and $\pi/32$ in ϕ. Sampling 2 has granularity 0.025 in η and $\pi/128$ in ϕ. Sampling 3 has granularity 0.050 in η and $\pi/128$ in ϕ. Note that the layout has changed since the calorimeter TDR. At η=0, the separation strip-middle is set at r=1586.995 mm and the separation middle-back at r=1929.577 mm*

7. *Current maps for the calorimeter*

The current induced by a drifting charge q in Liquid Argon is given by

$$i = qv_d \cdot E/V \tag{2}$$

where E is the electric field vector, V the high voltage applied and v_d the drift velocity. If E is the total electric field, then i is the total current induced on all cells. If E is the

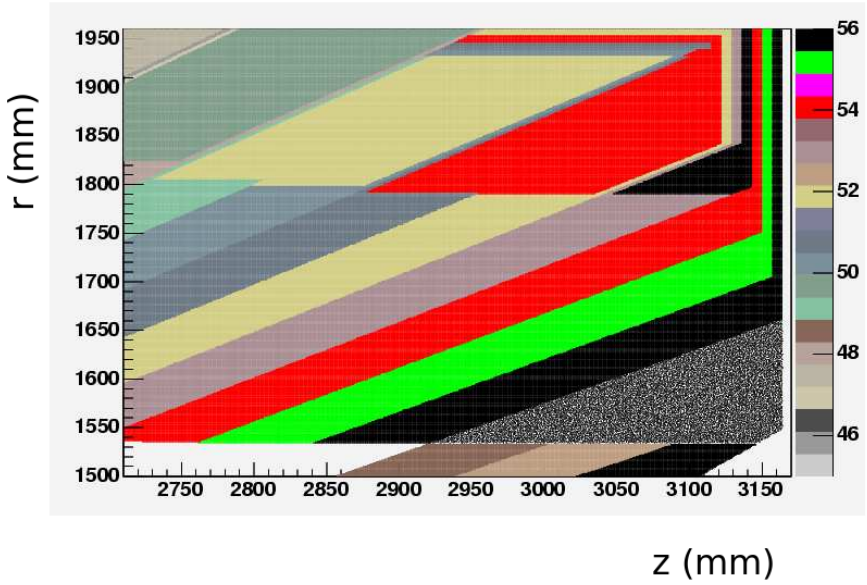

FIG. 46: *Detail of the cell granularity in the r-z plane showing how the small readout striplines of the middle cells are described.*

electric field when only one electrode is at the high voltage and the other electrodes at the ground, then i is the current induced on this electrode only. This is useful to compute current sharing among neighbor electrodes.

To avoid full 3D computations of field maps, the problem is divided into two parts, using the approximate symmetries of the calorimeter:

- In the x-y plane, to account for the accordion folds where the electric field is varying significantly. Depending on the radius, the position in the calorimeter is either considered as being in a fold or in a straight part. In the former case, electric field maps have been computed numerically for each fold separately by G.Lemeur and F.Touze at Orsay. In the later case, the field is almost constant except for the small widening of the gap along the electrode axis, and the field is approximated as V/gap.

- In the z-d_{elec} plane, to compute energy sharing among neighbor electrodes and also to account for the electrode transition region around η=0.8. In the later case a separation of $\pm$3 mm is assumed between the HV active part of the two electrodes.

From the electric field maps, current maps are computed. At a given position, the charge

created by a 1 MeV energy loss is computed. A ionization energy of 23.3 eV is used and an effective recombination effect as a function of the electric field is also taken into account (see Figure 47). The drift velocity and the current are then computed. The drift velocity used is taken from the note LArg-99-08. The temperature of LAr is assumed to be 89 K in this computation, which only affects the overall normalization. This charge is then moved in steps of 1 ns, computing each time the new position and the new current, until the charge reaches the electrode, in order to compute a current induced on the electrode as a function of the time. Figure 48 shows the ionization current as a function of time for a uniform energy deposition inside a middle cell at η=0.225.

This current is then convolved with the electronic response to a delta impulse (provided by M. Delmastro from electronic calibration data analysis). Different responses are used for different regions:

- Strips for η <0.8, covering folds 0,1,2 and straight sections 0,1,2
- Strips for η >0.8 and η <1.4 covering folds 0,1 and straight sections 0,1
- Middle for η <0.8, covering folds 3 to 12 and straight sections 2 to 12
- Middle for η >0.8 and η <1.4 , covering folds 2 to 12 and straight sections 1 to 12
- Back for cell number 0 to 8 and 26, covering folds 9 to 13 and straight sections 8 to 13
- Back for cell number 9 to 12 and 16 to 18, covering folds 12 to 13 and straight sections 11 to 13
- Back for cell number 13 to 15 and 19 to 20, covering folds 10 to 13 and straight sections 9 to 13
- Back for cell number 21 and 25, covering folds 9 to 13 and straight sections 8 to 13
- Sampling 1 for η >1.4, covering folds 0,1 and straight sections 0,1
- Sampling 2 for η >1.4, covering folds 2,3,4 and straight sections 1 to 4

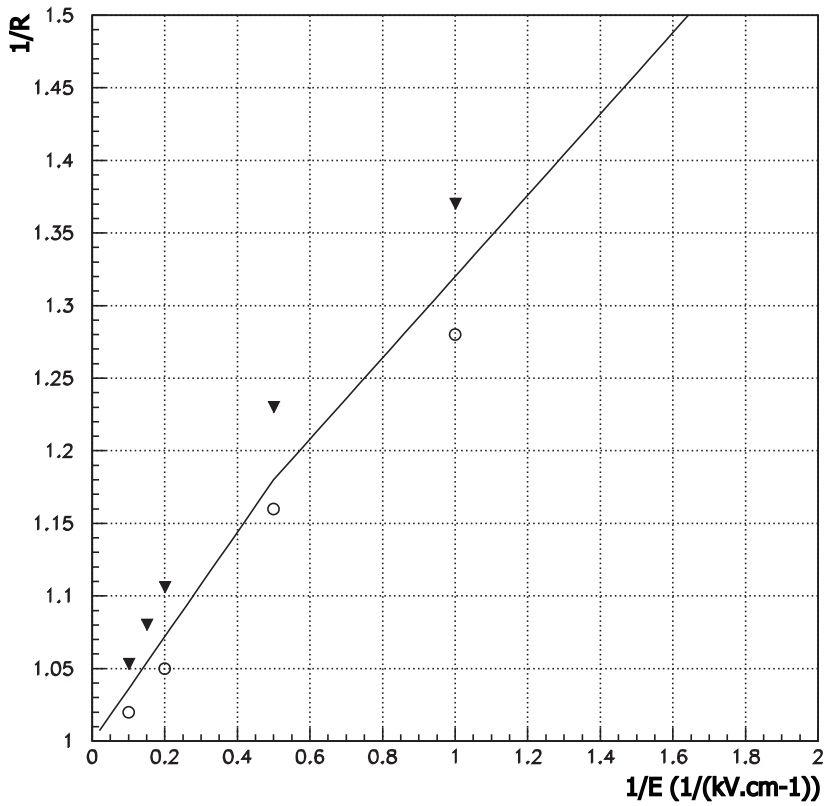

FIG. 47: *Inverse of recombination effect as a function of inverse electric field. The line is the value used in the current map computation. The symbols correspond to values found in the literature (black points are data from Scalettar et al, Phys.Rev.A25(1982)2419, white points are data from Aprile et al, NIMA261(1987)519. Note that the nominal inverse electric field in the straight sections is 0.1*

This leads to a total of 47 maps to cover all the folds. For the straight sections, all the even ones are the same and all the odd ones are the same (but odd and even are slightly different because the average gap is slightly different); thus for the ten regions, 2 x 10 maps are needed.

Figure 49 shows the current after shaping as a function of time, for uniform energy deposit inside a middle cell. The predictions are compared to electron data from the 2002 test-beam provided by L.Serin.

From the current after shaping, the final response is computed applying Optimal Filtering

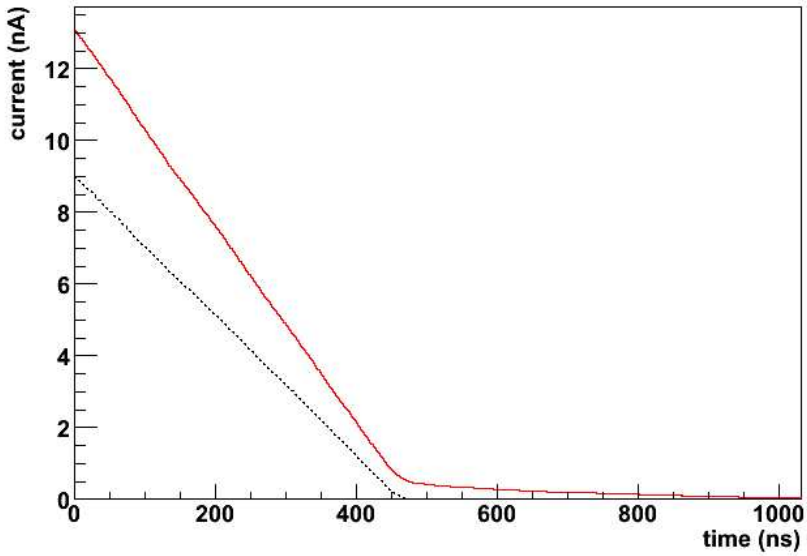

FIG. 48: *Ionization current as a function of time for a uniform energy deposition inside a middle cell at η=0.225. The dashed line shows the contribution from the straight sections of the accordion only.*

Coefficients[16] (OFC) to the the 5 samples centered around the maximum. The OFC are computed assuming a triangular average signal for the drift time corresponding to the average gap in the straight section (low luminosity conditions are assumed for the noise auto-correlation function used in the OFC computation). Taking into account the convolution with the shaper response allows one to take into account the reduction of the response for charge deposited near the electrode, where the drifting time is smaller than the shaper integration time.

The response is then normalized to the average value in the straight section for 2000 V (14.16 nA/MeV), so that the value stored is effective energy in MeV, such that this average effective energy is equal to the ionization energy in the straight sections.

Figure 50 shows some example of current maps in the x-y plane.

The maps hold the response at 400, 1000 and 2000 V applied high voltage, where it is assumed that the OFC are re-computed with the proper drift time.

As an overall check of the variations of recombination and drift velocity with high-voltage, Figure 51 shows the response vs applied HV (normalized to 2000 V) from the field map

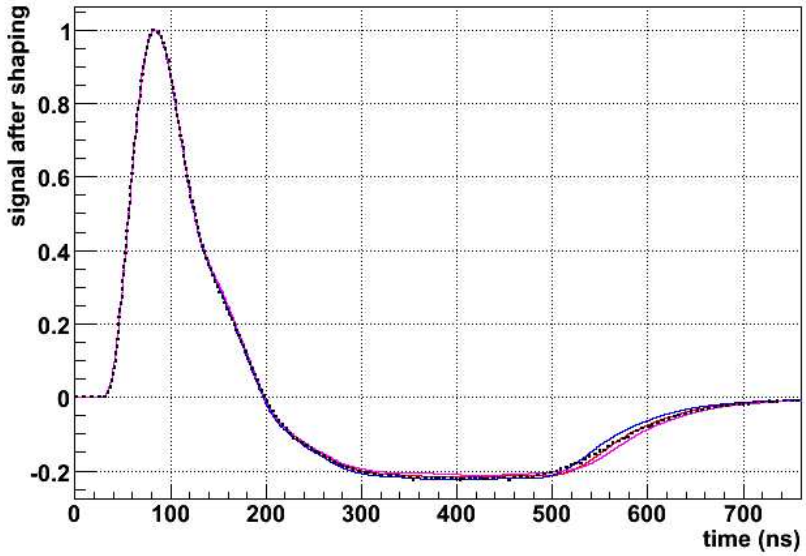

FIG. 49: *Current after shaping as a function of time for a uniform energy deposition inside a middle cell at η=0.225. The black dashed points are electron data from 2002 test-beam. The solid lines correspond to predictions for LAr temperature of 87.3, 89.2 and 90.8 K.*

computation, compared to test-beam data from 2002 and 2004. Between 100 V and 2000 V, the agreement is at the level of 1-2%.

A given step from GEANT in the LAr is divided in sub-steps of 200μm each (assuming that the energy loss is equally spread among the various substeps). For each sub-step, the local position in the electrode frame in the x-y plane is computed. The proper field map is used depending on the fold or straight location and on the cell number. The overall response read from this field map is then spread among cells η-1, η and η+1 using dedicated maps in the plane (z-distance from electrode) to include effect of energy sharing across cells, and for η close to 0.8 by a map taking into account the gap in electric field between the two electrodes.

In case of sagging, the same maps are used starting from the real local positions in the (sagged) electrode frame (with the adequate protections to avoid going outside the map which is defined for the ideal geometry). The overall response is scaled further by the ratio between the actual gap at the location of the step and the gap in the ideal geometry to the power 1.3 to account in first order for the change in the gap gain induced by the sagging. As

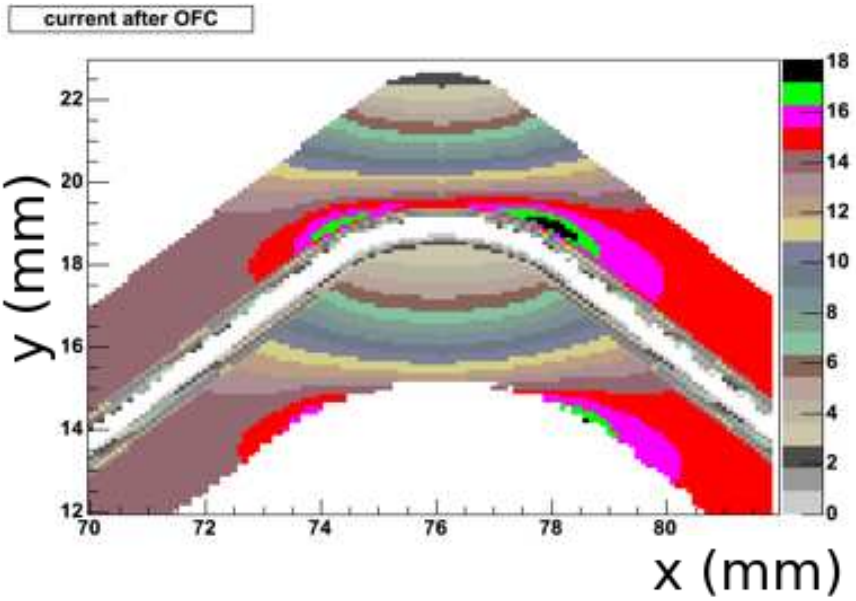

FIG. 50: *Current Map in one of the fold sections in the middle, for 2000 V applied high voltage.*

the change in the gap size is rather small, this first order approximation should hold well.

8. Cell identifier computation for the presampler

The cell number in ϕ is computed from projective geometry ($\Delta\phi$=$2\pi/64$). The cell number in η is computed from the z position in the half-presampler barrel frame, taking into account that cells in the same module have the same size in z, and this size is different from module to module. The tilt of the electrodes is taken into account in the first two modules.

9. Current maps for the presampler

The depth of the liquid argon in the presampler is 13 mm. The active HV on the electrode only covers 11 mm radially. To take this effect into account, current maps in the r-z planes are used. The same procedure as for the calorimeter is used, starting from electric field maps and deriving from them current maps. This is done separately for each presampler nodule, to take into account the differences in the electrode tilt and in the gap. The normalization is

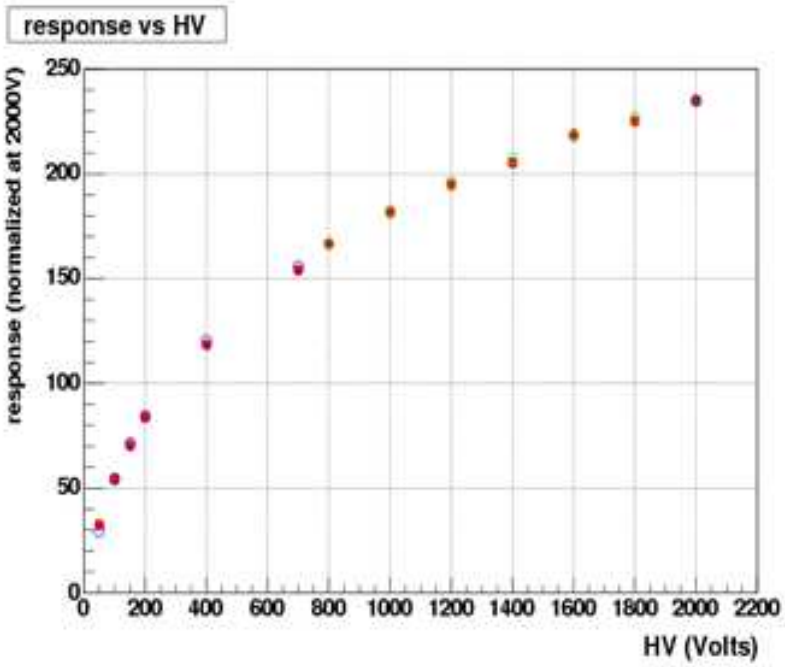

FIG. 51: *Response as a function of high voltage from this computation (red points) compared to test-beam data from 2002 (green points) and 2004 (blue points). Note that for this comparison, the simulation uses the same pulse reconstruction as 2002 and 2004 (parabola in one case, cubic in the other case) and not the OFC reconstruction*

given by the nA/MeV at the middle of the presampler, averaged over the various modules. Thus the simulation takes into account the gap variation between modules in the i/E factor. The electric field maps were computed by G.Lemeur. An example of current map for the presampler is shown in Figure 52. The average effect is that the effective collected energy is typically 10% smaller than the total ionization energy deposited in the LAr layer.

Small cracks in ϕ between presampler cells (especially between sectors) are ignored in the simulation.

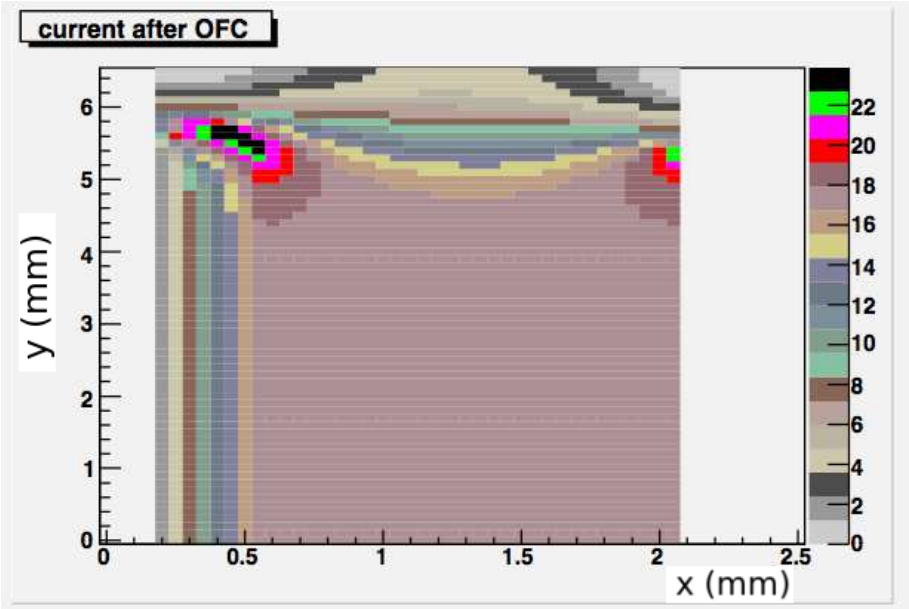

FIG. 52: *Current Map for the third presampler module. The x-axis is the distance from the middle of the electrode, the y-axis is the radial thickness inside the presampler (0 is the middle of the presampler layer). The nA/MeV values are shown as color code.*

IX. THE HADRONIC ENDCAP CALORIMETER

The hadronic endcap calorimeter (HEC) is a copper-LAr calorimeter providing hadronic calorimetry in the region $1.55 < \eta < 3.2$. It is built in two "wheels" (HEC-1 and HEC-2) and lies just behind the EMEC. A drawing of the HEC's position within ATLAS is shown in Fig. 53. A picture of an actual HEC-1 is shown in Fig. 54.

The two HEC volumes within each endcap are separately alignable within the ATLAS detector, and the readout geometry description (accessible through `HECDetectorManager`) is tied to the alignment of the two wheels. These wheels consist of 32 modules, which are ϕ-slices. Each module is built as a stack, with copper plates alternating with thin layers of liquid argon. The copper plates are 2.5 cm thick in HEC-1 and 5 cm thick in HEC-2 module, the front plate of each stack having half the nominal thickness, and the liquid argon layers have a thickness of 8.5 mm. Electrode planes run parallel to the copper, through the middle of each liquid argon layer. Stainless steel tie rods 6 mm and 8 mm in radius (for the front and rear wheels respectively), also modeled in the simulation, hold the entire assembly together. To hold the plates apart stainless steel spacers are added to the rods effectively increasing their radius to 8.5 mm (front) and 11.5 mm (rear) in the 8.5 mm liquid argon layers.

The layers of the HEC are conceptually grouped into seven "Longitudinal Blocks", which are collections of neighboring plates with identical radial segmentation. A map of these blocks can be seen in Fig. 55. The readout cells are semi-projective; within a block they are non-projective, but across blocks they form staircases that follow nominal pseudorapidity lines converging at the HEC focal points. The readout segmentation follows these staircases. The first sampling layer of the HEC consists of the first longitudinal block; and the second, third and fourth samplings consist of longitudinal blocks (2-3), (4-5), and (6-7) respectively. In the detector description database, the information on the construction of the blocks and the radial readout segmentation resides in the `HECLongitudinalBlock` table, and is also available through the `HECDetectorManager`. The `HECDetectorManager` also provides access to the focal distance of the HEC-1 and HEC-2; these are the distances between the focal points of the HEC wheels and their reference planes. Those reference planes are the front faces of the HEC wheels. They are modeled, within the ATLAS simulation, as

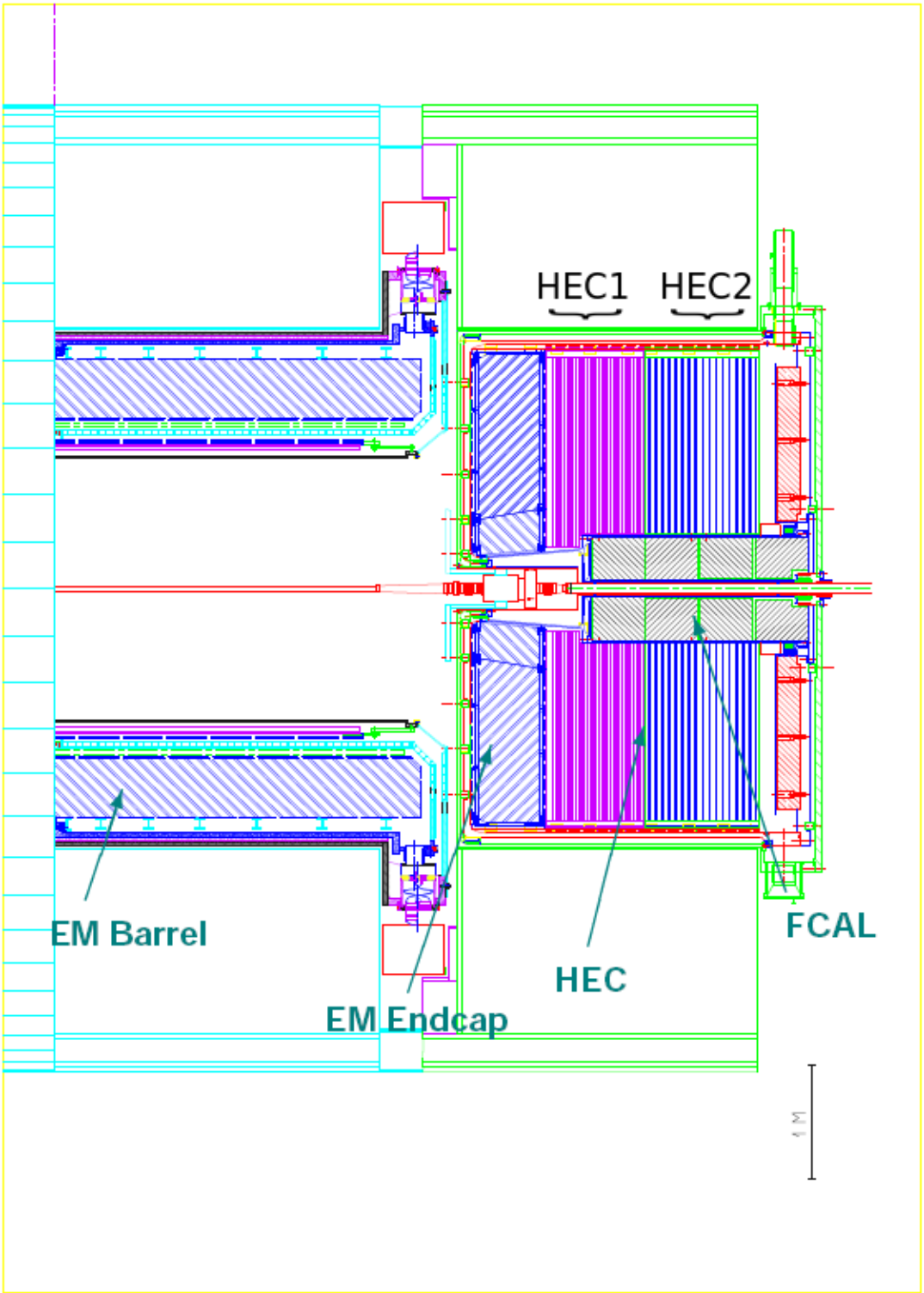

FIG. 53: Display of the two HEC wheels in ATLAS.

polycones; the position of the $z = 0$ plane of these polycones is at the front surface.

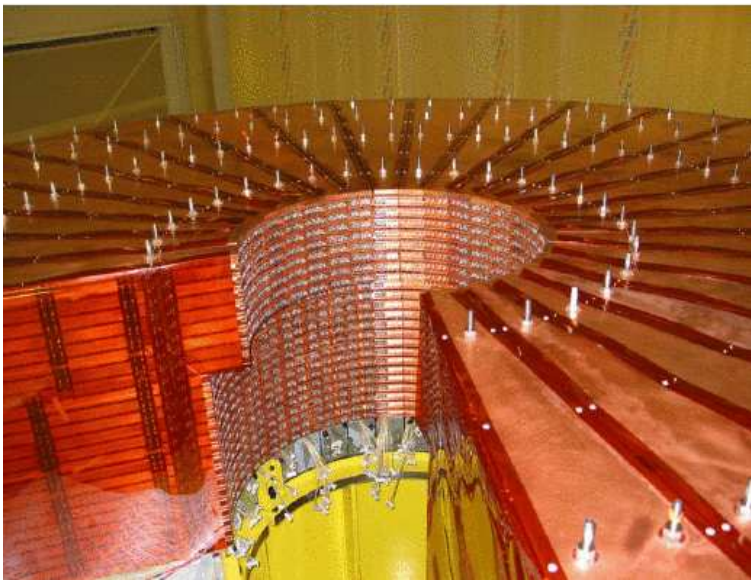

FIG. 54: An Overview photograph of the HEC.

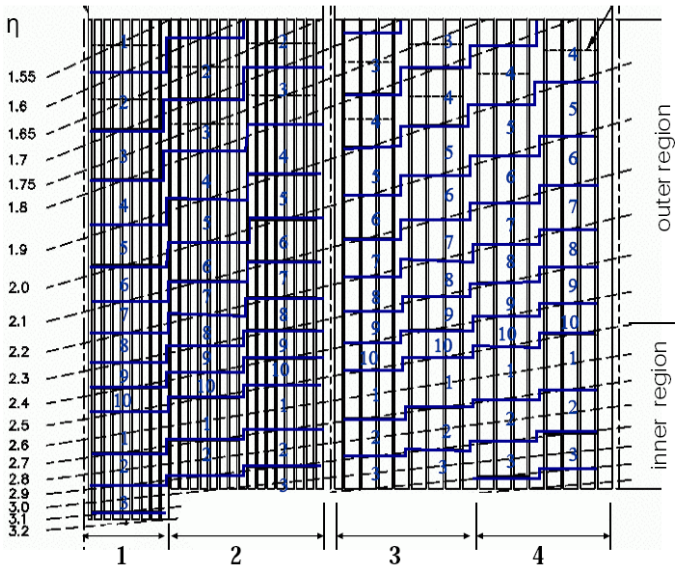

FIG. 55: Longitudinal Segmentation of the HEC

As everywhere in the LAr systems, the readout segmentation changes as a function of eta. This is implemented using regions of constant granularity. The entire η range of the HEC is covered by two regions ("inner" and "outer"). The readout segmentation for the first layer of the HEC are shown in Fig 56. Nominal cell boundaries for all layers can be found in the `HECNominals` table of the detector description database. Descriptors for the regions can also be retrieved through the `HECDetectorManager`.

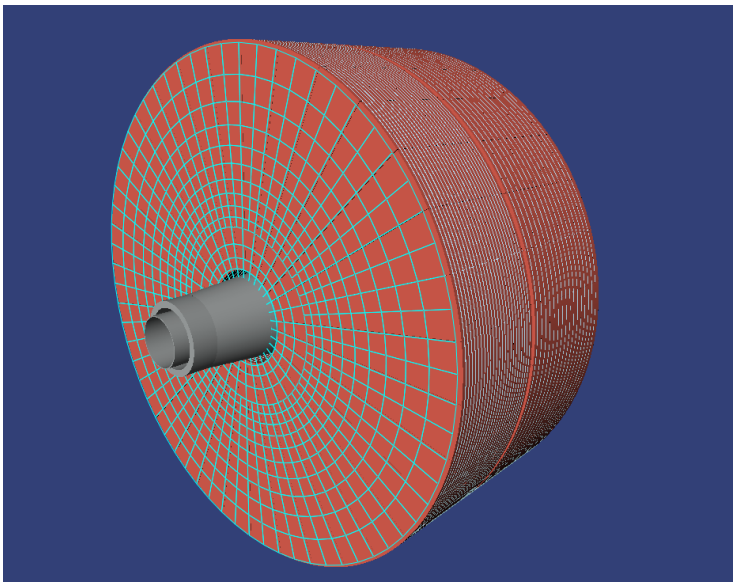

FIG. 56: Segmentation of the HEC

Along the ϕ-edge of each module runs a 2 mm wide inter-module gap filled with only liquid argon. Additionally, beyond that gap and into the copper, there is another 3 mm dead region. The inter-module gaps are modeled in GEANT, and the additional dead zone is achieved by embedding a liquid argon sensitive region inside a liquid argon fiducial region. Within the liquid argon fiducial region we place three electrodes, a PAD electrode in the center of the gap and one EST electrode in front of, and behind the PAD electrode. The electrodes are separated by honeycomb structures and liquid argon. Details of the gap region are shown in Fig. 57.

The HEC is a homogeneous detector and any mechanical tolerances are well below any significance for physics. This holds also for expected features of the cabling, such as timing and impedance matches, and also for calibration. The implementation of the HEC within the ATLAS simulation follows these principles, recommended by the HEC group:

- The average outer cold boundaries of the detector are carefully reproduced
- Average cold densities are used, so as to describe the total material present accurately
- Significant areas where the detector has inactive regions are modeled (for instance around the spacers and in the intermodule gaps)
- The ability to test failure modes is maintained. This implies the ability to switch off

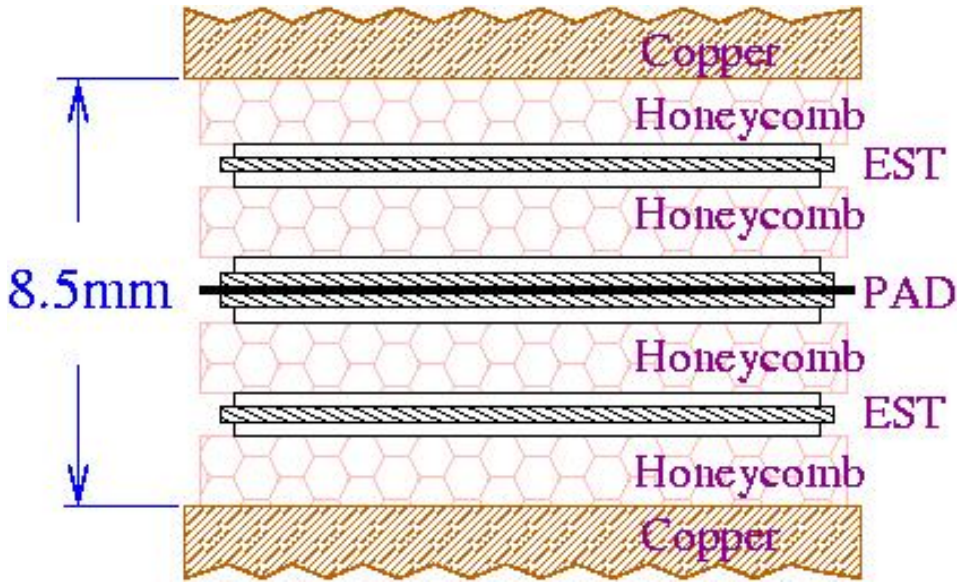

FIG. 57: Details of the HEC readout gap.

a sub-gap. There are 4 sub-gaps per 8.5 mm argon gap.

In the following discussion we will describe effects which are affecting the simulation. To these effects we ascribe a complexity level to classify their size. The basic description is assigned complexity 0; corrections affecting the average signal at approximately the 1% level complexity 1, and 0.1% is assigned complexity 2.

A. Details of the HEC Simulation

In view of the very close thermal expansion coefficients of copper and 316 stainless steel (16.7 and 16.0 ppm/degC at room temperature), the thermal expansion coefficient of copper should be used for all elements, including the readout boards (which are dominated in their thermal behavior by the copper pads etched in them. Using the LAr temperature of 89^o gives a scale factor of .99702 for linear dimensions; $1.0899 = (0.99702)^{-3}$ for densities. The cold contraction parameter is recorded in the detector description database (`ColdContraction` table). Densities of several important materials used within the description of the HEC are recorded in Table XII. HEC copper in both wheels extends to an outer radius of 2130 mm; contraction reduces this to 2023. As one can see from Figs. 54 and 55, the first longitudinal block, coinciding with the first sampling layer has a slightly different inner radius 372 mm

TABLE XII: Densities(COLD) of materials used in the HEC

Material	Density g/cm^3
Copper	9.01
Argon	1.396
Kapton/Glue in PAD and EST boards	1.45

(371 mm at cold) than the other layers 475 mm, (473 mm at cold).

In addition, the copper plates and the kapton/argon/honeycomb structures in the four readout gaps are described (in an average manner). The fractional volume of liquid argon displaced by the honeycomb is taken as 3.1%. The mechanical structure is assumed to shrink as if it was completely made of copper rather than copper and stainless steel. The assumed linear shrinkage warm to cold is described by a factor of 0.99702. This shrinkage is assumed for all HEC components (such as PAD boards). Thicknesses of the main components after contraction are tabulated in Table XIII. The simulation reads its high voltage status from a database and applies them to the response within each of the four sub-gaps individually (since hardware failures may occur at the sub-gap level). The ability to test the failure of a single sub-gap in a readout volume of 32 (or 64) sub-gaps is maintained. These effects constitute a complete, basic description (complexity 0). The hits written by the HEC simulation (when HV is present) contain the GEANT 4 energy deposits, without any charge collection effects.

The volume of the tie rods and spacers, the connecting bar material, are not only dead areas for readout but also areas of decreased interaction lengths. This affects the simulation at complexity 1.

The HEC modules are held in place at the inner radius by "tie bars" and at the outer radius by "connectors"; these are shown in Fig. 58. At its inner radius, approximately 2 cm of material has been milled away to accommodate bolts, reducing the material there at the few percent level. The connectors at the exterior of the HEC mostly affect the tile calorimeter. This is assigned complexity 2.

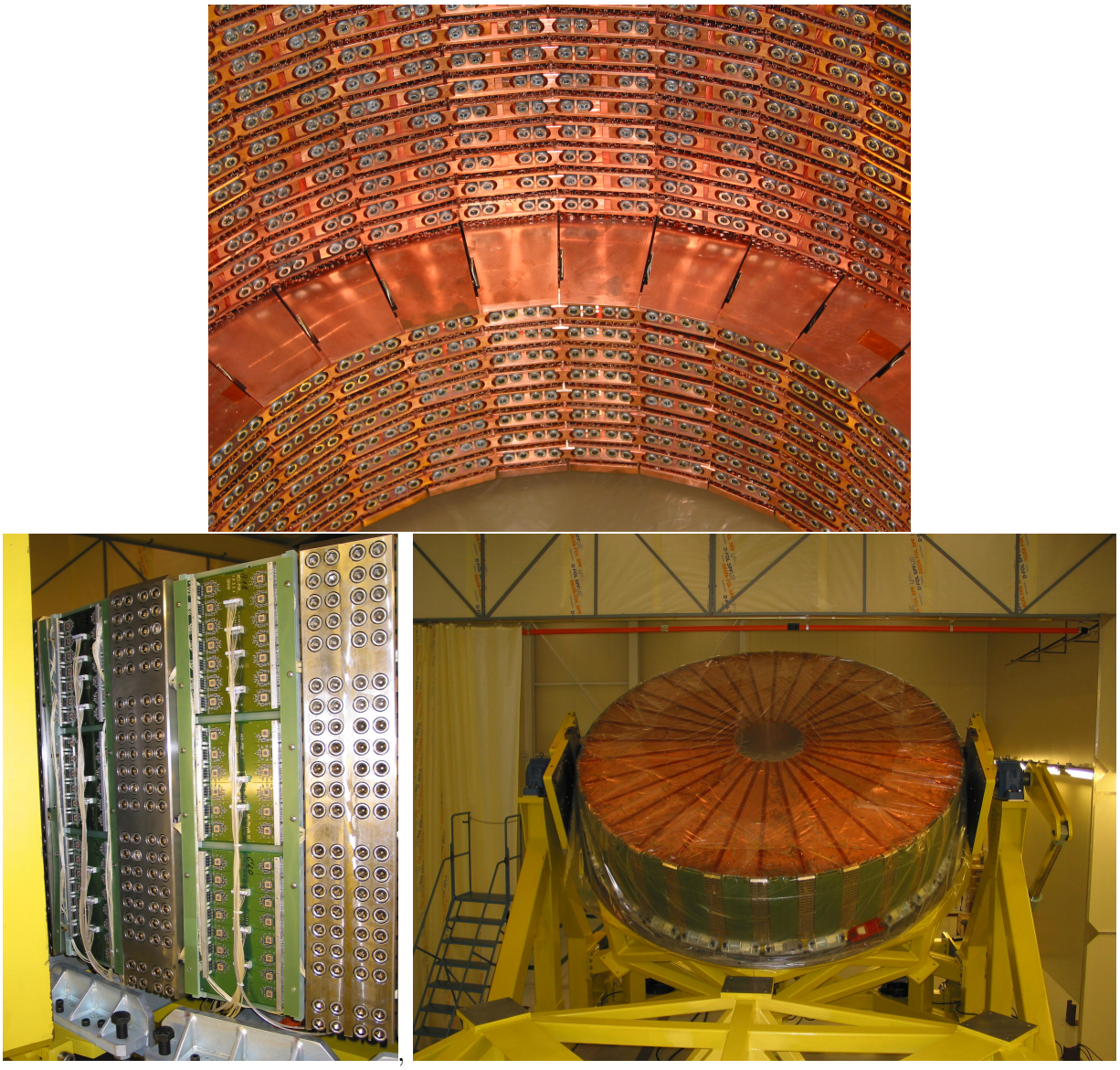

FIG. 58: Images of the tie rods at the inner radius of the HEC and connectors at the outer radius of the HEC.

B. Production Variations

Details of the production variations in HEC modules are held in two databases[18, 19]. An in-depth analysis of the impact of these effects upon the signal is presented in Ref [17]. Variation in the calorimeter response should be compared with the energy resolution of the HEC, $75\%/\sqrt{(E)}$ which at 1000 GeV gives 2.4%. Variations of copper plate thickness, copper-to-copper gap thickness, fraction of the liquid displaced by the honeycomb, PAD

TABLE XIII: Thicknesses(COLD) of HEC components (mm):

Component	Thickness (mm)
Copper(nominal)	12.463, 24.925, 49.851
Copper(actual)	12.464, 24.935, 49.852
PAD (incl copper)	0.380
EST	0.151
Cu-Cu Gap(nominal)	8.475 (front) ; 8.475 (rear)
Cu-Cu Gap(actual)	8.490 (front) ; 8.463 (rear)

and EST board thickness, thickness between the four sub-gaps affect both the sampling fraction and the pulse shape. This results in a signal variation which has been evaluated in [17] and which is summarized in Table XIV. All effects are at or below the 0.3% level. The magnitude of the signal variation due to production variations affecting the sampling fraction and signal in the HEC, is well below the expected resolution of the hadronic endcap calorimeter even for the highest energy jets. They are not expected to affect the linearity. We make no geometrical corrections based on observed variations in the production data.

TABLE XIV: Signal variation due to production variation of quantities that affect the sampling fraction and the signal shape. This information is from Table 15 in Ref. [17].

Variation	Gaps 1-8	Gaps 9-24	Gaps 25-32	Gaps 33-40
Copper thickness	0.03%	0.04%	0.03%	0.03%
Displacement of argon volume by honeycomb.	0.21%	0.21%	0.21%	0.21%
Gap thickness, including PAD, EST board thickness	0.18%	0.18%	0.22%	0.22%
Sub-gap thickness (all HV on)	0.00%	0.00%	0.00%	0.00%
Sub-gap thickness (3/4 HV on)	0.20%	0.14%	0.20%	0.20%
Total (all HV on)	0.26%	0.25%	0.26%	0.26%
Total (3/4 HV on)	0.32%	0.29%	0.32%	0.32%

X. THE FORWARD CALORIMETER

A. Generalities

The FCAL or forward calorimeter lies in the region $3.1 < |\eta| < 4.9$, inside a dedicated aluminum support tube that forms a mechanical part of the endcap cryostat. In the ATLAS simulation the walls of this support tube are "assembled" within the same mother volume, the endcap cryostat mother, as the cryostat containing the EMEC and HEC.

The FCAL consists of three individual modules: the front module (FCal1) is a copper-LAr module designed for EM calorimetry while the following two (FCal2 and FCal3) are constructed mainly of tungsten and are referred to as Hadronic Forward Calorimeter modules.

Besides the absorbers and the active liquid argon volumes, a few other dead (or inactive) volumes in the FCAL region are worthy of mention. Cable harnesses (modeled as a material mixture) run in grooves along the sides of the modules. A moderator tube known as the "JM Tube", composed of boronated polyethylene, with a density of 0.99 g/cm^3, lies in front of the FCal1 face, along a cylinder concentric with the beam pipe. These volumes are illustrated in Fig. 59.

The structure of the forward calorimeter modules is described in detail in [20]. Briefly, each module consists of a disk of absorber material containing a large number of cylindrical holes parallel to the beam line into which tubular electrodes are inserted. Each electrode consists of a copper tube into which has been inserted an absorber rod made of copper in the case of the FCal1 and of tungsten in the case of the FCal2/3 modules. This rod has a diameter slightly smaller than the inner diameter of the copper tube and is positioned concentrically inside the tube using a helical wound radiation-hard plastic fiber (PEEK), which also serves to electrically isolate the rod, which forms the anode of the LAr cell. The active gap is then a narrow annular layer of LAr.

The FCAL1 module is constructed from a stack of copper plates, each drilled with 12,260 holes for the electrodes. Copper tubes are inserted into each hole to provide a smooth surface for the LAr cell. Copper rods are used in the electrodes.

For the hadronic modules, which use tungsten as the primary absorber material, such a construction technique was not possible. Instead the FCal2/3 modules rely on a copper

skeleton: copper tubes are inserted between two endplates drilled with the required number of electrode holes. The spaces in between the tubes are filled with tungsten slugs which are manufactured to have the appropriate cross-sectional shape, and a length of about 1 cm. The modules are assembled by first "stacking" the absorber matrix defined by the copper endplates, the copper tubes, and the tungsten slugs. There are, additionally, specially manufactured copper pieces that run between the endplates at the inner and outer radii. At small radius this is a single piece and provides mechanical support at the inner edge of the modules. At the outer radius there are a series of shell pieces which do not provide much mechanical support. These are largely cosmetic, but do offer some protection to the outermost layer of electrodes during the modules assembly. These pieces are referred to as the inner and outer absorbers, respectively.

The modeling of hadronic and electromagnetic modules is done in slightly different ways, as illustrated in Fig. 60. For the electromagnetic modules, first, the absorber "matrix" is modeled as a material mixture. Then tubes of liquid argon are inserted into this matrix. The electrode holes in the copper plates that are stacked to form the FCal1 matrix are slightly larger that the outer diameter of the copper tubes that are inserted into them. These interstitial regions will fill with liquid argon when the cryostat is filled. For this reason, the FCal matrix is modeled as a mixture of copper and liquid argon, with mass fractions of 98.9% and 1.1%, respectively. For the hadronic modules, cylinders of liquid argon are inserted into the matrix and the electrode rods are inserted into the LAr cylinders, leaving the annular LAr gap. For the hadronic modules, the material mixture represented by the matrix is, additionally, more complicated.

The hadronic absorber "matrix" is effectively a mixture of the copper endplates, the copper tubes, the tungsten slugs and the (inactive) LAr that fills any residual volume between the electrodes and slugs. The slugs are themselves a mixture of tungsten, iron and nickel (WFeNi) as will be described in more detail below. The electrode rods are essentially pure tungsten. The details of the mixture calculation are provided in section X B.

For each module, the positions of the electrodes are recorded in a database structure called `LArFCALElectrodes`, which is filled with the list of electrode positions used in the manufacture of the FCAL (*i.e.* in the drilling of the copper plates).

In FCAL1, the gap has an inner radius of 2.356 mm and an outer radius of 2.625, for

a total gap of 269 μm. In FCAL2, the inner gap radius is 2.465 mm; the outer radius is slightly different for the two modules due to different shipments of copper tubes. The values are discussed below. For the simulation we take an average, corresponding to an outer gap radius of 2.841 mm or a gap of 376 μm. In FCAL3, the inner radius is 2.748 mm, and the gap is 508μm. The LAr Gaps can be seen in Fig. 60. More detailed information about the electrode parameters can be found the in reference [20].

The readout geometry of the FCAL differs from that of other ATLAS calorimeters in that it is laid out in a rectangular pattern, rather than following lines of constant η and ϕ, as shown in Fig. 61. The readout unit in the FCAL is called a Tile. Conceptually the readout cells are approximately rectangular prisms lying within the FCAL module, but actually they are simply a ganging of electrodes. Tiles in FCAL1 are (mostly) constructed from groups of 16 electrodes; in FCAL2 groups of 24 are used, and in FCAL3 groups of 36 are used. In each module, smaller tiles are used around the inner and outer edges. Both the tubes and Tiles are placed in a semi-regular plan in order to cover as much surface as possible. There is no recipe or simple prescription for generating the tile positions (or the tube positions for that matter); they are however accessible through the `FCALDetectorManager` and the classes that it manages. These include `FCALModule`, which contains the position of the FCAL in ATLAS coordinates, and also the `FCAL_ChannelMap` which contains many details about the tube positioning. The `FCALModule` also provides details of the nominal tile boundaries.

The simulation of the FCAL is a fairly simple affair. No charge collection effects are applied. Raw Geant energies are summed up within each cell and written out as `LArHit`s.

This remainder of this section summarizes those parameters of the hadronic forward calorimeter (modules 2 and 3) that are necessary for the detector description in the Monte Carlo simulation. The main issue is the effective density of the absorber matrix since this is described in the Monte Carlo as a mixture of copper (from the tubes) WFeNi (from the tungsten slugs) and liquid argon, which fills the volume not occupied by these other materials.

B. The Hadronic FCal Matrix Density

Each hadronic forward calorimeter (FCal) module consists of an hexagonally arranged

array of tubular electrodes, each formed by a copper tube and a rod of almost pure tungsten which is inserted into the electrode tube and positioned concentrically by a helically wound PEEK fiber. The gap formed by the rod and tube combination forms the active volume of the detector when filled with liquid argon. The absorber is composed of the tungsten rods and the matrix into which they are inserted. A partial view of the face of a hadronic forward calorimeter module is illustrated in Fig. 62.

The spaces between the electrodes are filled with tungsten alloy (WFeNi) slugs, as shown in Figs. 62 and 63. The slugs are produced by sintering a mixture (by weight) of 97% tungsten powder, 2% nickel and 1% iron, with the iron and nickel acting as binding materials. The powdered material is mixed with an organic binder and pressed into "greenform" slugs, which are approximately 20% larger than the specified dimensions of the final parts. The slugs are then sintered, that is, fired above the melting points of the binding materials. The nominal density (reported by the manufacturer) is 18.5 g/cm^3, though QC measurements put the value at about 18.3 g/cm^3. The slug cross-sectional area is defined by two quantities: the length d of the equilateral triangle that contains it and r, the radius of the curved section. d_{max}, the maximum value of d, is given by the electrode spacing, which is 8.179 mm in FCal2 and 9.000 mm in FCal3. Note that the radius feature is always defined with respect to the corner of an equilateral triangle with side d_{max}. The nominal slug size is shown as the darker line. The tolerance window is defined by ± 0.1 mm at 90° to the slug surface.

Setting $T = d_{max}$ and $r = r_{min}$, the maximal cross-sectional area is given by

$$A_{max} = \frac{1}{2}T^2 \sin(60^\circ) - \frac{1}{2}\pi r^2$$

and the minimal cross-sectional area is given by the expression

$$A_{min} = \frac{1}{2}T^2 \sin(60^\circ) - \frac{1}{2}\pi (r+t)^2 - 3(T - 2r - 2t)t$$

where $t = 0.2$ mm is the full size of the tolerance band (± 0.1 mm). The range of acceptable cross-sectional areas is given in Table XV. Assuming a slug material density of 18.3 g/cm^3, these can be converted into a mass/unit length, as also shown in the table.

The volume fractions of the components of the absorber matrix are calculated in the following manner. Fig. 63 represents one "unit cell" of the detector matrix, containing a single row of slugs and one half of an electrode. The cross-sectional area of this unit cell is given by

Module	A_{min}	$(M/\ell)_{min}$	A_{nom}	$(M/\ell)_{nom}$	A_{max}	$(M/\ell)_{max}$
FCal2	11.00	0.201	12.44	0.228	13.97	0.256
FCal3	12.61	0.231	14.18	0.259	15.83	0.290

TABLE XV: Calculated slug properties for FCal2 and FCal 3. There are three areas A represent the maximum, nominal and minimal cross-sectional areas (in mm^2) of the slugs, calculated from the slug specifications (i.e. the envelope in Fig. 63). The corresponding values for the mass/unit length (in mm) are also shown in each case, assuming a slug density of 18.3 g/cm^3.

FCal Module	Tube O.D.	Tube I.D.	Tube Spacing	Unit Cell Area	Matrix Area	Tube Area	Slug Area
FCal2A	6.192	5.660	8.179	28.967	16.387	2.476	12.16
FCal2C	6.180	5.680	8.179	28.967	16.298	2.330	12.16
FCal3A	7.010	6.515	9.000	35.074	18.406	2.629	13.90
FCal3C	7.010	6.515	9.000	35.074	18.406	2.629	13.90

TABLE XVI: Unit cell quantities for the hadronic forward calorimeter modules. Lengths are in mm and areas are in mm^2. Calculation of the slug area is described further on.

$0.5T^2\sin(60^\circ)$. From this, one must remove the inner volume of the electrode tubes $0.5\pi r_i^2$. This leaves the total available area (volume/unit length) available to the matrix material. For the tubes and slugs we can calculate the area. Whatever space is left over is assumed to be filled with liquid argon. The unit cell information is given in Table XVI.

The volume fractions of each of the materials is dependent on the slug and tube properties and can thus be different for two different modules of the same design, particularly in the case of FCal2 for which tubes for the two modules were from separate orders, and the slugs for the two modules were from different manufacturers. Prototype and initial production slugs were produced by Mi-Tech Metals. However, problems with slug quality led to a vendor change partway through construction. Slugs produced by the new vendor (Kulite), while within specifications, had a slightly smaller average cross-sectional area resulting in a 5% smaller mass/unit length.

The bounds on the cross-sectional area of the tungsten slugs are described above and summarized in Table XV. When slugs were received from the manufacturer, a variety of tests and measurements were performed. The triangle size d was determined, the masses and lengths were measured, and the density was checked. Compliance with the cross-sectional envelope was tested using go and no-go gauges, so no direct measurements of the cross-sectional area are available. However, this information can be obtained indirectly from measurements of the slug mass/unit length, assuming the density to be well known. Initial shipments of FCal3 slugs were oversized (average triangle size 9.01 mm). It was decided that these slugs could be used provided the remainder of the slugs were made slightly undersize the two samples were mixed uniformly. For FCal2, problems with initial shipments lead to a vendor change partway through the production, so properties of the slugs from both sources are described below. The quantity relevant to the discussion here is the mass per unit length, from which we can calculate a cross-sectional area. This information is summarized in Table XVII. The measured values for the mass/unit length fall in the range defined by the values in Table XV.

To account for the different thermal contractions of the copper and tungsten, each row of slugs is laid with a gap of 2-4 mm (warm). This gap is reduced when the module is cold. In calculating the volume fractions for the slugs we also apply a scale factor to account for the fact that the slugs in some cases will have rounded edges. Overall we apply an estimated scale factor of 0.99 for the slug volume.

For the FCal3 modules, the mixture was 31.7% oversize slugs with 68.3% undersized slugs for an effective area / unit cell of (0.317*14.53)+(0.683*13.61) = 13.90 mm^2. The volume fractions for the FCal3 are then given by:

- Tubes 2.63 / 18.41 = 0.143
- Slugs 0.99 * 13.90 / 18.41 = 0.748
- LAr 1.000-0.143-0.748 = 0.109

For the FCal2 modules, the mixtures of slugs from the two vendors are not precisely known. However, this change took place near the end of the stacking of the first module (FCal2C). This module is therefore dominantly composed of slugs from the original vendor (Mi-Tech

Module	$(M/\ell)_{meas}$	Area
FCal2 (Mi-Tech)	0.228	12.46
FCal2 (Kulite)	0.217	11.86
FCal3 (oversized)	0.266	14.53
FCal3 (undersized)	0.249	13.61

TABLE XVII: Measured mass/unit length (g/mm) for FCal2 and FCal3 slugs, with corresponding cross-sectional areas (mm^2), obtained assuming a slug density of 18.3 g/cm^3.

Metals) while the FCalA is dominantly made of slugs from the second vendor (Kulite). This is consistent with known mass difference between the FCal2 modules. However, since the precise fractions are not known, below we take the average result and quote half of the full range as the uncertainty (*i.e.* a value of 12.16±0.30). This is also useful since the simulation will likely use an average value in the beginning, until it is known whether we are sensitive to differences of this size, in which case the appropriate quantities can be easily recalculated from the information provided here.

FCal2A

- Tubes 2.476 / 16.387 = 0.151
- Slugs 0.99 * (12.16± 0.30) / 16.387 = 0.735±0.018
- LAr 1.000-0.151-(0.735±0.009) = 0.114± 0.018

FCal2C

- Tubes 2.33 / 16.298 = 0.143
- Slugs 0.99 * (12.16±0.30) / 16.298 = 0.739 ± 0.018
- LAr 1-0.143-(0.739±0.009) = 0.118 ± 0.018

From these quantities we can calculate the average density of the absorber matrix. These are shown in Table XVIII. Note, though, that these values are not valid in the endplate region of the detectors, which occupy the first and last 23.5 mm of depth (warm) for both

Module	Cu	WFeNi	LAr	Matrix	Matrix density
	8.96 g/cm^3	18.3 g/cm^3	1.4 g/cm^3	density	(with endplates)
FCal2A	0.151	0.735	0.114	14.95	14.31
FCal2C	0.143	0.739	0.118	14.95	14.31
FCal3A	0.143	0.748	0.109	15.11	14.45
FCal3C	0.143	0.748	0.109	15.11	14.45

TABLE XVIII: Material and matrix densities (g/cm^3) for the hadronic forward calorimeter modules. In the first three columns, the material densities are shown along with the volume fractions of those materials in the FCal matrix. The second last column shows the average matrix density. The final column shows the effective average density if the module endplates are included.

the FCal2 and FCal3. Each detector has a total depth of 445.5 mm (warm) so this represents 10.5% of the module depth. In these regions the matrix density is just that of pure copper. If the full depth of the FCal modules is to be treated in the Monte Carlo as consisting of a single material (mixture), the effective density in each case must be corrected to account for the endplates:

FCal2: 14.95 * 0.895 + 8.96 * 0.105 = 14.31 g/cm^3

FCal3: 15.11 * 0.895 + 8.96 * 0.105 = 14.45 g/cm^3

The effective density will also be slightly lower in the outermost and innermost regions of the detector, where the copper shells make up a small part of the absorber. In the simulation, the absorber matrix is modeled as a single volume. In order to have the density as accurate as possible in the bulk of the module, the lower density in these inner and outer regions was not accounted for in the effective density calculation.

The Monte Carlo requires that the material fractions be input as mass fractions. These have been calculated from the the values in Table XVIII and are summarized in Table XIX.

Module	Matrix (no endplates)			Matrix (with endplates)		
	Cu	WFeNi	LAr	Cu	WFeNi	LAr
FCal2A	0.091	0.899	0.011	0.150	0.840	0.010
FCal2C	0.086	0.903	0.011	0.145	0.844	0.010
FCal3	0.085	0.905	0.010	0.144	0.846	0.009

TABLE XIX: Material mass fractions for the hadronic forward calorimeter modules, for both the case in which the endplates treated as a separate (copper) volume, and for the case in which they are included as part of the (composite) matrix material. These values are calculated from the quantities in Table XVIII. For the endplates the density of 8.893 g/cm^3 (Copper 1100) is assumed.

C. Matrix Density from Module Masses

The effective density of the absorber matrix has been calculated separately from the module masses. The numbers obtained are 14.33 g/cm^3 for the FCal2 and 14.45 g/cm^3 for the FCal3, in good agreement with the numbers obtained above. The FCal2 and FCal3 effective matrix densities are considered to be consistent within their uncertainties and a density of 14.39 g/cm^3 was chosen for the ATLAS FCal GEANT4 simulation. The corresponding material mass fractions for the material making up the matrix are:

- Copper Tubes: 0.15
- WFeNi (Slug mixture): 0.84
- Liquid Argon: 0.01

Note that calculations using the unit cell properties and the measured module masses are not completely independent. A unit cell calculation done prior to the calculation based on the module masses yielded values for FCal2 and FCal3 of 14.46 g/cm^3 and 14.59g/cm^3 respectively. However, these did not account for the slug gap or other effects that will affect the slug volume, such as rounded edges etc. The choice of the (reasonable) scale factor of 0.99 for the slug volume was in part motivated by the desire to reconcile the two calculations. The sensitivity to this scale factor is an indication of the uncertainty on the unit-cell calculation. One should also note that the module densities obtained from the

masses were calculated using the cold dimensions, while warm dimensions were used for the unit-cell calculation.

D. Size of the active Liquid Argon Gap

Information on the average electrode dimensions relevant to the size of the active liquid argon gap in the six FCal modules is summarized in Tables 1 and 2 of reference [20]. The size of the gap depends upon the inner diameter of the electrode tubes and the outer diameter of the anode rods. Additionally, a small fraction of the volume of this gap is occupied by the PEEK fiber that positions the rod and ensures that it is electrically isolated from the tube. This fraction is about 1.2% for the FCal1 and 1.5-2.0% for the hadronic modules.

As was the case with the tungsten slugs, developments during the rod production lead to some differences in the size of the components delivered, in particular for the FCal3, for which it was necessary to find a second supplier. Each supplier produced rods in batches, and the properties varied slightly from batch to batch. For the FCal3 rods, about half were produced in Russia and about half were produced in China. On average, the rods from Russia were slightly undersized (5.490 mm diameter) and the rods from China were slightly oversized (5.506 mm). These rods were mixed in roughly equal proportions in the two FCal3 modules. The FCal3 electrode tubes were manufactured in a single batch with inner diameter slightly larger than nominal. Overall, the FCal3 gaps are slightly larger than nominal. For the FCal2 modules, all rods were manufactured in Russia and were slightly undersized. The tubes for the two modules were from two different orders and had slightly different inner diameters, leading to slightly different gap sizes in the two modules.

Capacitance measurements were done for each electrode in all six modules. The spread of these measurements provides a measure of the uniformity of the gap dimensions in each of the modules. These results are described in reference [21]. Though there are currently no charge collection effects applied in the FCal simulation, note that the fractional variation in the signal, resulting from variations in the electrode dimensions, is smaller than the corresponding fractional variation in the gap size [20].

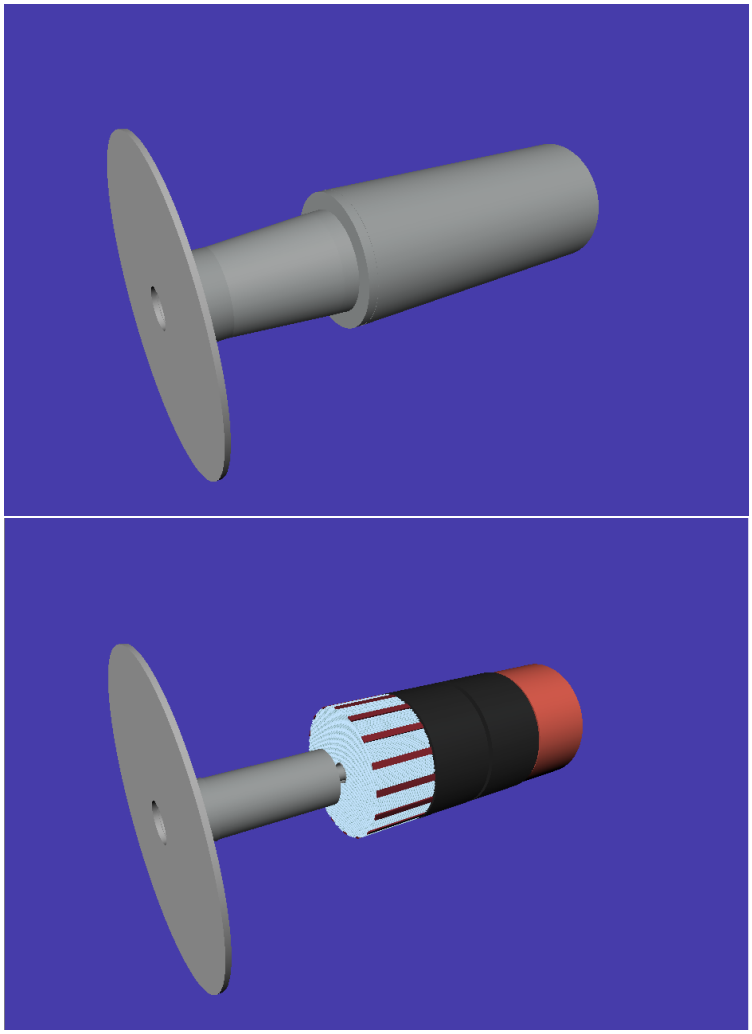

FIG. 59: Images of the FCAL in simulation. Top: This shows the FCAL cryostat and some moderator material in front of the FCAL. The large flat cylinder is moderator placed in front of the whole high-η portion of the detector. A tube of the same material slides into the FCAL "nose cone" (a cryostat element). Bottom: The FCAL is divided into an EM compartment (exploded to show LAr tubes and cable harnesses) and two hadronic compartments. Behind the hadronic compartment is an uninstrumented shielding plug of dimensions similar to an FCal modules, made of a copper alloy.

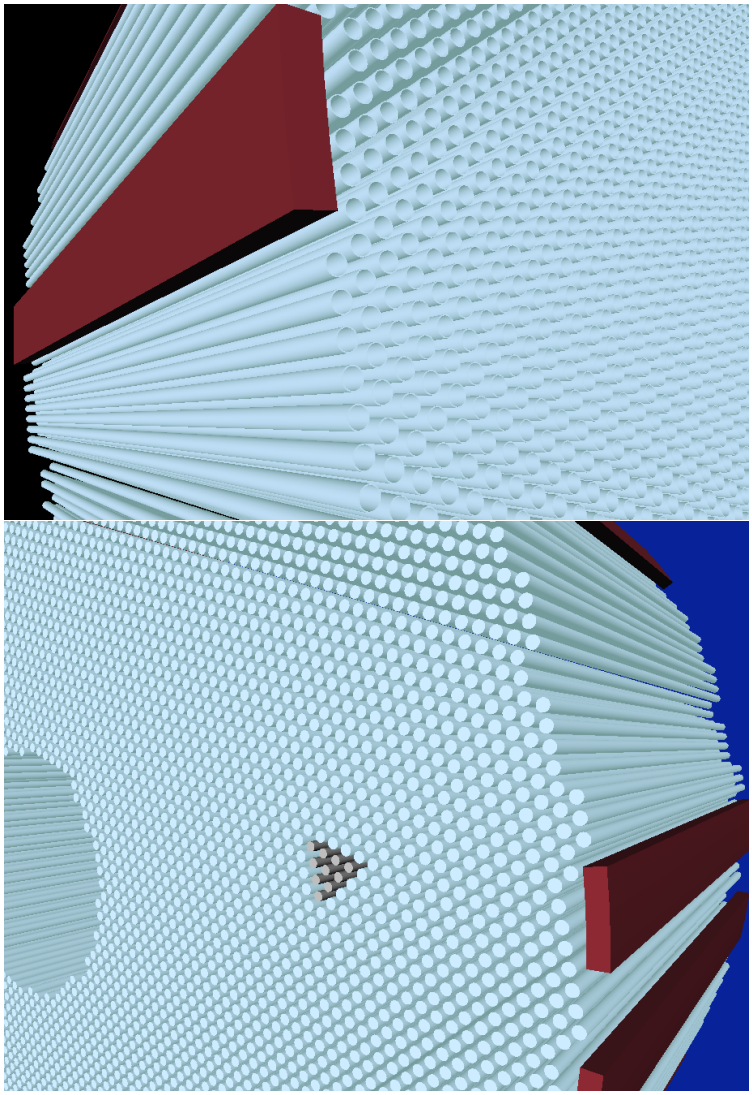

FIG. 60: The construction of liquid argon gaps within the FCAL. Top: in the EM compartment tube sections of LAr are inserted directly into the copper. Bottom: in the hadronic compartment, a solid cylinder of rod material is inserted into a slightly larger cylinder of LAr. In this diagram ten LAr tubes have been exploded to reveal the embedded rod. The brownish red structures are the cable harnesses.

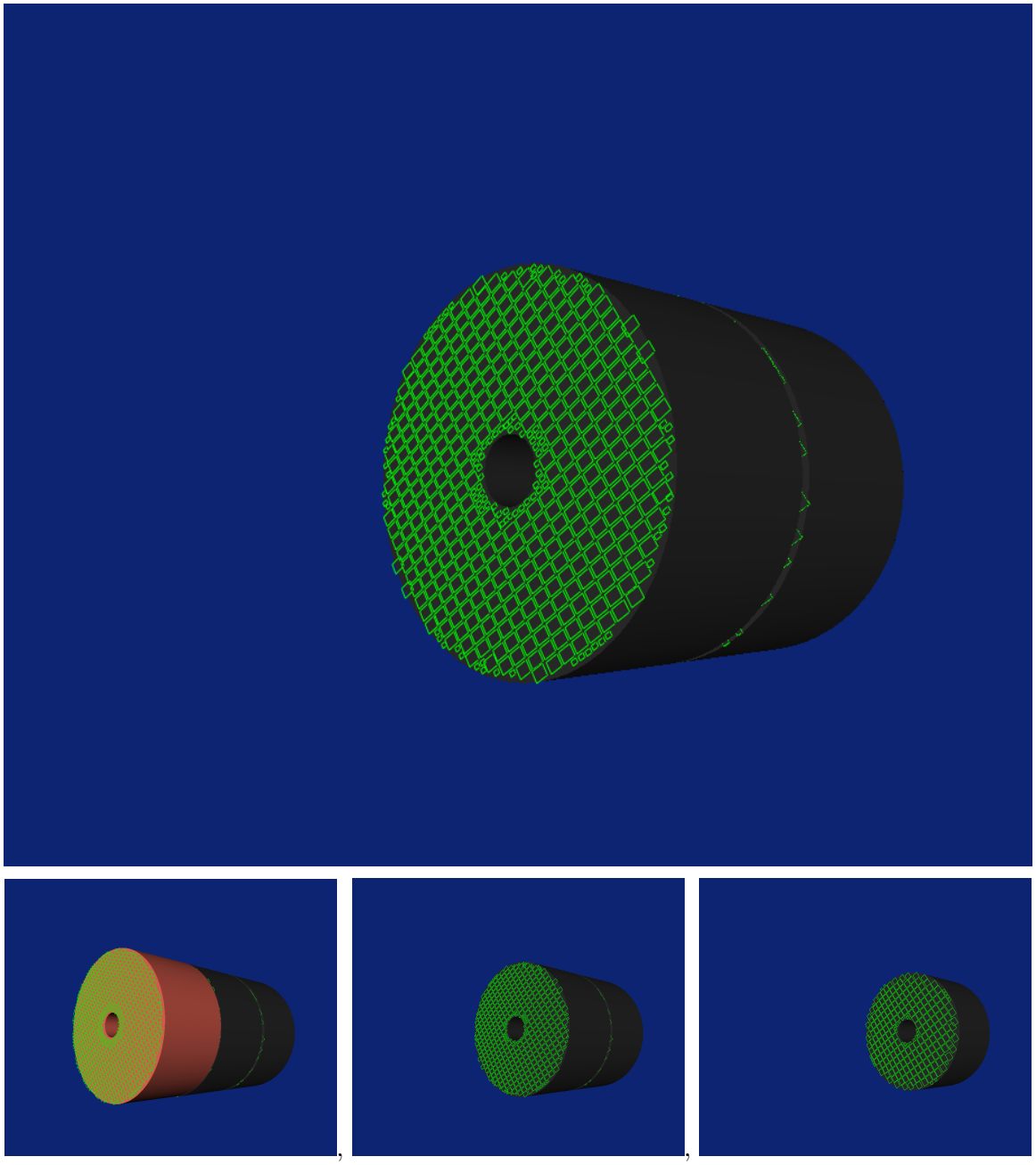

FIG. 61: Three images showing the tiling of FCAL 1, 2, and 3 (bottom) and a larger view of the tiling in FCAL 2 (top). More detailed views can be seen in Reference [20], especially Fig. 23.

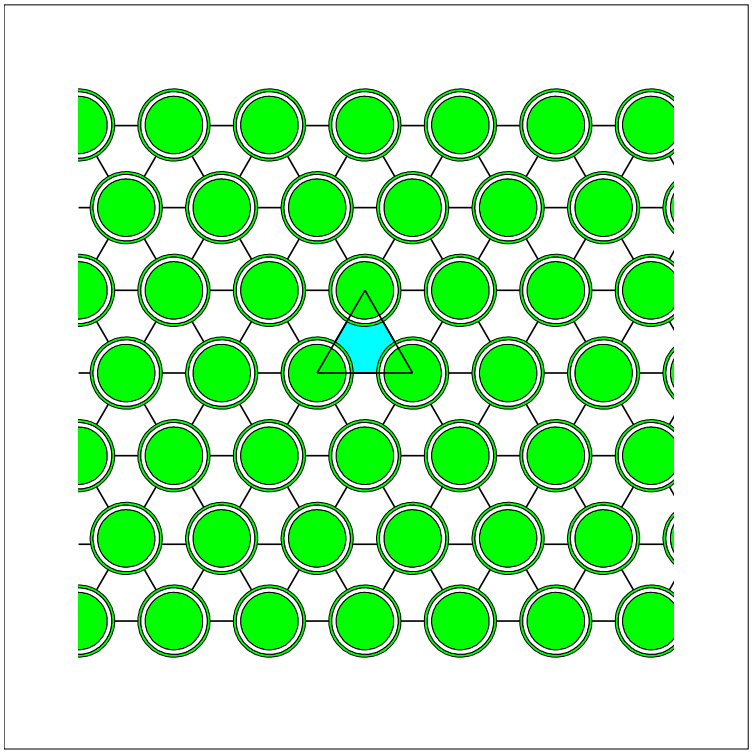

FIG. 62: Partial view of the face of an hadronic forward calorimeter module. Each module consists of a hexagonal array of tubular electrodes formed by copper tubes (shown shaded) into which rods of pure tungsten (also shaded) are inserted, with spacing and electrical isolation provided by a helically wound radiation-hard plastic fiber (PEEK). The electrode spacing corresponds to the side of an equilateral triangle that one can take as a (cross-sectional) definition of the unit cell. This triangle (see figure) and the outer radii of the three tubes define the envelope that available to the tungsten slugs (one shown shaded), which form the bulk of the absorber matrix. The envelope is shown in more detail in Fig. 63.

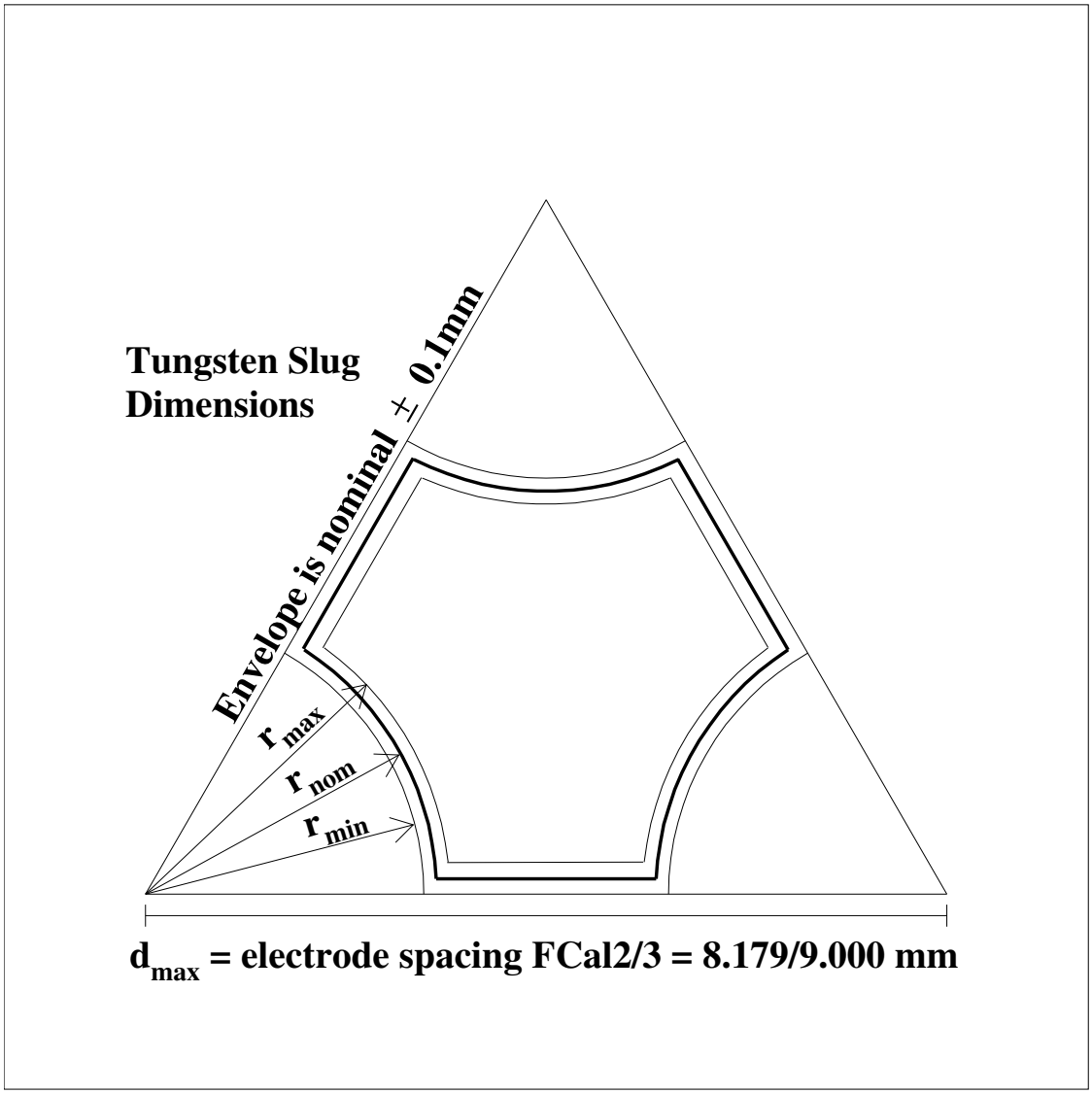

FIG. 63: Cross-sectional view of tungsten slug envelope. d_{max} represents the maximum size of the equilateral triangle containing the slug which is given by the electrode tube spacing. The nominal slug cross-section is shown as a bold line. The tolerance band is $\pm$ 0.1 mm in all lateral dimensions. The curved feature is defined in all cases as a radius from the electrode position, regardless of the triangle size of the slug.

XI. CRYOSTATS, COIL, SUPPORTS, SERVICES, AND OTHER MISCELLANEOUS MATERIALS

A. Barrel Cryostats

Here we give details about the coils and support structures, implemented as of December 2008. Details about certain approximations which have been made, and notes for future improvements are included in the sections below.

Connecting bolts In the central z part, the Al inner warm vessel of the cryostat starts at r=1150 mm and has a thickness of 10 mm. The Al inner cold vessel front wall ends at r=1385 mm with a thickness varying with η (14 to 44 mm, see Fig. 7). The inner cold vessel and the cold vessel cover are joined together at the C-side of the detector by flanges and 84 stainless steel bolts of type M16X2.0X65 LG. These have a diameter of 24 mm. Details can be found in the EDMS drawing atlabcc_0009-vAC-2. The bolts are not included in the present geometry description.

Material between the warm and cold vessel (in software) is made of Air instead of vacuum. This approximation was made as a work-around to failures in GEANT 4. In reality this volume is filled with the superinsulation. The thickness of the multiple Mylar layers in radiation lengths is small compared to the vessel wall thicknesses. There is a lot of superinsulation around the superconducting coil of the central solenoid where T. Kondo estimated the total thickness of multilayer insulation as 0.007 X_0. It is included in simulation by adjusting the Al layer thicknesses in the coil description. The superinsulation in other (less critical) places between cold and warm walls is not taken into account. For these places the air is a better approximation of reality than vacuum. However, it has no impact in practice.

Superconducting coil The superconducting coil is located between the inner warm vessel of the barrel cryostat and the inner cold vessel. The coil starts at r=1229 mm and ends at r=1275.335 mm. The coil, radiation shield, and superinsulation are modeled in the simulation by few layers of Al (12.8, 13.8 and 12 mm thick), Cu (3.05 mm) and G10 (4.7 mm). These thicknesses were tuned to total 0.671 X_0 using the coil description provided by T. Kondo in October 1997.

Superconducting coil support The coil is supported by G10 triangle supports that stretch from the coil to the cryostat walls, where they attach to 24 titanium blocks on each (positive and negative) z side. The most massive parts of the coil support - titanium blocks - are implemented in the simulation. The maximum local thickness of G10 of triangle supports is about 0.1 X_0 but their average thickness is much smaller due to elaborate cut-outs and it is small compared to the vessel's wall thickness. They lie in front of the EMEC outer wheel, between $\eta = 1.5$ and $\eta = 1.7$.

Signal and HV Feedthroughs and Cables. At each cryostat end, 32 signal feedthroughs in addition to one HV feedthrough pass from the outer warm vessel to the outer cold vessel.. The former carry approximately 120,000 signal and calibration lines, while the latter carries approximately 2,000 filtered HV lines. Though these cables are modeled within the LAr itself, they manner in which they are fed through the liquid argon (and conducted to crates on the end of the tile calorimeter) in the high-radius, high-z portion of the cryostat is not modeled. This region does not occlude any active portion of the LAr calorimeter. Since, however, they will affect the response of the tile calorimeter, these ultimately must be modeled.

Inner Detector Cables and Crates The modeling of electronics crates themselves, together with cables coming from the inner detector that occlude the EMEC, and their electronics crates, was the subject of an intensive effort that is documented in [12].

Plates and LAr Bath in the high-z high radius region Also at the high z and high radius region between the cold and warm vessels, lie additional Al plates (16 at each end, 25 mm thick). Liquid argon bath is present throughout the entire region of the cryostat bounded by the inner cold vessel and the outer cold vessel. However, in the present geometry description air still fills part of the region at the high radius, high z part of the cryostat near the feedthroughs. As with the feedthroughs, this dead material lies in front of the tile calorimeter. The plates, cables, and liquid argon occlude only a part of the tilecal extended barrel but should still require proper modeling for a correct simulation of the tilecal response.

[1] https://twiki.cern.ch/twiki/bin/view/Atlas/AthenaFramework

[2] https://twiki.cern.ch/twiki/bin/view/Atlas/LArReadoutGeometry

[3] http://atlas.web.cern.ch/Atlas/GROUPS/DATABASE/detector_description/

[4] http://geant4.web.cern.ch/geant4/

[5] http://atlas-computing.web.cern.ch/atlas-computing/
packages/simulation/geant4/G4AtlasApps/doc/index.html

[6] https://twiki.cern.ch/twiki/bin/view/Atlas/SimulationOptimization

[7] See the presentations from Ilya Tsukerman and Peter Krieger at the Milano Workshop, Agenda page http://indico.mppmu.mpg.de/indico/conferenceDisplay.py?confId=a0643

[8] A. Barriuso Poy, H. Boterenbrood, H. J. Burckhart, J. Cook, V. Filimonov, S. Franz, O. Gutzwiller, B. Hallgren, V. Khomutnikov, S. Schlenker and F. Varela, 2008 JINST 3 P05006, doi: 10.1088/1748-0221/3/05/P05006

[9] The ATLAS Computing Technical Design Report, ATLAS-TDR-017, 18 March 2005

[10] M. Leltchouk, P. Loch, G. Pospelov, W. Seligman, ATLAS note on calibration hits, in preparation.

[11] http://atlas.web.cern.ch/Atlas/GROUPS/DATABASE/detector_description/, and links therein, particularly
http://atlas.web.cern.ch/Atlas/GROUPS/DATABASE/
detector_description/RALaccess/RALaccess.htm

[12] M. Thioye, Topics in the measurement of electrons with the ATLAS detector at the LHC, Ph.D Thesis, Stony Brook University, 2008; M. Thioye, Description and Simulation of the Inactive Service Material between the Barrel/End-cap Transition Region of the ATLAS Electromagnetic Calorimeter, ATL-LARG-COM-2008-010

[13] P. Perrodo, "The ATLAS Liquid Argon Calorimetry System," CERN-OPEN-2003-019; LAPP-EXP-2002-003, also in Proceedings of the 31st International Conference on High Energy Physics (ICHEP 2002), 25 - 31 Jul 2002, Amsterdam, The Netherlands, Nucl. Phys. B, Proc. Suppl. 117 (2003)

[14] B. Aubert *et al.* "Construction, assembly and tests of the ATLAS electromagnetic barrel calorimeter", Nucl. Instrum. Methods Phys. Res., A 558 (2006) 388-418

[15] L. Martin, J.-L. Gimenez, A. Chekhtman. *"Creating IGES files of absorbers"*

(ABS.YYY.00.DRa.3).

[16] W.E. Cleland and E.G. Stern, "Signal Processing Considerations For Liquid Ionization Calorimeters in a High Rate Environment," Nucl. Inst. Meth. **A 338** (1994) 467

[17] http://atlas.web.cern.ch/Atlas/GROUPS/LIQARGSTORE/HEC/HEC_Calo/Database/Documentation/HEC_as_builtFINAL.pdf

[18] http://atlas.web.cern.ch/Atlas/GROUPS/LIQARGSTORE/HEC/HEC_Calo/General/Documents/HEC_Prod_Db_FINAL.pdf

[19] http://atlas.web.cern.ch/Atlas/GROUPS/LIQARGSTORE/HEC/HEC_Calo/General/Documents/HEC_Wheel_Db.pdf

[20] A. Artamonov et al., The ATLAS Forward Calorimeters. Submitted to JINST (2007).

[21] G. Bélanger et al., The ATLAS Liquid Argon Forward Calorimeter: Electrode Uniformity. ATLAS Note ATL-LARG-PUB-2006-001, Geneva: CERN, Sep. 2005.

[22] D. Costanzo *et al.* CERN-ATL-COM-SOFT-2004-006

[23] inner cryostat support structures passing through active calorimeter volumes, for example.

[24] This corresponds to the Atlas geometry tags ATLAS-CSC-01-00-00,ATLAS-CSC-00-00-00 for the nominal geometry, ATLAS-CSC-01-01-00, ATLAS-CSC-00-01-00 for the misaligned geometry and ATLAS-CSC-01-02-00 for the misaligned and matter distorted geometry

[25] The thicknesses are 2*0.2 mm for the steel, 1.532 mm or 1.131 mm for the lead and 2*0.139 mm or 2*0.3395 mm for the glue. The glue has the formula $C_5H_8O_4Si$, with a density of 1.69 g/cm^3 and a radiation length of 202.1 mm. The lead has density 11.35 g/cm^3 and a radiation length of 5.6118 mm; steel has a density of 7.87 g/cm^3 and a radiation length of 17.5854 mm